Probing Short-Range Structural Distortion of Stereochemically Active Lone Pairs in Extended Solid-State Materials

by

Uyen Phuong Dang

Presented to the Faculty of the Graduate School

of The University of Texas at Arlington in Partial Fulfillment

of the Requirements for the Degree of

DOCTOR OF PHILOSOPHY

Department of Chemistry & Biochemistry

THE UNIVERSITY OF TEXAS AT ARLINGTON

December 2022

Acknowledgements

This is a great opportunity for me to express my appreciation to my family, my advisor, collaborators, all lab mates, and friends who have been helping me with this study and supporting me in many different ways.

As an expression of gratitude, I would like to begin with my parents, Huan Dang and Lan Pham, parents-in-law, Tam Nguyen and Hang Le, uncle Vinh Ngo and aunt Mary Ngo, my sister Vy Dang and her husband Anh Bui, and my brother-in-law Duc Nguyen for all the unconditional support over the past few years.

I would like to express my deep gratitude to my husband, Tri Nguyen, for believing in me, supporting, encouraging me to pursue my education and career, and taking care of my precious son, Thienvan Nguyen, so many nights so that I could be able to complete my dissertation.

At the University of Texas at Arlington, I have worked with an excellent team. First and foremost, I wish to express my gratitude and appreciation to Dr. Robin Macaluso who has lighted my journey and guided me with her outstanding mentorship and support. I appreciably received her knowledge, experience, professionalism, and encouragement to achieve my educational goals. With Dr. Macaluso's continuous support, patience, and advice, I have overcome many obstacles, untangled many difficult knobs and strengthened my abilities through the years of PhD study. Additionally, I would like to thank Dr. Geneva Laurita and Dr. Sarbajit Banerjee for collaborating with my projects and providing me invaluable direction on my interest of study. I would also like to acknowledge Dr. Delphine Gout for the guidance on using the instruments to collect data for my projects.

I am very thankful to my dissertation committee members: Dr. Frederick MacDonnell, Dr. Kwangho Nam, and Dr. Rasika Dias, for the brilliant comments and suggestions on my projects.

I would like to give my warmest thanks to my research team – Melissa Orr, Hoa Nguyen, Katheryn Cruz, and Jason Lively for assisting me during my projects and a cherished time spent together in the lab.

Furthermore, this would not have been possible without the help of the UT Arlington's staffs in the Chemistry and Biochemistry department. I would like to thank Mrs. Debbie Cooke and the graduate program coordinator Stephanie Henry for all help, support, and reminders that I was able to keep up with deadlines. I also very appreciate the help from Dr. Brian Edwards and Dr. Roy McDougal on training and support with research instrumentations. I am very thankful to Dr. William Cleaver and Dr. Cynthia Griffith for their guidance on teaching duties. Thank you to Mrs. Beth Klimek for assisting me with getting supplies for my research.

I am deeply thankful to all my friends, especially Phuong Tran, Vy Nguyen, Tam Tran, and Tommy Nguyen who were always there for me whenever I needed help. Many thanks to all the people in my life who encouraged me and provided me with invaluable feedback on my education and career.

Finally, I would like to thank God for being my strength and letting me through all the difficulties. I have experience your guidance day by day and will keep on trusting you.

December 12, 2022

Abstract

PROBING SHORT-RANGE STRUCTURAL DISTORTION OF STEREOCHEMICALLY ACTIVE LONE PAIRS IN EXTENDED SOLID-STATE MATERIALS

Uyen Phuong Dang, PhD

The University of Texas at Arlington, 2022

Supervising Professor: Robin T. Macaluso

The structural and electronic effects of the lone pairs play an important role in magnetic, photocatalytic, and semiconducting behaviors of materials.[1-3] Investigating the role of stereochemically active ns^2 lone pairs derived from p-block cations in solid-state materials is important to phenomena associated with polarizable bonding, e.g., ferroelectricity. The effect of lone pairs in ferroelectric polarization has been studied on the lead metaniobate in which the covalency between Pb and O stabilizes the in-plane polarization which leads to orthorhombic symmetry.[4] $PbTiO_3$ has been widely studied for ferroelectric polarization associated with the off-centering of Ti in TiO_6 due to the characteristic $6s^2$ lone pair.[5-6] The structural distortion associated with lone pairs can be structured with long-range periodicity. However, lone-pair induced structural distortions can also be short-range in nature; investigation of these requires large X-ray and/or neutron fluxes available at synchrotron and neutron sources. The general theme of this dissertation focuses on structural characterization of Pb^{2+} containing solid-state materials using total elastic scattering where both Bragg and diffuse scattering of diffraction patterns are analyzed by Rietveld and pair distribution function techniques, respectively.

Chapter 1 presents the two chemical models that explain lone pairs of electrons, their interactions, and their influence on structural distortions. In the classical model, lone pair distortion

is explained by the hybridization of s and p atomic nonbonding. The revised lone pair model, on the other hand, state that lone pair is formed from the interaction of the cation s and p atomic orbitals with the oxide anion p orbital.

Chapter 2 presents the fundamentals of structural characterization of materials including powder X-ray diffraction, Rietveld refinement and atomic pair distribution function. Rietveld refinement is used to determine the crystallographic information and phase purity of our samples. Since we are interested in the effect of the lone pairs on the structure and properties of the Pb^{2+} containing solids, atomic pair distribution function is employed to find the local structure of the materials and ultimately characterize the lone pairs.

In **Chapter 3**, I will discuss how the Pb $6s^2$ lone pair driven structural distortions resulting in hybridization between the Pb $6s^2$ lone pair and O $2p$. This hybridization causes a change in the electronic structure of $PbVO_3Cl$ resulting in a thermochromic transition from yellow to red at 200 °C. This thermochromic phenomenon was not observed in $BaVO_3Cl$, which does not contain a stereochemically active lone pair.

Chapter 4 presents the structural, dielectric, and heat capacity behavior of the cation- and anion-deficient pyrochlore $Pb_{1.5}Nb_2O_{6.5}$ upon cooling. We find that both the vacancies and the lone pair driven distortions of the Pb cations are globally disordered in the cubic $Fd\bar{3}m$ structure, and local distortions are present at all temperatures that can be described by cristobalite-type cation ordering.

Finally, **Chapter 5** reports the Rietveld refinement results of neutron diffraction data on the cubic pyrochlore $Fd\bar{3}m$ $Pb_{1.5}Nb_2O_{6.5}$ against different models including cubic $Fd\bar{3}m$ 16d,

cubic $Fd\bar{3}m$ 96g, $F\bar{4}3m$, cristobalite $P2_12_12_1$, and cristobalite $P4_12_12$ at 100K, 200K, and 300K. The data were refined using the Rietveld methods in the GSAS-II software.

References

1. Zhang, D.; Johnsson, M.; Lidin, S.; Kremer, R. K., The New Nickel Tellurite Chloride Compound $Ni_{15}Te_{12}O_{34}Cl_{10}$ - Synthesis, Crystal Structure and Magnetic Properties. *Dalton Trans.* **2013,** *42* (5), 1394-1399.
2. Suzuki, H.; Kunioku, H.; Higashi, M.; Tomita, O.; Kato, D.; Kageyama, H.; Abe, R., Lead Bismuth Oxyhalides $PbBiO_2X$ (X = Cl, Br) as Visible-Light-Responsive Photocatalysts for Water Oxidation: Role of Lone-Pair Electrons in Valence Band Engineering. *Chem. Mater.* **2018,** *30* (17), 5862-5869.
3. Zhang, K.; Liu, C.; Huang, F.; Zheng, C.; Wang, W., Study of the Electronic Structure and Photocatalytic Activity of the BiOCl Photocatalyst. *Appl. Catal.* **2006,** *68* (3-4), 125-129.
4. Olsen, G. H.; Sørby, M. H.; Selbach, S. M.; Grande, T., Role of Lone Pair Cations in Ferroelectric Tungsten Bronzes. *Chem. Mater.* **2017,** *29*, 6414-6424.
5. Waghmare, U. V.; Spaldin, N. A.; Kandpal, H. C.; Seshadri, R., First-Principles Indicators of Metallicity and Cation off-Centricity in the IV-VI Rocksalt Chalcogenides of Divalent Ge, Sn, and Pb. *Phys. Rev.* **2003,** *67*, 125111.
6. Payne, D. J.; Egdell, R. G.; Walsh, A.; Watson, G. W.; Guo, J.; Glans, P.-A.; Learmonth, T.; Smith, K. E., Electronic Origins of Structural Distortions in Post-Transition Metal Oxides: Experimental and Theoretical Evidence for a Revision of the Lone Pair Model. *Phys. Rev. Lett.* **2006,** *96*, 157403.

Table of Contents

List of abbreviations

Å: Angstrom

ADP: atomic displacement parameter

APS: Advanced Photon Source

ANL: Argonne National Laboratory

Calc: calculated

C: Celsius

CHESS: Cornell High Energy Synchrotron Source

DFT: density functional theory

DRS: diffuse reflectance spectroscopy

DSC: differential scanning calorimetry

E_{BG}: energy band gap

EDS: energy-dispersive X-ray spectroscopy

ELF: electron localization function

F_{hkl}: structure factor

$|F_{hkl}|^2$: square of the absolute value of structure factor

F(Q): reduced tructure function

$\langle f(Q)\rangle^2$: atomic form-factor

FWHM: peak full-width at half-maximum

g: gram

G(r): reduced pair distribution function

GSAS-II: General Structure Analysis System II

I_{BG}: background intensity

I_{Bragg}: Bragg scattering intensity

I_{coh}: coherent scattering intensity

$I_{diffuse}$: diffuse scattering intensity

I_{inc}: incoherent scattering intensity

I_{MC}: multiple-scattering intensity

I(Q): total intensity of scattered X-ray beam

HAXPES: hard X-ray photoelectron spectroscopy

HOMO: highest occupied molecular orbital

LUMO: lowest unoccupied molecular orbital

NIST: National Institute of Standards and Technology

NOMAD: Nanoscaled-Ordered Materials Diffractometer

NPDF: neutron pair distribution function

NSLS-II: National Synchrotron Light Source II

Obs: observed

ORNL: Oak Ridge National Laboratory

PDF: pair distribution function

PDFgui: pair distribution function graphical user interface

PDOS: partial density of states

PPMS: physical properties measurement system

R_{exp}: expected residual

R_p: profile residual

R_{wp}: weighted profile residual

S(Q): total-scattering structure function

SNS: Spallation Neutron Source

TDOS: total density of states

TOF: time-of-flight

XANES: X-ray absorption near-edge structure spectroscopy

XRD: X-ray diffraction

XPDF: X-ray pair distribution function

VESTA: Visualization for Electronic and Structural Analysis

List of Illustrations

List of Tables

Chapter 1 Introduction

1.1. Definition of lone pairs

Lone pairs are associated with *p*-block cations described with ns^2np^0 valence electron configuration. Table 1-1 shows some examples of lone pair cations.

Table 1-1: Examples of cations carrying lone pair of electrons.

	1+	2+	3+
$2s^2p^0$			N
$3s^23p^0$			P
$4s^24p^0$	Ga	Ge	As
$5s^25p^0$	In	Sn	Sb
$6s^26p^0$	Tl	Pb	Bi

The existence of lone pairs affects the molecular shape and the Valence-Shell Electron-Pair Repulsion (VSEPR) model of crystal molecules which was developed by Gillespie and Nyholm in 1975.[1] Lone pairs are considered to be inactive and they distribute themselves to minimize electron repulsion. Lone pair repulsion causes ligands to be displaced to one side and away from the lone pair leading to an asymmetric coordination of the central cation. A common example found in many chemistry textbooks is NH_3 in which the lone pair contributes to a trigonal pyramidal geometry with bond angles distorted to be less than 109.5°, the ideal bond angle for a regular tetrahedron. Since VSEPR treats lone pairs as predominantly nonbonding in nature, they are considered as inert lone pairs which do not engage in orbital hybridization.

In the solid state, some lone pairs can become stereochemically active, and this activity can be used to observe and ultimately control properties. Lone pairs of electrons are stereochemically active when they hybridize with other orbitals, typically anion p orbitals. In many crystalline solids with cation-centered lone pairs such as Pb^{2+}, Sn^{2+} and Bi^{3+}, the hybridization of the lone pair with anion p orbital results in distorted cation-centered polyhedra. The lone-pair repulsions can induce oriented dipoles that trigger deviations from centrosymmetry in the crystal structure. Such structural distortions can lead to temperature-dependent phase transitions which are important for many applications such as ferroelectric, piezoelectric, non-linear optical and semiconductor materials.[2]

1.2. Descriptive models of lone pairs

Molecular shapes and the effect of lone pairs on molecular shapes have become general themes in chemistry. The lone pair of electrons can induce an off-centering of central metal to form a highly distorted polyhedron.[3] The concept of a chemically inert lone pair, not taking part in the formation of bonds but stereochemically active in solid state materials has long been associated with post-transition-metal cations with ns^2np^0 electronic configuration. Recently, the origin of lone pair formation has been focused on the interaction of the cation s and p atomic orbitals with the oxide anion p orbital rather than the hybridization of s and p orbitals on the cation.

1.2.1. The Orgel model

In 1959, the classical Orgel model relates structural asymmetry by lone pairs. Orgel explained the cationic lone pair distortion through an on-site mixing of ns^2np^0 cations nonbonding s and p orbitals.[4] He showed that the hybridization of s and p orbitals cannot take place on the cation occupying sites with inversion symmetry. Instead, such orbital hybridization may be generated in non-centrosymmetric sites. Mixing between the s and p states results in the second-

order stabilization. However, this classical model does not explain why some crystal structures favor the formation of stereochemically active lone pairs and exhibit one-sided coordination while other metal cations do not exhibit similar structures despite the same electronic configuration. The Pb^{2+} in both PbS and α-PbO has the same electronic configuration of $[Xe]4f^{14}5d^{10}6s^2$ but different local coordination environment. Figure 1-1 shows the local coordination environment of PbS which is cubic and forms a perfectly regular octahedron.[5] However, the Pb^{2+} lone pair in α-PbO, which does not possess an inversion symmetry, causes a distorted structure. The crystal structure of α-PbO can be described as a distorted CsCl structure in which both the lead and oxygen are four-coordinate rather than eight-coordinate found in CsCl.[6] More recently, the revised lone pair model has been applied to explain this deficiency.[7]

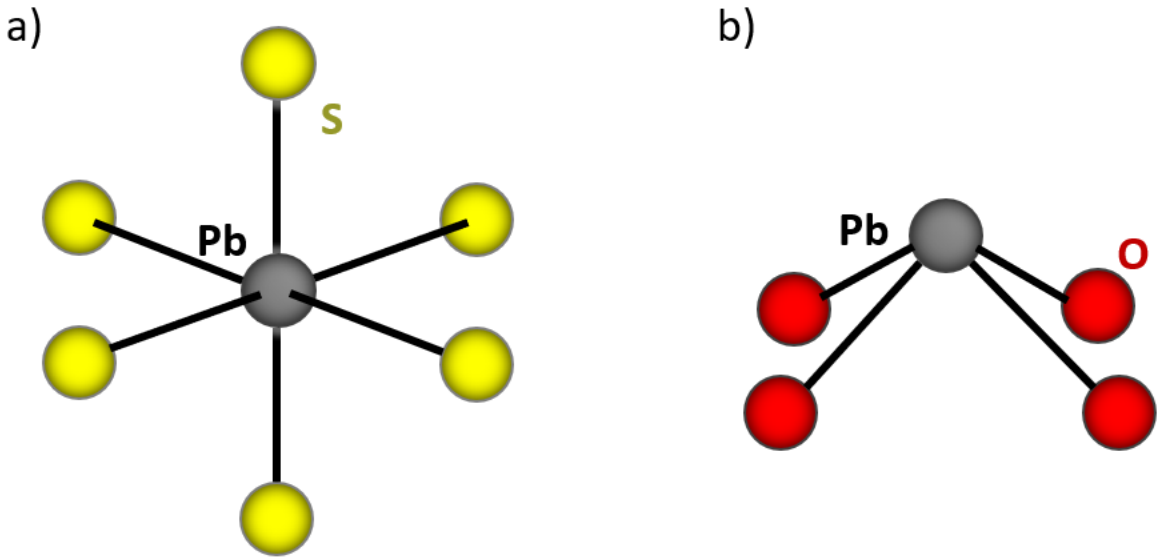

Figure 1-1: The local coordination environment of Pb^{2+}in a) PbS with a perfectly regular octahedron whereas b) the tetragonal α-PbO can be described as a distorted CsCl structure in which both lead and oxygen are four-coordinate rather than eight-coordination in a regular CsCl structure.

1.2.2. Revised lone pair model

While VSEPR assumes that lone pairs are chemically inert and the Orgel model attributes structural asymmetry to the hybridization of s and p orbitals of the central metal ion, the revised lone pair model attributes lone pair stereoactivity because of the cation sp-hybridization with p-orbitals of anions. This concept had first been proposed in the origin of the lone pair of α-PbO in 1999.[6] In 2011, lone pairs stereoactivity was described as a pseudo Jahn-Teller effect by Walsh *et al.* in a review of the stereochemistry of post-transition metal oxides.[7]

According to the revised lone pair model, the lone pair of α-PbO is considered to form from the hybridization of the 6s and 6p atomic orbitals. Density functional theory calculations indicate that the electron distribution of α-PbO is heavily distorted with the lone pair projected to one side of the Pb cation opposite from other oxygen neighbors, leading to an asymmetric metal cation coordination.

The s^2 electrons are not chemically inert, but they interact strongly with the anion p state in the valence band giving rise to filled bonding and antibonding states at bottom and top of the upper valence band, respectively, as shown in Figure 1-2. The interaction of the filled antibonding states with unoccupied cation p states eventually results in a stabilization of the occupied electronic states that induces the stereochemical activity.[7]

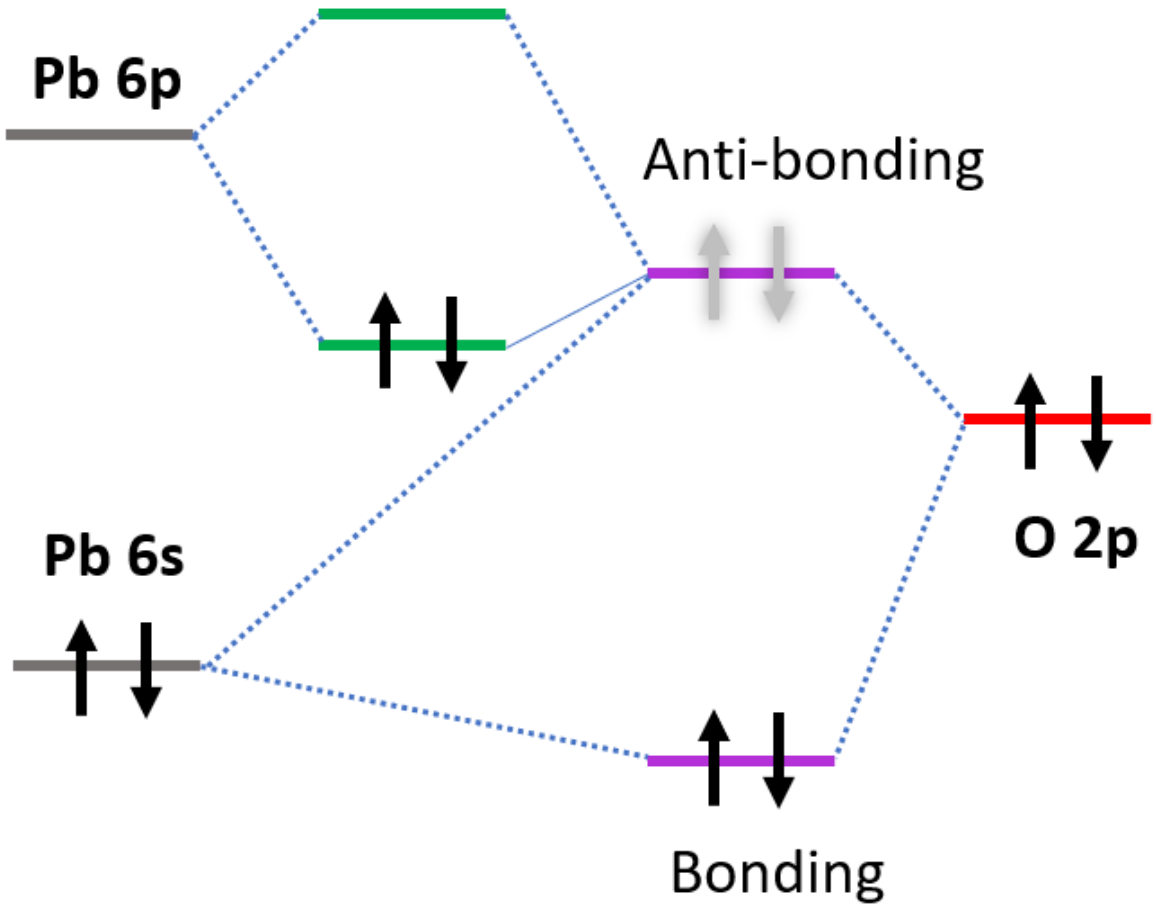

Figure 1-2: Scheme showing the revised lone pair model

Walsh *et al.* also added that the contribution of the cation s state to the antibonding state in creating interaction with the cation p state is critical to the formation of a stereochemically active lone pair. The stronger the cation *s* state contribution to the antibonding state, the stronger the stabilization of the antibonding state. Hence, the antibonding levels have a strong component of the cation *s* states. The formation of stereochemically active lone pairs also depends on the relative energy of the cation *s* and anion *p* states. The closer the cation s and anion p states are in energy, the stronger the interaction between them and the more cation states present in the upper valence band. This leads to an active lone pair effect.

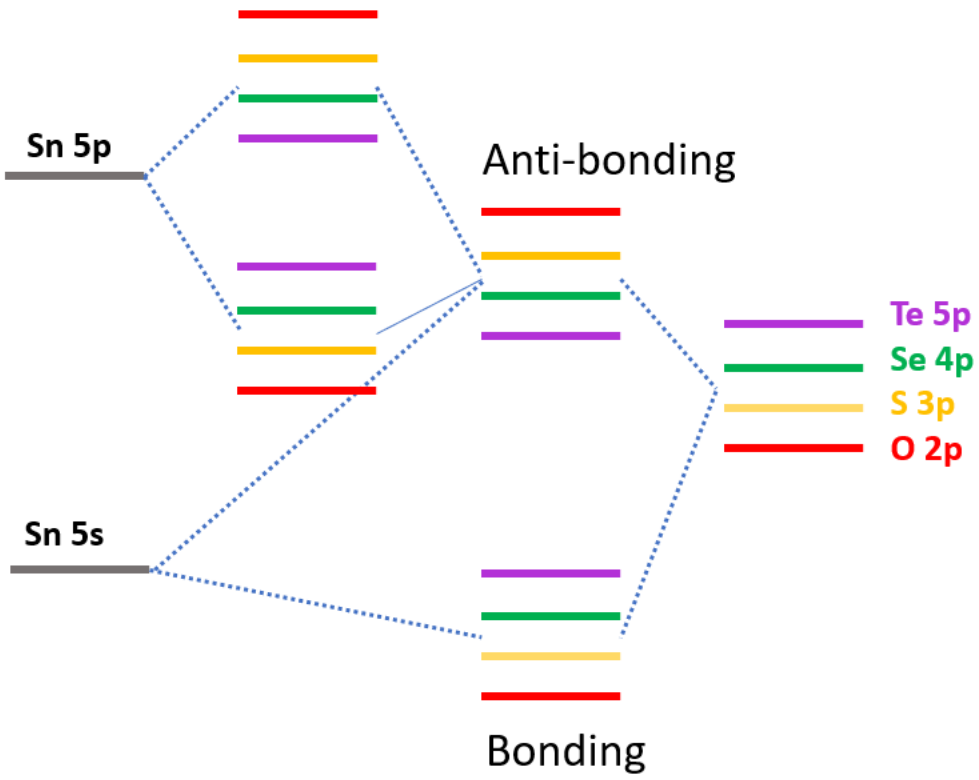

Figure 1-3: Scheme showing the interaction of Sn 5s with the anion p states.

Density functional theory calculations on SnO, SnS, SnSe, and SnTe in the rocksalt, litharge, and herzenbergite structures, respectively, show a strong interaction between Sn 5s and O 2p and gradually weaker interactions of Sn with S, Se, and Te, respectively.[8] This interaction is illustrated in Figure 1-3. Due to the progressively increasing of the energy of the anion p orbitals from O to Te, the separation of Sn 5s and the anion p states is increased. This separation reduces the interaction between them and results in less contribution of the anion p state in the bonding state and less contribution of Sn 5s in the antibonding state. The antibonding Sn 5s – O 2p states is stabilized by the strong interaction between them resulting in more active lone pair. In addition, the electron distribution around the Sn^{2+} is found to be highly asymmetric in the litharge structure type SnO and almost symmetric in the SnTe structure. This trend agrees with the increase of the energy of anion p states as the atomic number in chalcogenides increases.

1.3. Pyrochlore structure

Metal oxides such as perovskite and foordite are well-known compounds in the last decade due to their distinctive optical, electronic, and photocatalytic properties while very few pyrochlore compounds are explored to learn.[9-10] In this body of work, one of our projects involved the electron lone pairs and pyrochlore structures which have attracted considerable attention for dielectric properties.

The general formula of oxide pyrochlores is $A_2B_2O_7$ (often written as $A_2B_2O_6O'$) where A cations are typically a +2 or +3 cations and B cations are typically a +5 or +4 cations, respectively. An ideal pyrochlore structure has a cubic structure and crystallizes in ($Fd\bar{3}m$) space group with two unique cation sites. The A cation sites are eight-coordinated, and the B cation sites are six-coordinated forming two interpenetrating sublattices of corner-shared BO_6 octahedra and A_2O' chains as shown in Figure 1-4.[11-12]

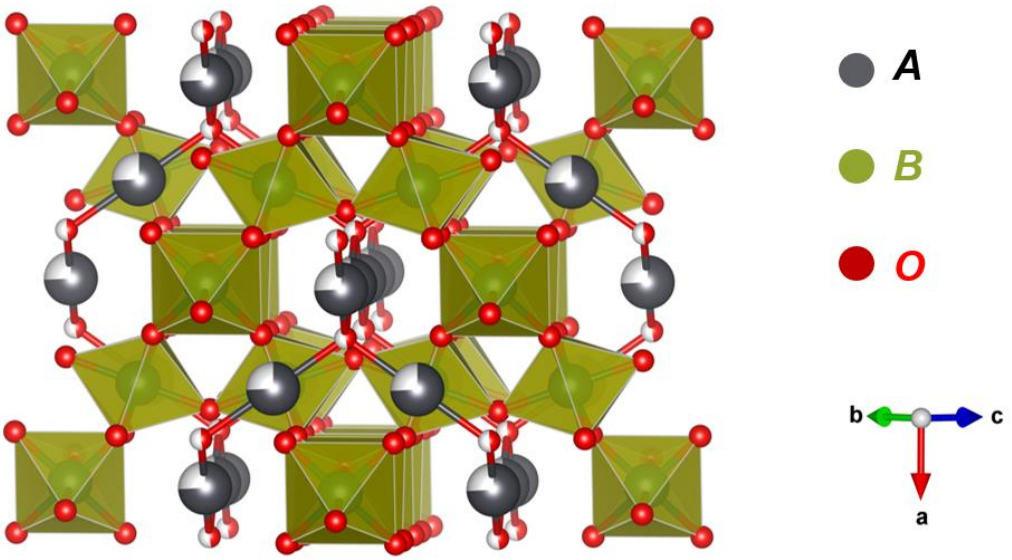

Figure 1-4: Illustration of the ideal cubic $Fd\bar{3}m$ pyrochlore showing BO_6 octahedra and the A-cation channels

Lead-containing solid-state materials with pyrochlore structures, $A_2B_2O_7$ or $A_2B_2O_6O'$ (A = Pb; B = Ns, Nb, Sb), are interesting because of their attracting applications to be pigments,[13] dielectric,[14] magnetic,[15] and relaxor ferroelectric materials.[16] The pyrochlore structure tolerates a wide range of substitutions at all three sites leading to a large diversity of electrical properties.[17]

Bismuth titanate $Bi_2Ti_2O_6O'$ is of particular stoichiometric pyrochlore containing lone pair-driven distortions published by Ram Seshadri and coworkers.[18] In this material, the Bi^{3+} on the A site displays an incoherent off-centering with their coordination polyhedra, and that is revealed by the heat capacity measurement. The previous study also showed that the presence of disordered displacements of Bi^{3+} cations with a lone pair from the Wyckoff position 16*d* of the idealized cubic pyrochlore to the 96*h* positions. [19] From the pair distribution function data, Ram Seshadri and coworkers suggest that lone-pair-active Bi displacements correlates with their nearest neighbors leading to zigzag distortions of the $O'Bi_4$ tetrahedra in the supercell.

Stereochemistry of lone pairs in extended solids has been studied using density functional calculations in conjunction with the electron localization function.[20-21] Pb^{2+} lone pairs in the cubic defect pyrochlore $Pb_2Sn_2O_6$ is also studied for the effect of lone pairs distortions on physical behavior.[22] From the electron localization function data, the O' atoms are complete absence in the crystal structure and is replaced by a vacancy resulting in topological frustration of the lone pair. Due to this symmetry of the crystal structure, the lone pair cannot localize into a single lobe of electron density, and instead splits into two lobes. These lone pair distortions remain frustrated preventing coherent long-range ordering.

1.4. References

1. Gillespie, R. J.; Nyholm, R. S., Inorganic Stereochemistry. *Q. Rev. Chem. Soc* **1957,** *11*, 339-380.
2. Liang, F.; Kang, L.; Lin, Z.; Wu, Y., Mid-Infrared Nonlinear Optical Materials Based on Metal Chalcogenides: Structure–Property Relationship. *Cryst. Growth Des.* **2017,** *17* (4), 2254-2289.
3. Stoltzfus, M. W.; Woodward, P. M.; Seshadri, R.; Klepeis, J.-H.; Bursten, B., Structure and Bonding in $SnWO_4$, $PbWO_4$, and $BiVO_4$: Lone Pairs vs Inert Pairs. *Inorg. Chem.* **2007,** *46* (10), 3839-3850.
4. Orgel, L. E., The Stereochemistry of B Subgroup Metals. Part 11. The Inert Pair. *J. Chem. Soc.* **1959**, 3815-3819.
5. Ettema, A. R. H. F.; Haas, C.; Moriarty, P.; Hughes, G., Wave Function Imaging of the PbS(001) Surface with Scanning Tunneling Microscopy. *Surf. Sci.* **1993,** *287*, 1106.
6. Watson, G. W.; Parker, S. C., Origin of the Lone Pair of α-PbO from Density Functional Theory Calculations. *J. Phys. Chem. B* **1999,** (103), 1258-1262.
7. Walsh, A.; Payne, D. J.; Egdell, R. G.; Watson, G. W., Stereochemistry of Post-Transition Metal Oxides: Revision of the Classical Lone Pair Model. *Chem. Soc. Rev.* **2011,** *40* (9), 4455-4463.
8. Walsh, A.; Watson, G. W., Influence of the Anion on Lone Pair Formation in Sn(II) Monochalcogenides. *J. Phys. Chem. B* **2005,** *109*, 18868-18875.
9. Abirami, R.; Senthil, T. S.; Kalaiselvi, C. R., Preparation of Pure $PbTiO_3$ and (Ag-Fe) Codoped $PbTiO_3$ Perovskite Nanoparticles and their Enhanced Photocatalytic Activity. *Solid State Commun.* **2021,** *327*, 114232.
10. Zhou, C.; Wang, T.; Li, D. Z.; Wang, J.; Shi, R.; Zhang, T., Flux-Assisted Low Temperature Synthesis of Nanoplates with Enhanced Visible Light Driven Photocatalytic H_2-Production. *J. Phys. Chem. C* **2021,** *125*, 23219-23225.
11. Sleight, A. W., New Ternary Oxides of Mercury with the Pyrochlore Structure. *Inorg. Chem.* **1968,** *7*, 1704-1708.
12. Subramanian, M. A.; Aravamudan, G.; Subba Rao, G. V., Oxide Pyrochlores - A Review. *Prog. Solid State Chem.* **1983,** *15* (2), 55-143.
13. Andrea, M.; Saniz, R.; Krishnan, D.; Rabbachin, L.; Nuyts, G.; De Mayer, S.; Verbeeck, J.; Janssens, K.; Pelosi, C.; Lamoen, D.; Partoens, B.; De Wael, K., Unraveling the Role of Lattice Substitutions on the Stabilization of the Intrinsically Unstable $Pb_2Sb_2O_7$ Pyrochlore: Explaining the Lightfastness of Lead Pyroantimonate Artists' Pigments. *Chem. Mater.* **2020,** *32*, 2863-2873.
14. Ubic, R.; Reaney, I. M., Structure and Dielectric Properties of Lead Pyrochlores. *J. Am. Ceram. Soc.* **2002,** *85* (10), 2472-2478.
15. Hallas, A. M.; Arevalo-Lopez, A. M.; Sharma, A. Z.; Munsie, T.; Attfield, J. P.; Wiebe, C. R.; Luke, G. M., Magnetic Frustration in Lead Pyrochlores. *Phys. Rev. B* **2015,** *91*, 104417.

16. Smith, R. M.; Gardner, J.; Morrison, F. D.; Rowley, S. E.; Ferraz, C.; Carpenter, M. A.; Chen, J. S.; Hodkinson, J.; Dutton, S. E.; Scott, J. F., Quantum Critical Points in Ferroelectric Relaxors: Stuffed Tungsten Bronze $K_3Li_2Ta_5O_{15}$ and Lead Pyrochlore ($Pb_2Nb_2O_7$). *Phys. Rev. Mater.* **2018,** *2* (8), 084409.
17. Anaf, W.; Schalm, O.; Janssens, K.; De Wael, K., Understanding the (in)Stability of Semiconductor Pigments by a Thermodynamic Approach. *Dyes. Pigm.* **2015,** *113*, 409-415.
18. Shoemaker, D. P.; Seshadri, R.; Tachibana, M.; Hector, A. L., Incoherent Bi Off-centering in $Bi_2Ti_2O_6O'$ and $Bi_2Ru_2O_6O'$: Insulator versus Metal. *Phys. Rev.* **2011,** *84*, 064117.
19. Shoemaker, D. P.; Seshadri, R.; Hector, A. L.; Llobet, A.; Proffen, T.; Fennie, C. J., Atomic Displacements in the Charge Ice Pyrochlore $Bi_2Ti_2O_6O'$ Studied by Neutron Total Scattering. *Phys. Rev.* **2010,** *81*, 144113.
20. Seshadri, R.; Baldinozzi, G.; Felser, C.; Tremel, W., Visualizing Electronic Structure Changes across an Antiferroelectric Phase Transition: Pb_2MgWO_6. *Mater. Chem.* **1999,** *9*, 2463.
21. Seshadri, R., Visualizing Lone Pairs in Compound Containing Heavier Congeners of the Carbon and Nitrogen Group Elements. *Chem. Sci.* **2001,** *113*, 487.
22. Seshadri, R., Lone Pairs in Insulating Pyrochlores: Ice Rules and High-*k* Behavior. *Solid State Sci.* **2006,** *8*, 259-266.

Chapter 2 Methods

2.1. Diffraction in general

X-ray diffraction (XRD) is a powerful technique for characterizing crystalline materials. X-rays are produced by high-speed electrons accelerated through a high voltage which allows to strike a metal target. This process leads to monochromatic x-rays which in turns strikes a finely powdered sample that contains a large number of tiny crystals in a perfectly random orientation. The incident beam strikes various lattice planes in every possible orientation generating diffracted beam which is detected by a movable detector. The relationship between the wavelength of the incident X-rays, λ, the angle of incidence, or Bragg angle, θ, and the distance between pairs of adjacent planes, the *d-spacing*, *d*, is known as Bragg's law.[1] The derivation of Bragg's law[1] is illustrated in Figure 2-1. A set of parallel and equidistant planes of crystal, 11' and 22', is represented with the inter-planar distance between pairs of adjacent planes which is called *d-spacing*, *d*. A beam of monochromatic X-rays $\overline{AB}$ is incident on plane 11' with angle θ and reflected along $\overline{BC}$. Similarly, a second beam $\overline{DY}$ is incident on the adjacent plane 22' with angle θ, scatted by atom Y, and reflected along $\overline{YE}$. The beam 22' must travel the extra distant $\overline{XY}$ + $\overline{YZ}$ as compared to beam 11' if the two beams are to continue traveling in phase and parallel. The $\overline{XY}$ + $\overline{YZ}$ distance must equal the integral multiple of the wavelength, $n\lambda$, where *n* are the integers. Considering the perpendicular distance between planes 11' and 22', *d*, as the hypotenuse of the triangle Δ XYB and $\overline{XY}$ as the opposite, one can use trigonometry to relate the angle of incidence, θ, to the distance $\overline{XY}$ by

$$\overline{XY} = d\sin\theta \qquad \text{Equation 2-1}$$

Because $\overline{XY} = \overline{YZ}$,

$$XYZ = \overline{XY} + \overline{YZ} = 2XY = 2\,d\sin\theta \qquad \text{Equation 2-2}$$

Therefore,

$$n\lambda = 2\,d\sin\theta \qquad \text{Bragg's Law} \qquad \text{Equation 2-3}$$

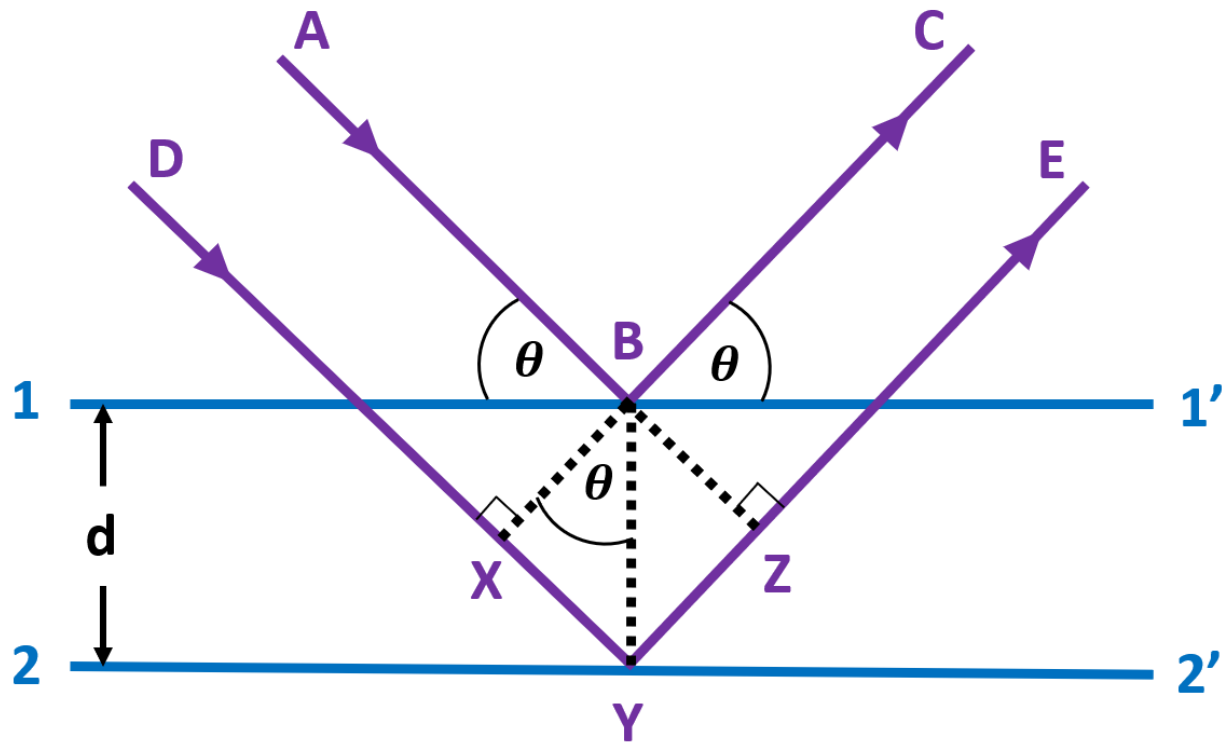

Figure 2-1: Derivation of Bragg's law

Diffraction occurs only when constructive interference from interplanar spacing satisfies Bragg's law, $2d\sin\theta = n\lambda$ where n is integer. Diffraction methods can identify chemical information such as phase identification, phase purity and crystallographic information based on Bragg's law.[2]

2.2. Rietveld refinement method

Powder diffraction data can be analyzed using different techniques such as Rietveld, Pawley, and Le Bail methods.[3-5] What distinct Rietveld method from other structural refinement methods is that it allows to analyze the whole diffraction pattern or the full profile refinement. Without Rietveld refinement method, one would not be able to analyze peak by peak from a diffraction pattern. Rietveld refinement is a method of refining crystal structure from x-ray or neutron powder diffraction data where the least-squares refinements are carried out until the best fit between the observed powder diffraction pattern and the calculated pattern is obtained.[3, 6] The structure of a typical powder diffraction pattern is described by 2θ positions, intensities, and shapes of multiple Bragg reflections.[7] Each of the three components contains information about the crystal structure of the material, the properties of the sample and the instrument parameters.

Positions of Bragg peaks contain information about the unit cell symmetry and parameters as they are established from the Bragg's law as a function of the wavelength and the interplanar distances, *d*-spacing.[7] In addition, diffraction peaks appear at specific diffraction angles of different reflections due to scattering by periodic lattices. Therefore, both unit cell dimensions and the wavelength are the two major factors that determine the position of Bragg peaks.

The intensities of Bragg peaks in any diffraction pattern have different intensities that are used to determine space group symmetry and atomic coordinate of atoms. The peak intensities can be calculated for individual Bragg peaks from the structural model and are determined by several factors including structural factors, specimen factors, and instrumental factors.[7] The structure factor, F_{hkl}, also known as the structure amplitude, describe the amplitude f_j and phase δ_j of a waves diffracted from an atom. It is defined by the scattering factors of all atoms together with the

coordinates and types of atoms in the unit cell. It is important to note that the intensity of a wave is proportional to the square of its amplitude

$$I \; \alpha \; f_j^2 \qquad \text{Equation 2-4}$$

The structure factor or structure amplitude for the *hkl* reflection is given below

$$F_{hkl} = \sum_j f_j \, exp(i\delta_j) = \sum_j f_j (\cos \delta_j + i \sin \delta_j) \qquad \text{Equation 2-5}$$

where $i = \sqrt{-1}$

In an X-ray diffraction experiment, the amplitude of light scattered by a crystal is determined by the arrangement of atoms in the diffracting planes, and the experimental intensity, $I_{(hkl)}$, is directly related to the structure through the structure amplitude, as shown in the following equation

$$I_{hk_l} \; \alpha \; |F_{hkl}|^2 = \sum_j (f_j \cos \delta_j)^2 + \sum_j (f_j \sin \delta_j)^2 \qquad \text{Equation 2-6}$$

$|F_{hkl}|^2$, is the square of the absolute value of structure amplitude.

Specimen factors depend on several sample properties including shape, size, and grain size. Instrumental factors that affect diffraction patterns include properties of radiation, type of focusing geometry, and properties of the detector.

The shape of Bragg peaks is best described by a bell-like function or the peak shape function. It is also represented by the two simplest peak shape functions which are Gaussian and Lorentzian distributions of the intensity in the Bragg peak. The Lorentzian function is sharp near its maximum with long tails on each side near its base. The Gaussian function, on the other hand,

has rounded maximum with no tails at the base. Both functions are centrosymmetric. Figure 2-2 shows the illustration of Gaussian and Lorentzian peak shape functions.

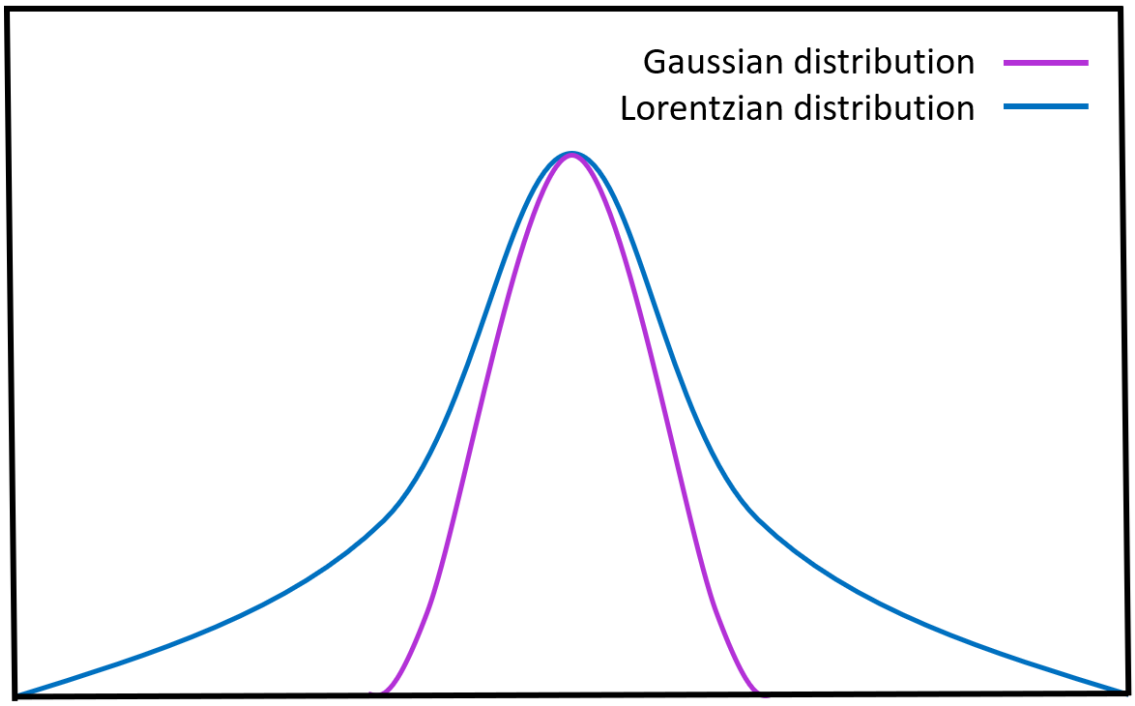

Figure 2-2: Illustration of Gaussian and Lorentzian distributions

The structural analysis was performed with the Rietveld method using the High Score Plus software that includes solving the structure and refining the model.[8] The Rietveld method requires a model of a crystal structure similar to the one being investigated. Scale factor is one of the variables in structure refinement that shows the relative height of the experimental with calculated intensities. Its correctness is critical in obtaining a good agreement between the observed and calculated intensities. In typical Rietveld refinements, the observed diffraction intensities can be modelled with the contribution of background scattering which is commonly fitted with low-order polynomial functions.[9] When a diffraction pattern contains multiple phases, the scale factor, unit cell, atomic parameters, preferred orientation, and peak profile parameters are set individually for

each phase. The atomic parameters such as atomic position, occupancy, and thermal parameters are refined for each atom in the phase. At this point, the positions of the observed and calculated peaks must match well. Then, the symmetry of the peak is fitted by refining the peak profile parameters such as the Cagliotti peak width function parameters U, V, and W, profile shape parameters, peak asymmetry profile, and anisotropic broadening function.[9] The Caglioti equation describes how peak width varies with 2θ as shown below

$$H_k = (U \tan^2\theta + V \tan\theta + W)^{1/2} \qquad \text{Equation 2-7}$$

where H_k is the Caglioti function, and U, V, and W are refinable parameters.

The difference plot provides clues to what to refine, which can be given as

$$\Delta y_i = y_i(obs) - y_i(calc) \qquad \text{Equation 2-8}$$

When the difference between the observed and calculated intensities is large, there is something affecting the peak intensity. The peak shape and position parameters are then needed to be modified to reduce the difference. These steps are repeated until a good fit of the model to the observed data is achieved based on statistics which are discussed later.

During the Rietveld refinement, the means of a non-linear least squares minimization are used to solve the following equations:

$$y_1(calc) = k\, y_1(obs) \qquad \text{Equation 2-9}$$

$$y_2(calc) = k\, y_2(obs)$$

...

$$y_n(calc) = k\, y_n(obs)$$

where $y_i(obs)$ and $y_i(calc)$ are the observed and calculated intensities of a point *i* of the powder diffraction pattern, respectively, *k* is the pattern scale factor, and *n* is the total number of the measured data points.[7]

The quality of the refinement using Rietveld method is quantified by parameters such as profile residual, R_p, weighted profile residual, R_{wp}, expected residual, R_{exp}, and goodness of fit, χ^2. Criteria of fit between the entire observed and entire calculated data is based on the minimization of those residual values. The pattern residual, R_p, and the weighted pattern residual, R_{wp} are given as

$$R_p = \frac{\sum|y_i(obs) - y_i(calc)|}{\sum y_i(obs)} \qquad \text{Equation 2-10}$$

$$R_{wp} = \left\{\frac{\sum w_i(y_i(obs) - y_i(calc))^2}{\Sigma w_i(y_i(obs))^2}\right\}^{1/2} \qquad \text{Equation 2-11}$$

where $y_i(obs)$ and $y_i(calc)$ are the observed and calculated intensities at the i^{th} step, respectively, and w_i is a suitable weight associated to $y_i(obs)$ and $y_i(calc)$ (usually $w_i = 1/y_i$) . The $y_i(calc)$ depends on structural and profile parameters including background, specimen displacement, zero-shift error, scale factors, sample transparency, atomic coordinates, occupancies, lattice parameters, peak shape, peak width, and preferred orientation.[10] The progress of a Rietveld refinement can be monitored by R_{wp} value which is mathematically the most meaningful residual because the numerator is the residual being minimized. A small value of R_{wp} indicates a successful minimization. Another numerical criterion is the "goodness of fit", χ^2, shown in the following equation

$$\chi^2 = \left[\frac{R_{wp}}{R_{exp}}\right]^2 \qquad \text{Equation 2-12}$$

During the refinement process, χ^2 usually starts out large and decreases as the model produces better agreement with data. A χ^2 of 1 is ideal for a good fit between a crystallographic model and the experimental data. In our work, acceptable χ^2 is about 1.2.

Another parameter usually refined using the Rietveld method is atomic displacement parameters (ADP) which is also known as thermal parameters. At any temperature that is higher than absolute zero, the atoms vibrating about their equilibrium lattice site. These vibrations are quantified by the Debye-Waller temperature factor given below

$$B^j = 8\pi^2(U^2)^j \qquad \text{Equation 2-13}$$

where B^j is the displacement parameter, and $(U^2)^j$ is the mean-square amplitude of the vibration of the j^{th} atom from its equilibrium position (x, y, z) in $Å^2$. In addition to the displacements caused by thermal motion, these parameters include several effects such as preferred orientation, deformation of the electron density, or porosity. Information on atomic displacement parameters would also be useful since anomalous ADP's may warrant any further characterization such as pair distribution function measurement, hard X-ray photoelectron spectroscopy measurement, and density functional theory calculation.

2.3. Atomic Pair Distribution Function

2.3.1. Why pair distribution function?

Conventional powder X-ray diffraction analysis relies on information in the Bragg peaks in the diffraction pattern which yields the average structure of materials. However, traditional crystallographic approaches to structure determination are insufficient for complex materials that contain small randomness and local deviations from perfect periodicity. These important structural features are buried in between or underneath the Bragg peaks in the form of diffuse scattering that

cannot be probed using conventional crystallographic analysis. Thus, an alternative method known as atomic pair distribution function (PDF) analysis is needed to probe the diffuse scatterings. Because we consider both Bragg intensities and diffuse scatterings, as shown in Figure 2-3, an experiment called total scattering experiment is employed to measure all the coherent scattering throughout all of the reciprocal space. From X-ray scattering experiments, one can understand not only the local structure which is the additional information that is to be gained but also the average structure.

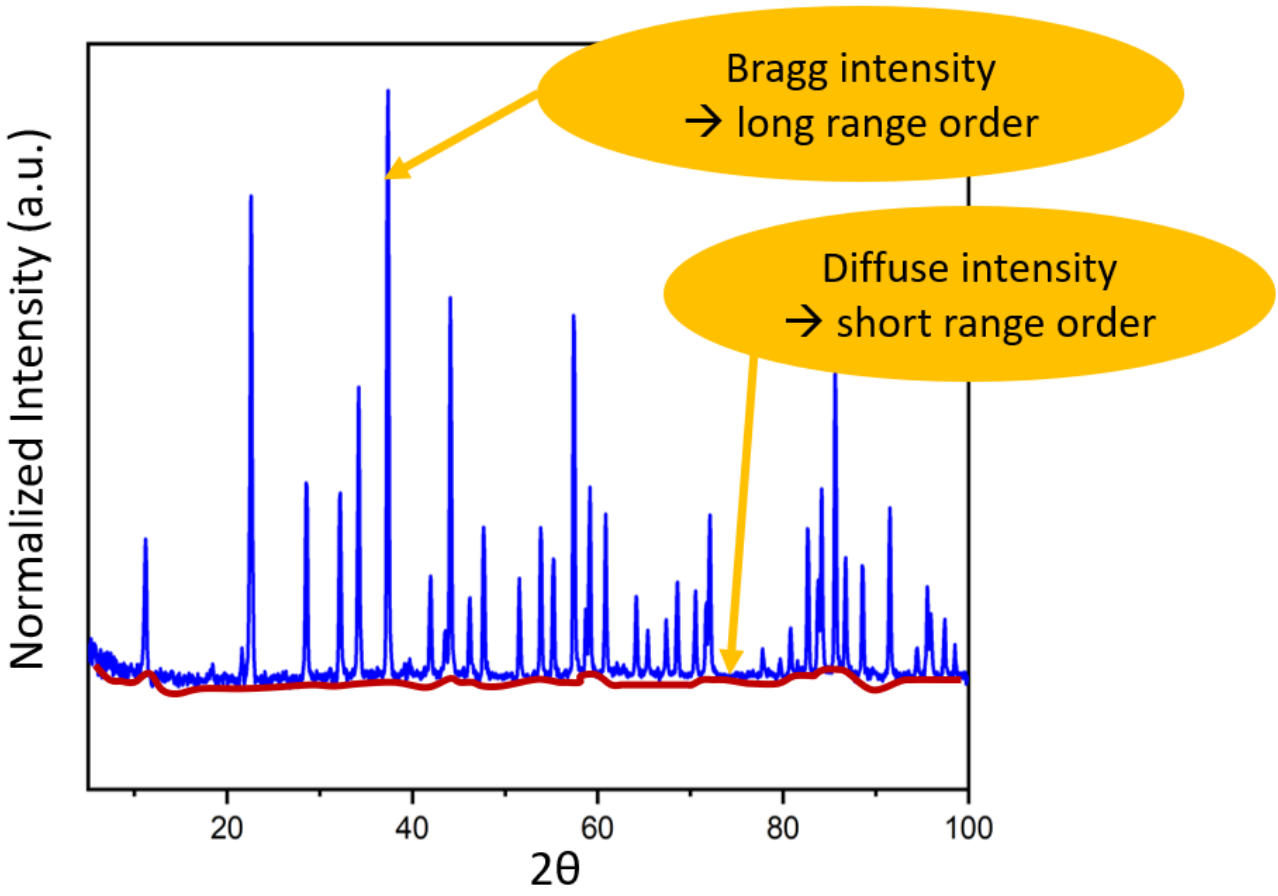

Figure 2-3: Illustration of Bragg and diffuse intensities in a powder diffraction pattern

2.3.2. What is pair distribution function?

PDF describes the probability of finding atomic pairs separated by a distance *r*. The PDF can also be understood as a bond length distribution which yields the local structure beyond the unit cell size while Bragg intensities only give average structure within a unit cell.[11] The study of PDF analysis can be performed on different length scales to obtain information about long-range ordered structure from the Bragg scattering and short-range structural correlations from the diffuse scattering intensity.[12] This method uses extremely short wavelength, that is, of higher energy such as synchrotron radiation X-rays of energy 60 keV,[13] over a wide-angular range of which they are detected resulting a wide range of reciprocal space. Powder diffraction data are usually presented as diffracted intensity as a function of the momentum transfer of scattering particles, Q, which is defined as the difference between the incoming and outgoing wavevectors, as shown in Figure 2-4. Q is the scattering vector whose magnitude is given by

$$Q = |Q| = 2k\,sin\,\theta = \frac{4\pi \sin\theta}{\lambda} = \left|k_{outgoing} - k_{incoming}\right| \quad \text{Equation 2-14}$$

where λ is the wavelength of the probe, θ is half of the angle formed between the incident and scattered directions.[14]

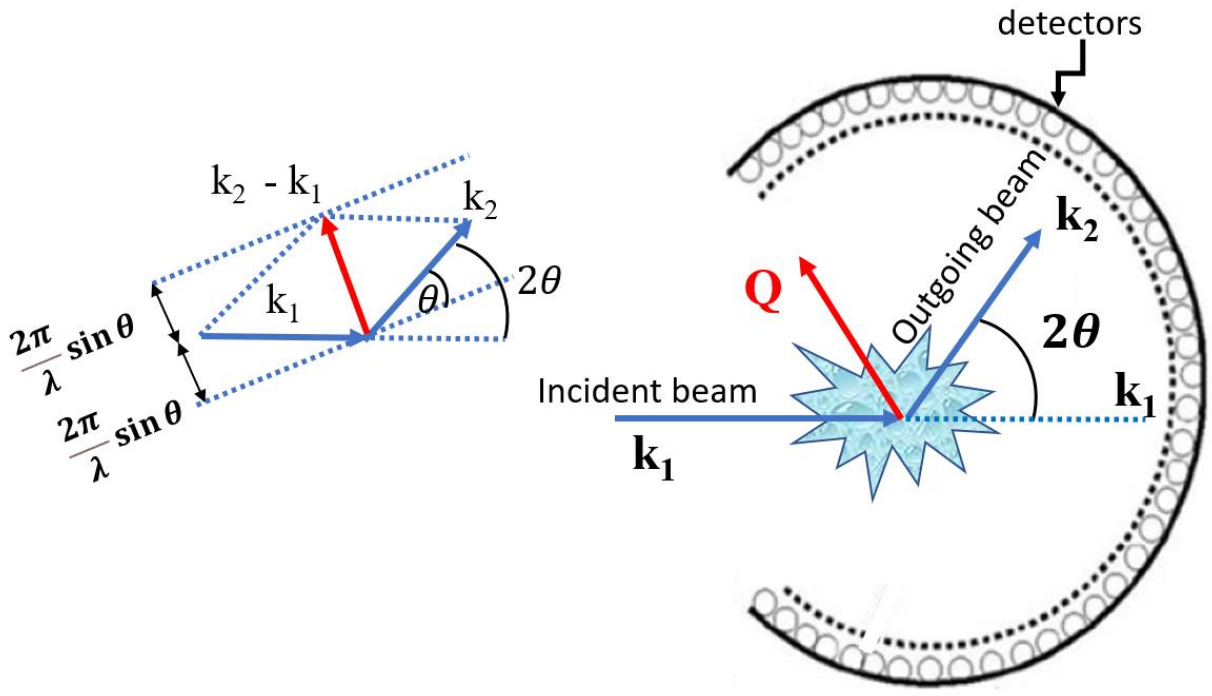

Figure 2- 4: Schematic of diffracted beam of X-rays or neutrons on powder sample, and the intensity is collected as a function of angle.

2.3.3. How does PDF work?

PDF data can be collected from angle dispersive X-ray diffraction or time-of-flight (TOF) neutron diffraction. The time-of-flight of neutrons is the time it takes for the neutron to move from the moderator to the detector. As a beam of X-rays or neutrons hits a powder sample in a PDF experiments, the intensity is collected as a function of angle resulting in a raw diffraction pattern. In the case of X-ray scattering, the distance from sample to detector is calibrated, and the data is integrated to go from 2-dimension to 1-dimension and obtain the total intensity of scattered X-ray beam, I(Q). The raw data from 1-dimension TOF neutron diffraction, on the other hand, is treated with binning and conversion of TOF to Q and I(Q). The I(Q) equation is given by

$$I(Q) = I_{Bragg} + I_{diffuse} = I_{coh} + I_{inc} + I_{MC} + I_{BG} \qquad \text{Equation 2-15}$$

where I_{Bragg} is the Bragg scattering intensity, $I_{diffuse}$ is the diffuse scattering intensity, I_{coh} is the coherent scattering intensity, I_{inc} is the incoherent scattering intensity, I_{MC} is the multiple-scattering intensity, and I_{BG} is the background intensity.

In crystallographic analysis, the background is curve-fitted and discard. The background in the PDF analysis, on the other hand, contains a wealth of information about local structure. Thus, the collected diffraction patterns are corrected for instrument and sample parameters and to obtain background. Details of data correction can be found Reference #15. The corrected intensity is then normalized with respect to the intensity of the incoming beam to obtain the total-scattering structure function, S(Q), a dimensionless quantity related to coherent scattering signal, as shown below

$$S(Q) = \frac{I(Q)}{\langle f(Q) \rangle^2} \quad \text{for X-ray scattering} \qquad \text{Equation 2-16}$$

$$S(Q) = \frac{I(Q)}{\langle b \rangle^2} \quad \text{for neutron scattering} \qquad \text{Equation 2-17}$$

where $\langle f(Q) \rangle^2$ is the atomic form-factor, and b is the scattering length or neutron scattering cross section. This approach results in a reduced structures function,[14]

$$F(Q) = Q(S(Q) - 1) \qquad \text{Equation 2-18}$$

where Q is the momentum transferred of scattering particle during the scattering process.

Total scattering structure functions S(Q) are different from conventional powder diffraction in the Q-range studied. In total-scattering experiments, the S(Q) must be measured over a wide range of Q-values, potentially 30-50 $Å^{-1}$ for highest real-space resolution while conventional powder diffraction experiments typically go to a maximum Q around 8 $Å^{-1}$ and 16 $Å^{-1}$ for a Cu-K_α tube and Mo-K_α radiation, respectively.[15]

To analyze the total scattering data, the model can be fitted in reciprocal-space which is in turn Fourier transformed to real-space to obtain the PDF. The reduced pair distribution function, G(r), is determined by a Fourier transform of the obtained experimentally total-scattering structure function, S(Q), according to

$$G(r) = \frac{2}{\pi}\int_0^{\infty} Q[S(Q) - 1]\, sin(Qr)\, dQ \qquad \text{Equation 2-19}$$

where S(Q) is the corrected and normalized total-scattering structure function, Q is the magnitude of the scattering vector, and r is the distance between the two atoms. Figure 2-5 shows the steps for obtaining pair distribution function data and analysis.

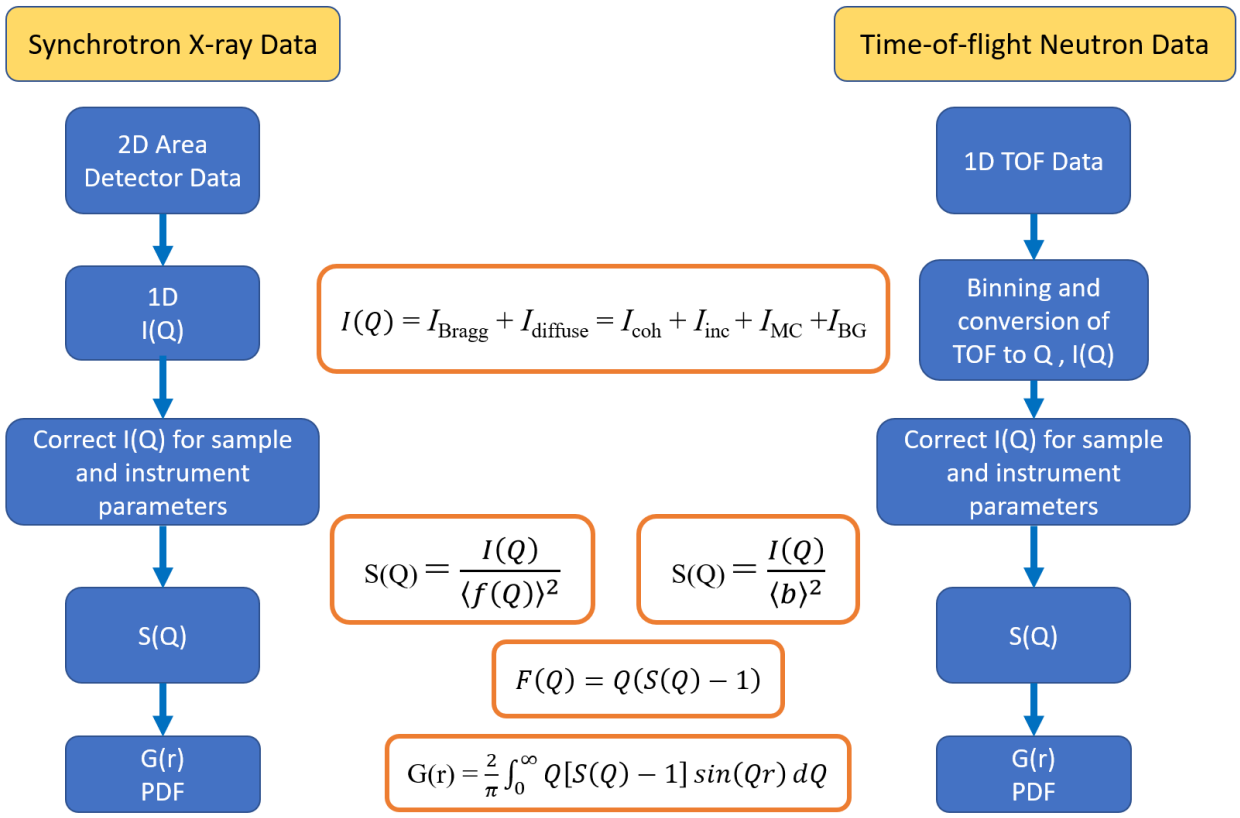

Figure 2- 5: Steps for obtaining pair distribution function data and analysis

2.3.4. Why is atomic pair distribution function useful?

The atomic pair distribution function contains structural and size information of a material that can be easily measured experimentally. It is also calculated from a known structure and provides local correlation of the structure. Since the PDF is a real-space function, structural information can be obtained directly by just looking from the PDF peaks as illustrated in Figure 2-6. The peak position in the PDF indicates the existence of a pair of atoms with that separation including the average bond lengths and interatomic distances. The integral intensity of PDF peaks yields information about average coordination properties, which is also related to the scattering power of the atoms involved. For example, a PDF peak corresponding to a Pb-Pb pair will be much larger than between two oxygen atoms. The width of a PDF peak reveals the distribution of atom-atom distances and thermal motion of the atoms, or static disorder. The broader the peak, the larger the distribution of the distances. This could arise from dynamic structural disorder due to thermal atomic motions or vibration of atoms along its lattice point. The PDF peak width also depends on a doping or nanosize induced disorder leading to static structural disorder.[12]

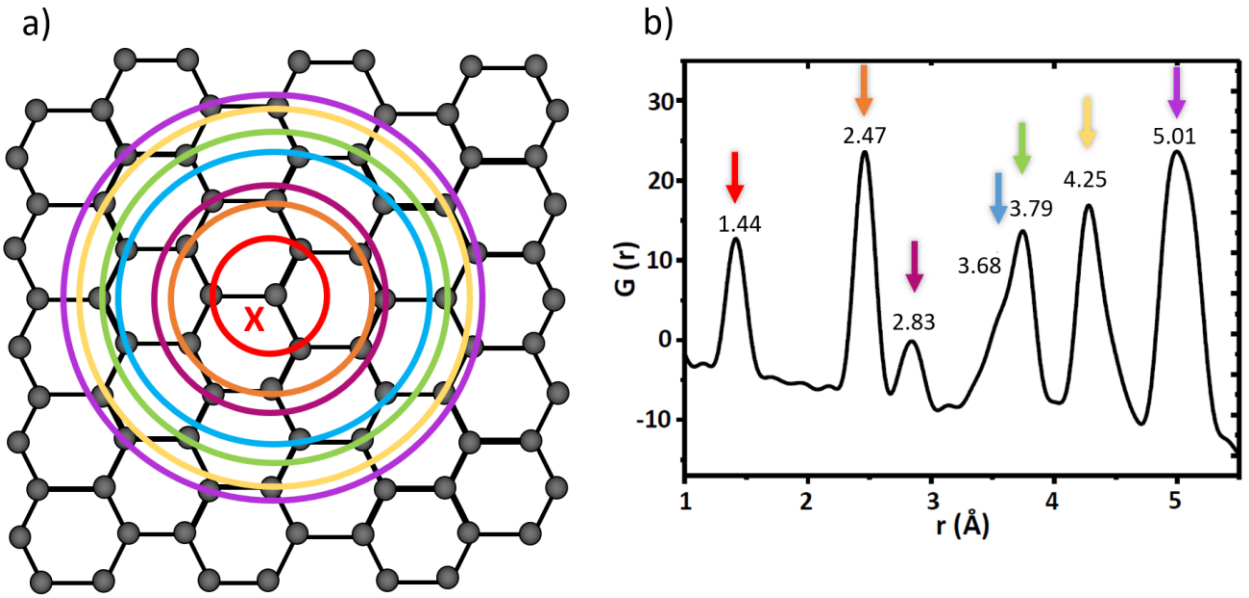

Figure 2- 6: Schematic of the modelling of process of finding an atom at a distance r from a given atom using PDF. Starting with the central atom X in the structure shown in the left panel, there are 3 nearest neighboring atoms at 1.44 Å away representing as the intensity at 1.44 Å for the PDF in the right panel. Then another set of atoms can be found at 2.47Å away from the central atom as well as the second peak in PDF, ect. The area under the second peak is greater than that of the first peak because there are more pairs contribute to that distance.

2.3.5. Synchrotron X-ray and neutron scattering studies

Synchrotron and neutron powder diffraction studies play an important role in structural solid-state chemistry such as providing characteristic fingerprint of a compound for qualitative analysis and precisely providing the detailed structures of crystalline compounds. Most of crystal structure determinations are performed using laboratory X-ray source, but there are some compounds whose crystalline structure information are difficult to determine. The features distinguishing synchrotron X-rays from conventional X-rays source is the high intensity and the continuous spectral distribution.[16] In addition, the high-resolution measurements can be uniquely

used to investigate the subtle phase transitions that are found in some materials such as ferroelectrics.[17] The synchrotron X-ray diffraction is also advantageous in detecting the presence and quantity of different elements, and differentiating between different oxidation states of an element.

Because neutrons are scattered by the nucleus of atoms unlike X-rays which are scattered by the electrons, there is only a weak dependence upon atomic number for neutron scattering. This property has led to different applications of neutron diffraction in solid-state chemistry including probing precisely the location of light atoms such as oxygen in the presence of elements. In addition, atoms that are adjacent in the periodic table have similar numbers of electrons, and thus their X-ray scattering powers are identical. Therefore, neutron diffraction will be beneficial to differentiating between elements adjacent to each other in the periodic table. Neutron diffraction is also a powerful technique for studying the magnetic structure of materials. Since neutrons possess magnetic dipole moment, they are diffracted by both atomic nuclei and unpaired electrons when interacting with unpaired electrons.[1] Additional peaks contain information about the spin arrangement will appear in the diffraction patterns.

In this thesis, a complementary of synchrotron X-rays PDF and time-of-flight neutron PDF is employed to probe the interatomic distance between lead and oxygen in the mixed-anion $PbVO_3Cl$ and pyrochlore $Pb_{1.5}Nb_2O_{6.5}$. The PDF data reveals that Pb–O interatomic distance in $PbVO_3Cl$ compound decrease upon heating, while Pb–Cl distance are only affected by thermal motion. Hence, the change in Pb–O interatomic distance upon heating is responsible for the thermochromic behavior at 200 °C in this material. Joint X-ray PDF and neutron PDF data showed the local structure in the cubic pyrochlore $Pb_{1.5}Nb_2O_{6.5}$ material is best described by the cristobalite

structure at 100 K, 200 K, and 300 K. The cristobalite structure also better describes the data out to long length scales upon cooling suggesting a long-range structural transition upon cooling.

2.3.6. Where is PDF data collected?

X-ray pair distribution function (XPDF) experiments are mostly carried out at X-ray synchrotron facilities using high incident energy X-rays. The first synchrotron experiments were carried out at the Cornell High Energy Synchrotron Source (CHESS) and the National Synchrotron Light Source II (NSLS-II) at the Brookhaven National Lab.[18-19] Several dedicated X-ray beamlines such as 11ID-B and 11ID-C have also been constructed at the Advanced Photon Source (APS) of Argonne National Laboratory (ANL) in Lemont, IL, USA.

The neutron pair distribution function (NPDF) experiments using neutron diffractometers require time-of-flight neutron sources that can be carried out at the Manuel Lujan Neutron Scattering Center (MLNSC)[20] at Los Alamos National Laboratory (LANL), Spallation Neutron Source (SNS) at Oak Ridge National Laboratory (ORNL), and National Institute of Standard and Technology (NIST) Center for Neutron Research. Several instruments at SNS facility employed for PDF studies include Nanoscale-Ordered Materials Diffractometer (NOMAD) at BL-1B, Spallation Neutrons and Pressure Diffractometer (SNAP) at BL-3, and Powder Diffractometer (POWGEN) at BL-11A. These are instruments available at the time of this writing. There are more facilities available for PDF measurements in the U.S. and the world, and it can change in the future.

2.3.7. PDF refinement

The pair distribution functions, G(r), can be obtained by the transformation of the normalized total scattering functions, S(Q), using the program PDFgetX2, or PDFgetX3, with a selected Q_{max}.[21-22] Local structure is then investigated by least-square refinement of the real-space

PDF data using the PDFgui software suite. A good PDF is obtained when the sample is collected with high maximum momentum transfer, high Q resolution, good counting statistics at high Q, and low instrument background. The purpose of PDF quantitative analysis is to fit a model to the average structure models determined from Rietveld refinement over specific ranges. The PDF refinement can be started with peak fitting in which the PDF peak positions and widths of the model are fitted to the observed scattering data. The PDF widths are then fitted as a function of r for correlated motion. PDF data can be refined with small box modelling using PDFfit or PDFgui. This approach is for crystalline materials and a good check to see if the local structure matches the average structure. The other possibility in the PDF refinement is large box approach – reverse Monte Carlo (RMC) modeling – which will not be discussed in detail in this document. This modeling approach simply a general method of structural modeling based on experimental data. In addition to applying the small box and large box RMC techniques to study the disordered crystalline materials, these techniques are used to study amorphous materials, liquids, and glasses.[23-25] The sample parameters in the PDF refinement includes scale factor, lattice parameters, atomic positions expressed in fractional coordinates, anisotropic thermal parameters for each atom, and the average atomic occupancy.[26]

A distinct local structure may be possible when an average structure model fails to explain observed material properties. For example, the average structure from X-ray diffraction data did not explain the thermochromic behavior in $PbVO_3Cl$.[27] Information about the coordination number can be extracted by integrating the intensity under that peak and fitting that peak with a series of Gaussian functions.[28] As the PDF refinement progresses, signatures of disorder can be found through complementary methods. Thermal motion or static displacements of atoms, which are known as atomic disorder, give rise to a distribution of atom-atom distances.[28] Therefore, PDF

peaks are often broadened with the presence of atomic disorder. For instance, a non-Gaussian PDF peak may indicate an anharmonic crystal potential. The refinement can be terminated when a best-fit of the PDF calculated from the model and the PDF data is obtained.

For this thesis, I mainly focus on performing structural analysis using Rietveld and PDF refinement methods. Rietveld refinement is performed on the synchrotron X-ray and neutron data of crystalline samples using the General Structure Analysis System II (GSAS-II) crystallographic analysis suite[29] to obtain average structure of the powder samples. The average structures are then used as a model to fit the PDF data, G(r), during the PDF refinement with small box modelling approach using PDFgui software suite to investigate the local structures. The refined structures are finally visualized using the Visualization for Electronic and Structural Analysis (VESTA) suite of program[30] for interatomic distances and bond angles that are restrained in Rietveld analysis.

2.4. References

1. West, A. R., Basic Solid State Chemistry. Second ed.; John Wiley & Sons Ltd: New york, 2000.
2. Leng, Y., Materials Characterization: Introduction to Microscopic and Spectroscopic Methods. Wiley, 2008.
3. Rietveld, H. M., Line Profiles of Neutron Powder-Diffraction Peaks for Structure Refinement. *Acta Cryst.* **1967,** *22*, 151.
4. Pawley, G. S., Unit-Cell Refinement from Powder Diffraction Scans. *J. Appl. Cryst.* **1981,** *14*, 357.
5. Bail, A. L.; Duroy, H.; Fourquet, J. L., *Ab initio* Structure Determination of $LiSbWO_6$ by X-Ray Powder Diffraction. *Mater. Res. Bull.* **1988,** *23*, 447.
6. Loopstra, B. O.; Rietveld, H. M., Further Refinement of the Structure of WO_3. *Acta Cryst.* **1969,** *B25*, 1420.
7. Pecharsky, V. K.; Zavalij, P. Y., *Fundamentals of Powder Diffraction and Structural Characterization of Materials*. Kluwer Academic Publishers: NY, USA, **2003**.
8. Degen, T.; Sadki, M.; Bron, E.; Konig, U.; Nenert, G., The HighScore suite. *Powder Diffr.* **2014,** *29*, S13-S18.
9. Young, R. A., *The Rietveld Method*. Oxford University Press, Oxford, **1991**.
10. Altomare, A.; Capitelli, F.; Corriero, N.; Cuocci, C.; Falcicchio, A.; Moliterni, A.; Rizzi, R., The Rietveld Refinement in the EXPO Software: A Powerful Tool at the End of the Elaborate Crystal Structure Solution Pathway. *Crystals* **2018,** *8* (5).
11. Proffen, T.; Billinge, S. J. L.; Egami, T.; Louca, D., Structural Analysis of Complex Materials Using the Atomic Pair Distribution Function - a Practical Guide. *Z. Kristallog.* **2003,** *218* (2), 132-143.
12. Billinge, S. J. L., Nanometer Scale Structure from Powder Diffraction: Total Scattering and Atomic Pair Distribution Function Analysis. *International Tables of Crystallography* **2019,** *H*, 649-672.
13. Petkov, V.; Jeong, I.-K.; Chung, J. S.; Thorpe, M. F.; Kycia, S.; Billinge, S. J. L., High Real-Space Resolution Measurement of the Local Structure of $Ga_{1-x}In_xAs$ Using X-Ray Diffraction. *Phys. Rev.* **1999,** *83*, 4089-4092.
14. Billinge, S. J. L., The Rise of the X-Ray Atomic Pair Distribution Function Method: a Series of Fortunate Events. *Philos. Trans. R. Soc. A* **2019,** *377* (2147).
15. Egami, T.; Billinge, S. J. L., *Underneath the Bragg Peaks: Structural Analysis of Complex Materials*. Oxford: Elsevier, 2003; Vol. 7.
16. Carrondo, M. A.; Jeffery, G. A., Chemical Crystallography with Pulsed Neutrons and Synchrotron X-Rays. *React. Kinet. Catal. Lett.* **1988,** *37* (1), 251-254.
17. Laurita, G.; Hickox-Young, D.; Husremovic, S.; Li, J.; Sleight, A. W.; Macaluso, R.; Rondinelli, J. M.; Subramanian, M. A., Covalency-Driven Structural Evolution in the Polar Pyrochlore Series $Cd_2Nb_2O_{7-x}S_x$. *Chem. Mater.* **2019,** *31*, 7626−7637.

18. Aur, S.; Kofalt, D.; Waseda, Y.; Egami, T.; Wang, R.; Chen, H. S.; Teo, B. K., Local Structure of Amorphous $MO_{50}Ni_{50}$ Determined by Anomalous X-ray Scattering using Synchrotron Radiation. *Solid State Commun.* **1983,** *48*, 111-115.
19. Kofalt, D. D.; Nanao, S.; Egami, T.; Wong, K. M.; Poon, S. J., Differential Anomalous-X-Ray-Scattering Studies of Icosahedral and Amorphous $Pd_{58.8}U_{20.6}Si_{20.6}$. *Phys. Rev. Lett.* **1986,** *57*, 114-117.
20. Proffen, T.; Egami, T.; Billinge, S. J. L.; Cheetham, A. K.; Louca, D.; Parise, J. B., Building a High Resolution Total Scattering Powder Diffractometer – Upgrade of NPD at MLNSC. *Appl. Phys. A: Mater. Sci. Process* **2002,** *74*, S163-S165.
21. Qiu, X. H.; Thompson, J. W.; Billinge, S. J. L., PDFgetX2: a GUI-Driven Program to Obtain the Pair Distribution Function From X-ray Powder Diffraction Data. *J. Appl. Cryst.* **2004,** *37*, 678.
22. Juhás, P.; Davis, T.; Farrow, C. L.; Billinge, S. J. L., PDFgetX3: a Rapid and Highly Automatable Program for Processing Powder Diffraction Data into Total Scattering Pair Distribution Functions. *J. Appl. Cryst.* **2013,** *46*, 560-566.
23. McGreevy, R. L.; Howe, M. A., The Structure of Molten LiCl. *J. Phys. Cond. Mat.* **1989,** *1* (49), 9957-9962.
24. Nield, V. M.; Keen, D. A.; Hayes, W.; McGreevy, R. L., Structural Changes in silver bromide at the Melting Point. *J. Phys. Cond. Mat.* **1992,** *4* (32), 6703-6714.
25. Pusztai, L.; Svab, E., Modelling the Structure of $Ni_{65}B_{35}$ Metallic Glass by Reverse Monte Carlo Simulation. *J. Phys. Cond. Mat.* **1993,** *5* (47), 8815-8828.
26. Farrow, C.; Juhás, P.; Liu, J.; Bryndin, D.; Božin, E.; Bloch, J.; Proffen, T.; Billinge, S. J. L. *PDFgui User Guide*, Board of Trustees of Columbia University in the City of New York: **2016**.
27. Dang, U.; Zaheer, W.; Zhou, W. Y.; Kandel, A.; Orr, M.; Schwenz, R. W.; Laurita, G.; Banerjee, S.; Macaluso, R. T., Lattice Anharmonicity of Stereochemically Active Lone Pairs Controls Thermochromic Band Gap Reduction of $PbVO_3Cl$. *Chem. Mater.* **2020,** *32* (17), 7404-7412.
28. Billinge, S. J. L., *Pair Distribution Function Technique: Principles and Methods*. Springer, Dordrecht, The Netherlands, **2012**.
29. Toby, B. H.; Dreele, R. B. V., GSAS-II: the Genesis of a Modern Open-Source all Purpose Crystallography Software Package. *J. Appl. Cryst.* **2013,** *46*, 544-549.
30. Momma, K.; Izumi, F., VESTA 3 for Three-Dimensional Visualization of Crystal, Volumetric and Morphology Data. *J. Appl. Cryst.* **2011,** *44*, 1272-1276.

Chapter 3 Anharmonicity of Stereochemically Active Lone Pairs Controls Thermochromic Band Gap Reduction of $PbVO_3Cl$

Reprinted with permission from U. Dang, W. Zaheer, W. Zhou, A. Kandel, M. Orr, R. W. Schwenz, G. Laurita, S. Banerjee, and R. T. Macaluso. Lattice Anharmonicity of Stereochemically Active Lone Pairs Controls Thermochromic Band Gap Reduction of $PbVO_3Cl$. **2020**, *32*, (17), 7404-7412.

Abstract

Stereochemically active lone pairs of electrons play an important role in a diverse range of physical phenomena in many materials, ranging from semiconducting halide perovskites to thermochromic inorganic-organic hybrids. In this paper, we demonstrate the importance of the $6s^2$ lone pair on the reversible thermochromic transition in the mixed-anion inorganic compound, $PbVO_3Cl$. This $6s^2$ stereochemically active lone pair results in subtle structural distortions upon heating while maintaining its overall orthorhombic structure. These distortions result in competing interactions with the Pb $6s^2$ lone pair and ultimately, a pronounced change between yellow and red at ~200 °C. X-ray diffraction analyses of $PbVO_3Cl$ demonstrate two-dimensional features in contrast to the three-dimensional network in isostructural $BaVO_3Cl$. X-ray and neutron pair distribution function experiments reveal that Pb-O interatomic distances decrease upon heating, while Pb-Cl distances are only affected by thermal motion. X-ray photoelectron spectroscopy measurements provide experimental evidence of the presence of the $6s^2$ lone pair at the valence band maximum, which are corroborated by first-principles calculations. The results demonstrate a broadly generalizable mechanism for using repulsions between lone-pair electrons of *p*-block cations to drive discontinuous changes of local symmetry and electronic structure.

3.1. Introduction

Mixed-anion systems, e.g., oxynitrides, oxysulfides and oxyhalides, stand out as a class of materials because of the tunability of atomic and electronic structure and therefore, semiconducting band gaps.[1-4] Mixed-anion systems containing stereochemically active lone pairs are particularly interesting because structural distortions associated with the lone pairs contribute to magnetic,[5] photocatalytic,[3]and nonlinear optical behavior.[6-8] Comparing $PbBi_2OX$ (X = Cl, Br, I) to *AE*Bi_2OCl (*AE* = Sr, Ba) demonstrated that the hybridization between the $6s^2$ lone pair and O 2*p* resulted in an upward shift of the valence band (VB) in $PbBi_2OX$ (X = Cl, Br, I), thereby making it a potential visible light-induced water splitting catalyst.[3] Thermochromic transitions due to disorder associated with $5s^2$ lone pairs have been recently described for the organic-inorganic hybrid (2-MIm)SbI_4 (MIm – methylimidiazolium).[9] However, lone-pair-driven electronic instabilities bringing about a pronounced modulation of electronic structure are much less explored in all-inorganic systems.

Stereochemically active lone pairs derived from *p*-block cations have long been understood to affect structural distortions.[10] It is important to point out that in inorganic solids, stability of structural distortions associated with stereochemically active lone pairs are closely connected to lone pair-anion interactions.[11] For example, in the halide perovskite, $CsSnBr_3$, small, localized distortions invoked by the Sn 5*s*-Br 4*p* interactions play an important role in dielectric and optical behavior.[12] The unusual band gap widening with temperature of PbS, PbSe, and PbTe semiconductors has also been attributed to the emphanisis effect, in which the Pb^{2+} lone pairs become stereochemically active upon warming, leading to local distortions at elevated temperatures.[13-15] The link between lone pair-anion interactions and structural distortion is strongly justified by the combination of experimental spectroscopic evidence and a theoretical

revised lone pair model,[10, 15] leading to promising predictive abilities in the area of catalysis. For instance, the hybridization of Pb $6s^2$ or Sn $5s^2$ states with O 2*p* states in β-$Pb_xV_2O_5$ and β-$Sn_xV_2O_5$ yields a combination of occupied bonding and anti-bonding lone-pair—anion states. The latter is further stabilized by mixing with unoccupied cation 5 and 6 *p*-states, yielding an occupied hybrid "mid-gap" state above the O 2*p* valence band[2, 16-17] with a distinctive spectroscopic signature distinguishable by hard X-ray photoemission spectroscopy. Such lone-pair-derived mid-gap states have been utilized to extract holes from photoexcited II-VI quantum dots, enabling the design of heterostructures for water splitting and mitigating the longstanding challenge of photo-anodic corrosion of chalcogenide quantum dots that has limited their use in photocatalysis.

This paper establishes the unique effect of thermally induced structural distortions derived from a stereochemically active lone pair on a thermochromic transition in the mixed-anion inorganic compound, $PbVO_3Cl$. Previous work on this material was motivated by the Pb $6s^2$ lone pairs.[18] Unlike other mixed anion compounds containing lone pairs where the harder cation interacts with the oxide while the softer metal interacts with the softer anion, e.g., chalcogenide or halide, the $6s^2$ lone pairs in $PbVO_3Cl$ simultaneously interact with both O and Cl, and thus $PbVO_3Cl$ presents a special opportunity to evaluate the structural stability of lone pair interactions with anions of very different electronegativities. We show that thermally driven electrostatic repulsions between stereochemically active lone pairs on $PbCl_4$ units and the concomitant lattice distortion alters the hybridization of Pb $6s^2$ lone pair states with O 2*p* states, resulting in a thermochromic transition at ~200°C, which brings about a reversible color change between yellow and red because of local distortions of the atomic structure strongly coupled with modulation of the electronic structure. $BaVO_3Cl$, which does not contain a stereochemically active lone pair of electrons, was also prepared as a control for the comparison of the local structure of the two

compounds. Total X-ray and neutron scattering were used to elucidate long and short-range crystal structures as a function of temperature. Density functional theory (DFT) calculations in conjunction with X-ray absorption near-edge structure (XANES) and hard X-ray spectroscopies (HAXPES) provide theoretical and experimental evidence of the key involvement of the Pb $6s^2$ lone pair in the electronic structure of $PbVO_3Cl$.

3.2. Materials and Methods

3.2.1. Synthesis

Powder samples of $PbVO_3Cl$ were prepared in a manner similar to procedures described elsewhere.[18] A mixture of PbO, $PbCl_2$, and V_2O_5 in a 1:1:1 molar ratio was ground in an agate mortar and pestle. The powders were pressed into a pellet and placed inside a fused silica ampoule. The ampoule was subsequently sealed under vacuum, heated at 3 °C/min to 450 °C, where it dwelled for 12 hours, and then cooled to 25 °C at 3 °C/min. The product was visibly yellow with a typical yield of ~86%. The impurity was found to be $PbCl_2$ which could be removed by washing the sample with DI water.

The synthesis of $BaVO_3Cl$ was based on a previously reported two-step procedure.[19] First, V_2O_5 and $BaCO_3$ were ground in an agate mortar and pestle and placed in a platinum crucible. The mixture was heated at 5.6 °C/min to 700 °C, where it dwelled for 6 hours, and then cooled to 25 °C at 5.6 °C/min to yield BaV_2O_6. In the second step, a mixture of $BaCl_2$ and BaV_2O_6 in a 1:1 molar ratio was ground, pressed into pellet, placed in a fused silica ampoule and sealed under vacuum. The sample was heated at 30 °C/h to 480 °C, where it dwelled for 24 hours and then cooled at 8 °C/h down to 300 °C. The ampoule was removed from the furnace and quenched in an ice bath. The powder product was visible yellow with typical yields determined by X-ray powder diffraction of ~91% to ~94%.

Safety Precautions: Pb and V containing compounds cause irritation on contact with the body. Ingestion of these compounds is toxic. Follow normal laboratory safety procedure by wearing gloves, wearing goggles, working in a vent hood, and avoiding any direct contact with the chemicals.

3.2.2. Structural Characterization

3.2.2.1. Powder X-ray Diffraction

Powder X-ray diffraction (XRD) data were collected using a PANalytical Empyrean diffractometer equipped with a PIXcel^{3D} detector and Cu (λ = 1.5405980 Å) tube, which was operated at 45 kV and 40 mA. Data were collected over the angular range $10° \leq 2\theta \leq 90°$ with a step width of 0.008° and step rate of 0.0557 °/s at room temperature. The background was estimated by a polynomial function varying four coefficients. Atomic coordinates, scale factor, peak shape function (U, V, W), and isotropic displacement parameters were refined.

3.2.2.2. Total Scattering Measurements

Time-of-flight (TOF) neutron scattering data were collected at 100, 300, and 500 K on the nanoscale ordered materials diffractometer (NOMAD) at the Spallation Neutron Source (SNS), Oak Ridge National Laboratory (ORNL) with a collection time of approximately 2 to 4 h per sample.[20] The samples were loaded into quartz capillaries and an empty capillary was subtracted as background. The pair distribution functions (PDF), *G(r)*, were obtained by the transformation of the normalized total scattering function, *S(Q)*, with a Q_{max} = 28.0 Å^{-1}.

Synchrotron X-ray total scattering measurements were collected on the 11-ID-B beamline at the Advanced Photon Source (APS) located at Argonne National Laboratory (ANL) with a photon wavelength of 0.1432 Å from 300 to 575 K. Samples of fine powder were transferred into

a Kapton capillary (1.1 mm OD, 1.0 mm ID) tightly compacted by glass wool to ensure the maximum packing fraction. The two samples were separated in the capillary by glass wool. Data were collected every 2 min upon warming at a rate of 5 K min^{-1}. Corrections to obtain the *S(Q)* and subsequent Fourier transform with a Q_{max} of 27.55 $Å^{-1}$ to obtain the *G(r)* was performed using the program PDFgetX2.[21] The local structure was investigated via analysis of the real-space PDF using the PDFgui software suite.[22] Crystal structures were visualized using the VESTA suite of programs.[23]

3.2.2.3. Density Functional Theory

First-principles calculations were performed using density functional theory, as implemented within the Vienna *ab initio* simulation package (VASP). The projector augmented wave (PAW) formalism was used to model electron−ion interactions.[24-28]A kinetic energy cutoff of 520 eV was used for plane-wave basis restriction. Electronic exchange and correlation effects were included using the generalized gradient approximation based on the Perdew−Burke−Ernzerhof functional (GGA-PBE).[27] The strong electronic correlation of the V 3*d* electrons was accounted for using a Hubbard correction U_{eff} = 3.25 eV.[32] Supercells with dimensions 1 × 2 × 2 were used to relax the $PbVO_3Cl$ and $BaVO_3Cl$ structures. For geometry optimization, the supercells were relaxed until the cartesian components of the forces were below ±0.01 eV·$Å^{-1}$. A uniform Γ-centered 6 × 6 × 4 Monkhorst−Pack *k*-point grid was used for structure relaxations and density of states (DOS) calculations. Self-Consistent Field (SCF) DFT calculations were further performed as implemented in VASP on structural models derived from the refinement of PDF data. Refined PDF data collected over a range of 1—4.5Å at 300 K and 570 K was used for SCF calculations.

3.2.2.4. Hard X-ray Photoelectron Spectroscopy

Valence band HAXPES measurements were performed at the National Institute of Standards and Technology beamline 7-ID-2 of the National Synchrotron Light Source II at the Brookhaven National Laboratory. Measurements at an incident photon energy of 2 keV were performed with a pass energy of 200 eV, whereas the measurements at the incident photon energy of 5 keV were collected at a pass energy of 500 eV. The data was collected with a step size of 0.85 eV and the analyzer axis oriented parallel with the photoelectron polarization vector. The higher excitation of HAXPES circumvents deleterious charging issues that are common to ultraviolet and soft X-ray photoelectron spectroscopy. Photon energy selection was accomplished using a double Si (111) crystal monochromator. No evidence of charging was observed during our measurements. The beam energy was aligned to the Fermi level of a silver foil before measurements.

3.2.2.5. X-ray Absorption Near-Edge Structure Spectroscopy

V L-edge and O K-edge measurements were performed at beamline 7-ID-1 of the National Synchrotron Light Source II of Brookhaven National Laboratory device beamline operated by the National Institute of Standards and Technology. A horizontally polarized x-ray beam with a spot size of 10 μm was used for data collection. A grid bias of -300 V was used to reduce the low-energy electrons and improve surface sensitivity. A charge compensation gun was used to avert the charging of the samples. The data was collected with a resolution of 0.5 eV for all plotted spectra. The partial electron yield signals were normalized to the incident beam intensity from a freshly evaporated gold mesh. The spectra were energy calibrated to O K-edge for a standard TiO_2 sample.

3.3. Results and Discussion

3.3.1. Average Crystal Structure

Both $PbVO_3Cl$ and $BaVO_3Cl$ adopt the orthorhombic *Pnma* space group, in agreement with previous structural reports.[18] Results from powder X-ray diffraction analyses of both compounds are provided in Tables 3-S1 and 3-S2. X-ray fluorescence results (Table 3-S3) indicate 1 mol Pb:1 mol V ratio, in agreement with powder XRD.

Since $PbVO_3Cl$ and $BaVO_3Cl$ share the same space group and atomic positions, similarities in their crystal structures are expected. Their crystal structures are compared in Figures 3-1a and 3-1b. Both compounds include chains of edge-sharing VO_5 square pyramids running in the *b* direction. Square pyramids within a chain are in a *trans*-configuration in which the apical oxygen points alternately in the *ac* plane as shown in Figure 3-1a. The VO_5 square pyramids in both compounds are similarly distorted. The vanadium atom is slightly off-center in the VO_5 square pyramid with a short doubly bonded apical V-O bond (1.599 - 1.611 Å) and four long bonds of 1.824 - 1.920 Å and of 1.805 - 1.956 Å for Pb and Ba, respectively. These results agree with previous structural reports.[18]

In both compounds, the chains are connected by the divalent cation (Pb^{2+} or Ba^{2+}); however, the connectivity of Pb^{2+} is distinct from its Ba^{2+} counterpart. Each BaO_5Cl_4 polyhedron in $BaVO_3Cl$ connects to the oxygen atoms of three unique VO_5 square pyramids to form a three-dimensional network as shown in Figure 3-1b. In $PbVO_3Cl$, on the other hand, each PbO_3Cl_3 polyhedron connects two VO_5 square pyramids from two neighboring chains, resulting in two-dimensional sheets in the *bc* plane, with a clear separation between layers of ~3.3 Å. This interlayer separation and coordinate undersaturation of the main-group cation is diagnostic of the role of stereoactive lone pairs, which have an approximate volume of an oxide or fluoride ion.

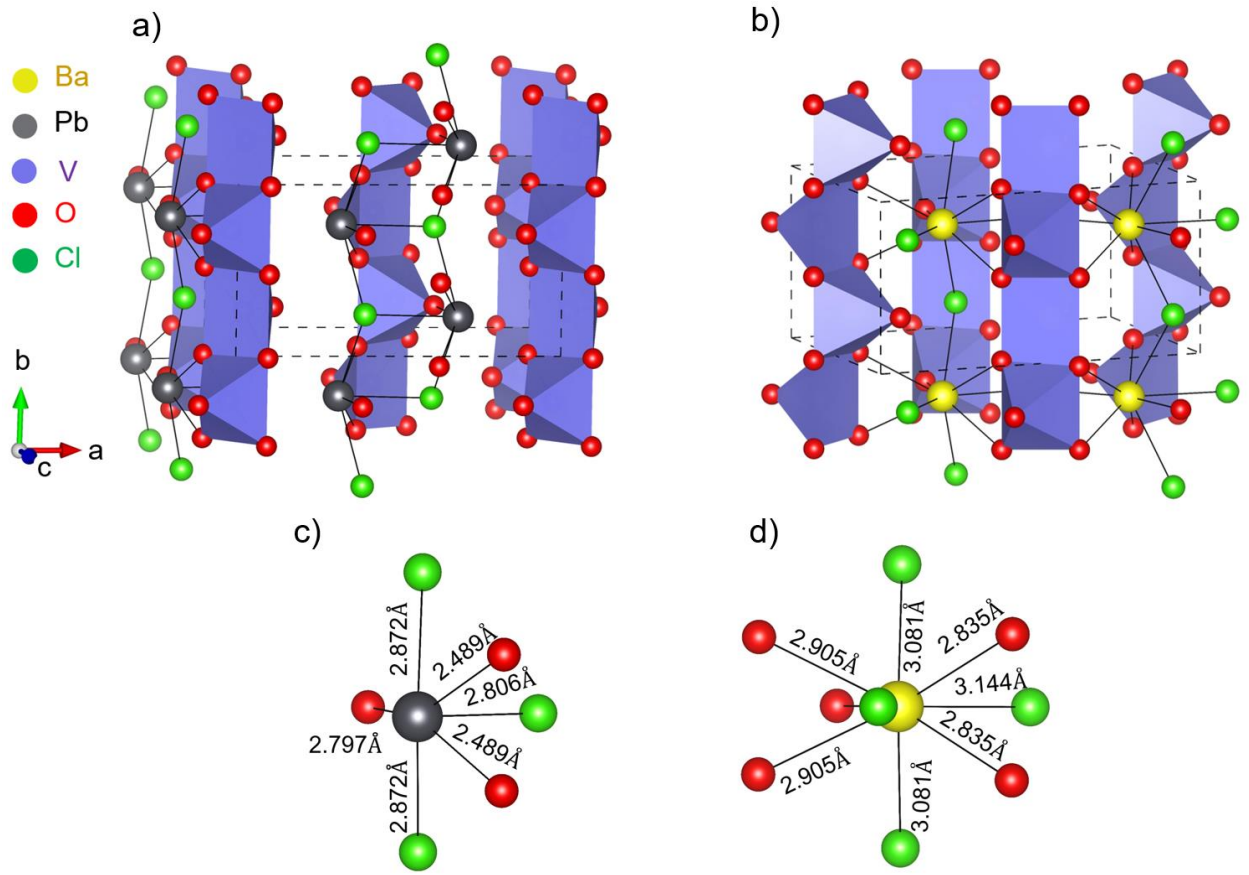

Figure 3-1: Average crystal structures of (a) $PbVO_3Cl$ and b) $BaVO_3Cl$. Local coordination environments and interatomic distances of the divalent cation environment in (c) PbO_3Cl_3 and (d) BaO_5Cl_4 at room temperature.

Coordination environments around the divalent cations in $PbVO_3Cl$ and $BaVO_3Cl$ are depicted in Figures 3-1c and 3-1d, respectively. The Pb^{2+} cation is coordinated by three oxygen atoms and three chlorine atoms while Ba^{2+} is linked to five oxygen atoms and four chlorine atoms. Two of the oxygen atoms also form one edge of the VO_5 square pyramid base. Their interatomic distances – Pb-O and Pb-Cl and to that of Ba-O and Ba-Cl –are slightly shorter than bond distances calculated by summing their radii, Pb^{2+} (1.19 Å), Ba^{2+}(1.47 Å), O^{2-} (1.40 Å) and Cl^{-} (1.80 Å).[29]

3.3.2. Total Scattering

To better understand the local structure of the two samples, analysis of the X-ray Pair Distribution Function (XPDF) was performed. The PDF is a histogram of all atom-atom correlations in a material and incorporates both Bragg and diffuse scattering from a sample, representing the local bonding and atom-atom interactions. Therefore, by analyzing how well (or how poorly) the XPDF data is fit by the crystallographic *Pnma* structure, we can understand deficiencies in the model in the form of structural disorder. Fits of XPDF data, provided in Figure 3-2, against the structural model based on conventional laboratory X-ray diffraction for $PbVO_3Cl$ and $BaVO_3Cl$ illustrate that the average *Pnma* structure more accurately describes the local structure for $BaVO_3Cl$. Although the XPDF data agree well with the average structural model for all temperatures (all *Rw* values are between 7-10% for the fits over the *r*-range of 1-6Å), the peaks at ~2.5 – 2.8 Å, which arise from Pb-O and Pb-Cl pair correlations, are poorly described by the average structural model for $PbVO_3Cl$ at all temperatures, indicating that there is more disorder in the local coordination of Pb than the average structure can describe. In $BaVO_3Cl$, the analogous peaks (at ~2.9 – 3.0 Å) shift towards larger *r* as the temperature increases due to thermal expansion, yet the peak remains well fit. Pair correlations were determined from the partial neutron and X-ray pair distribution functions (Figure 3-S1). Additional fitting of the XPDF data over various length scales can be seen in Figures 3-S2 and 3-S3.

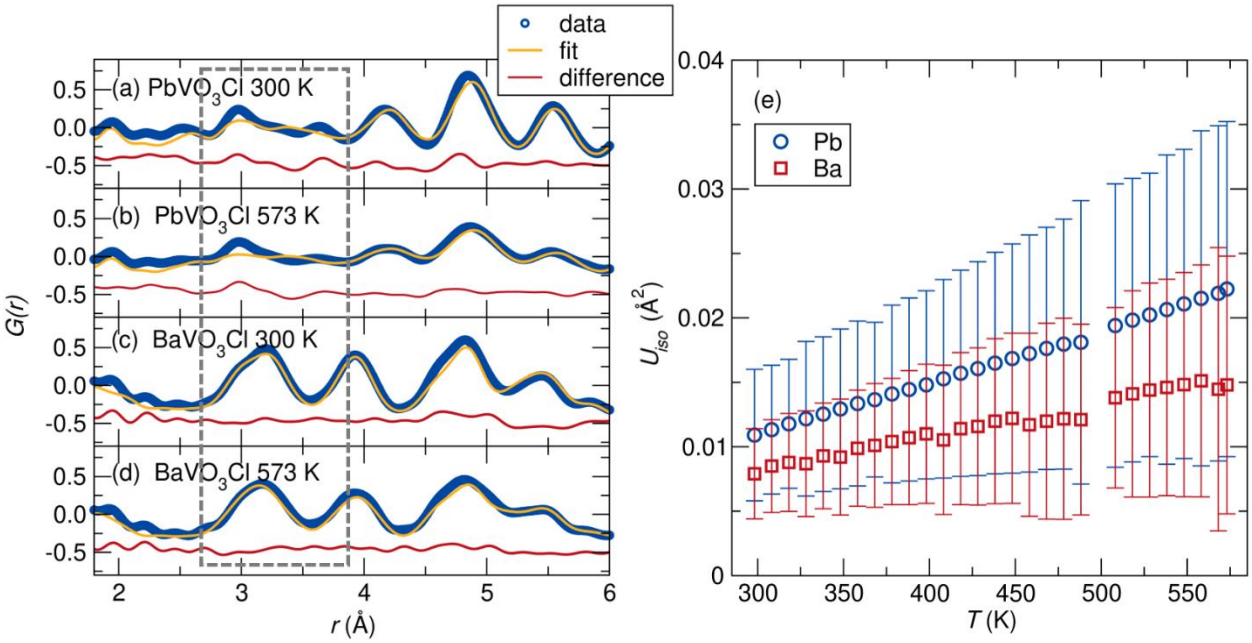

Figure 3- 2: Left: Fits of XPDF data against the average Pnma structures for $PbVO_3Cl$ [(a) 300 K and (b) 573 K and $BaVOCl_3$ [(c) 300 K and (d) 573 K]. Peaks highlighted in the dashed box indicate regions where the data is poorly fit in the Pb-analogue. Right: Isotropic atomic displacement parameters (U_{iso}) of Pb and Ba from XPDF data Isotropic atomic displacement parameters (U_{iso}) of Pb and Ba from XPDF data.

Atomic displacement parameters (ADP) provide insight into structural disorder. The unrealistically low U_{iso} of O1 obtained in our Rietveld refinements of powder X-ray diffraction data for $PbVO_3Cl$ (Table 3-S2) may be attributed to the relatively low scattering power of O (compared to Pb) or local disorder. Hence, we were motivated to investigate ADPs using pair distribution function using X-ray and neutron total scattering. Isotropic ADPs (U_{iso}) of Pb and Ba as a function of temperature are shown in the right panel of Figure 3-2. The U_{iso} values increase with temperature as expected with increasing thermal motion. Three additional trends in Figure 3-2b indicate the presence of the lone pair: consistently higher U_{iso} values, larger error and faster rate of increase of U_{iso} for $PbVO_3Cl$ with temperature. Because Pb ($Z = 82$) possesses more electron

density than Ba (Z = 56), it would be reasonable to anticipate that the U_{iso} of Pb to be smaller than U_{iso} of Ba; however, we observe the opposite trends at all temperatures, posited to arise from additional disorder from the stereochemically active lone pair of Pb^{2+}. Figure 3-3 provides a closer view of evolution of the XPDF data upon warming. The peak at ~3.0 Å indicates the Pb/Ba—Cl bond (see Supplemental Figure 3-S1 for partials), which remains relatively unchanged in shape upon warming. A large difference in peak shape corresponds to the Pb-Pb and Ba-Ba correlations at ~5.5 Å. The Pb-Pb correlation develops a notable asymmetry in comparison to Ba-Ba correlations, indicating that the Pb displacements lack long-range correlation. This asymmetry becomes more pronounced at higher temperatures.

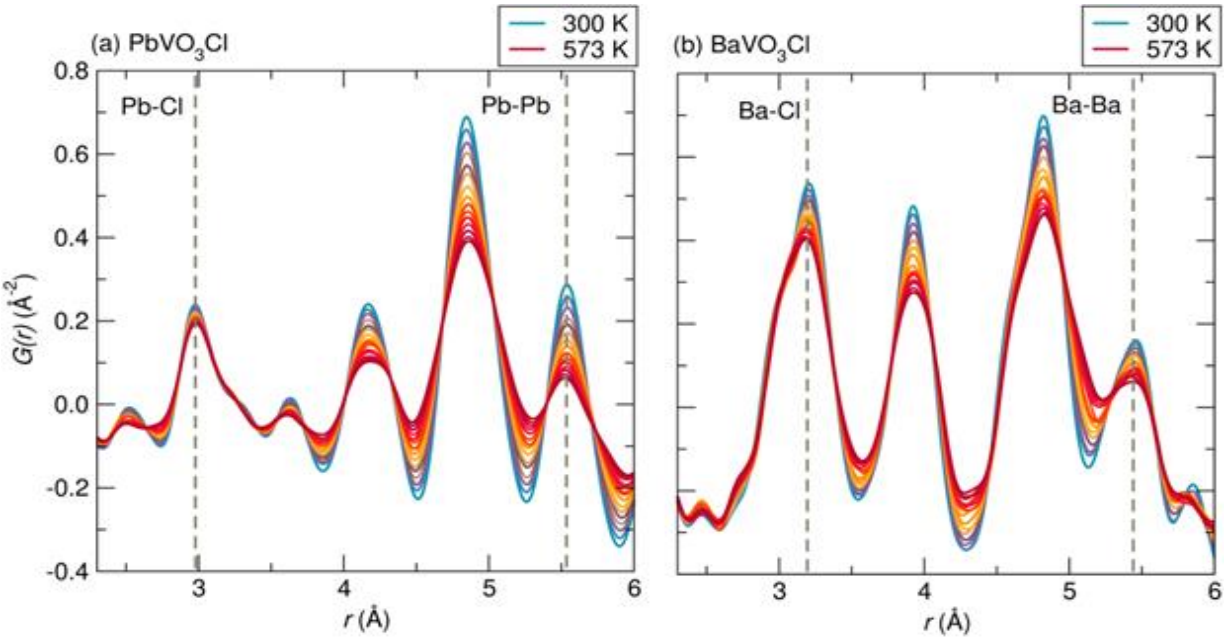

Figure 3- 3: XPDF data for (a) $PbVO_3Cl$ and (b) $BaVO_3Cl$ indicate that the Pb-Cl and Ba-Cl peak shape (indicated by a dashed line) remains relatively unchanged with temperatures, whereas the Pb-Pb correlation (indicated by a dashed line) develop a distinct asymmetry upon warming, in contrast to the same Ba-Ba correlation in $BaVO_3Cl$.

Because oxygen in the presence of lead has much higher scattering lengths via X-ray analysis, neutron pair distribution function (NPDF) data were collected to probe the oxygen environment. Fits of the neutron data against the *Pnma* structure can be found in Figure 3-S4. Interestingly, the positive temperature dependence of the Pb U_{iso} (Figure 3-4) agrees with the trends observed in the XPDF data (Figure 3-2b); however, the temperature dependence of the O U_{iso} and Cl U_{iso} remain consistent across the temperature range (Figure 3-4). The right panel of Figure 3-4 provides intriguing insight into the dynamics of the crystal structure with temperature. We observe that while the VO_5 square pyramids expand with increasing temperature as expected, the Pb-O distance *decreases* with temperature and results in overall smaller PbO_3Cl_3 polyhedra at higher temperatures. The Pb-Cl distance, however, is maintained at all temperatures, indicating that the primary structural effects on orbital overlap and thus observed physical properties are due to the changing Pb-O bond length. Therefore, the lone pair shifts towards oxygen are very subtle and that the pair distribution function is essential to identifying the structural changes resulting from the presence of the $6s^2$ lone pair. The displacement of Pb is also temperature-dependent, and the Pb atoms shift towards the 2D layer in which it already resides. While small-box modeling does provide insight into the presence of disorder (observed as a poor fit by the crystallographic structure), it is noted that PDFgui applies a harmonic approximation and thus generates Gaussian peak shapes.[23] Therefore, as the lattice becomes more anharmonic as a result of the lone pair stereochemistry, a Gaussian peak becomes a less accurate model of the data, resulting in larger error in the fit parameters. The anisotropy of the disorder will be further investigated with temperature-dependent single crystal X-ray diffraction studies.

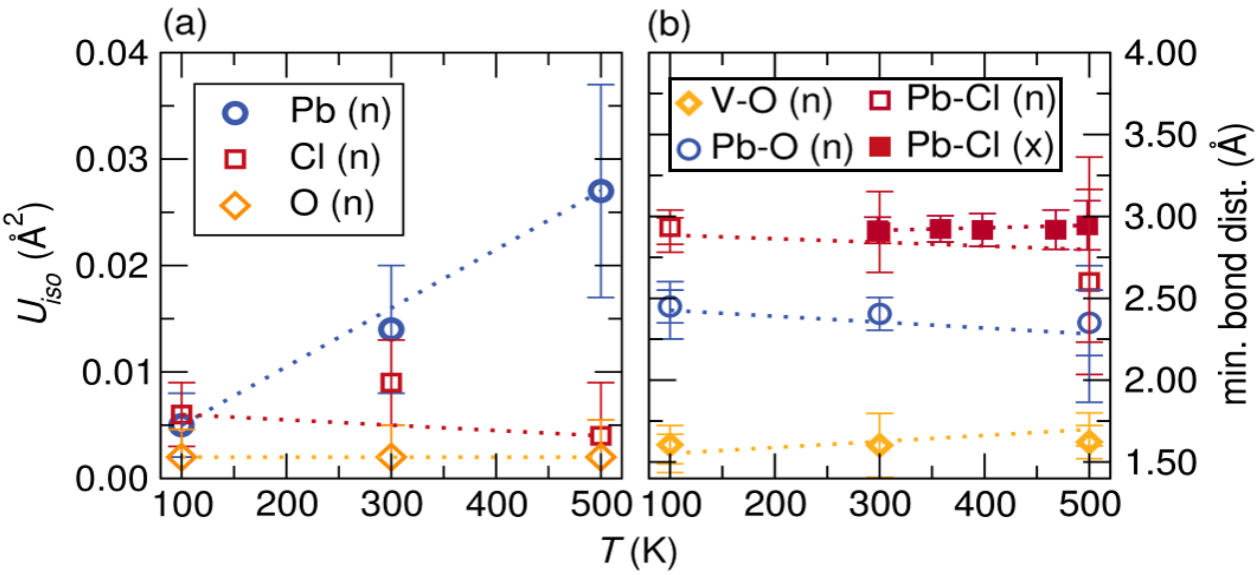

Figure 3-4: (a) Isotropic ADPs of Pb, Cl, and O and (b) V-O, Pb-O, and Pb-Cl distances with temperature.

To probe the electronic structure origin of the differences in the local atomic structure of $PbVO_3Cl$ and $BaVO_3Cl$, HAXPES measurements have been performed at incident photon energies of 2.0 and 5.0 keV. In contrast to XPS, which primarily probes surface electronic structure, the high excitation energies accessible in HAXPES enable interrogation of the bulk electronic structure. HAXPES further serves as an excellent, and indeed, quantitative probe of orbital contributions at the valence band.[16-17, 30] In general, photoionization cross-sections decay rapidly with an increase in incident photon energy; however, this effect is much more pronounced for subshells with higher orbital angular momentum.[31-33] Therefore, by varying the incident photon energy in photoemission experiments, the relative energy positioning and orbital contributions of states with *s*, *p*, and *d* character can be disentangled. Indeed, the relative spectral weights of different bands can be evaluated using energy-variant HAXPES.[34] Photoemission profiles obtained for both $PbVO_3Cl$ and $BaVO_3Cl$ at incident photon energies of 2.0 and 5.0 keV are plotted in Figures 3-5a and 5b.[16-17, 30] A direct comparison of the photoemission spectra of $PbVO_3Cl$ and

$BaVO_3Cl$ shows two major distinctions. First, a strong band centered at a binding energy of ~10.5 eV is observed for $PbVO_3Cl$ with no similar band for its *s*-block counterpart; the intensity of this feature increases with increasing incident photon energy, indicating the presence of electronic states with considerable Pb $6s^2$ character. Second, the valence band maximum of $PbVO_3Cl$ exhibits states higher up in energy (shaded as red in Figs. 3-5a and 3-5b) that are not observed for $BaVO_3Cl$. These states become more pronounced with an incident photon energy of 5.0 keV, again indicating their pronounced *s* character. The presence of these two features can be explained considering the revised lone pair model and are further assigned with the aid of DFT calculations. The hybridization of the Pb $6s^2$ stereoactive lone pairs with O 2*p* and Cl 3*p* states leads to the formation of hybrid Pb 6*s* – O 2*p* and Pb 6*s* – Cl 3*p* bonding (B) and antibonding states (AB). The Pb 6*s* – O 2*p* and Pb 6*s* – Cl 3*p* bonding states collectively give rise to the feature centered at 10.5 eV in the valence band HAXPES spectra. The Pb 6*s* – O 2*p* and Pb 6*s* – Cl 3*p* antibonding states are further stabilized by an overlap with empty Pb 6*p* states in the conduction band wherein this energetic stabilization drives a second-order Jahn—Teller distortion. The resulting hybrid states have considerable *s*-character, are situated at the valence band maximum, and have been represented as the shaded lone pair states in Figures 3-5a and 3-5b. Since O 2*p* states are closer in energy to Pb 6*s* states, greater mixing is expected in comparison to Cl 3*p* states, which induces a substantially greater splitting of B and AB states resulting in the Pb $6s^2$—O 2*p* states being positioned at the valence band maximum.

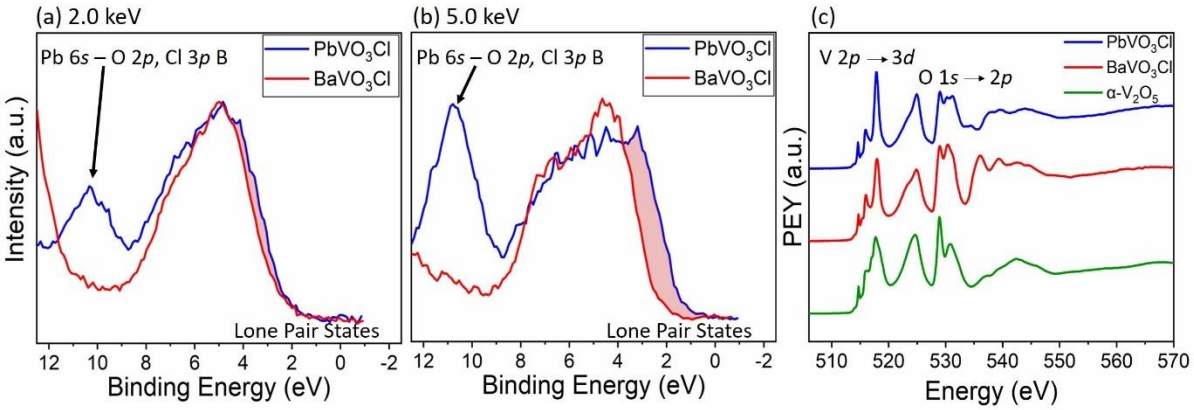

Figure 3-5: (a) HAXPES of $PbVO_3Cl$ and $BaVO_3Cl$ at an incident photon energy of 2.0 keV. (b) HAXPES of $PbVO_3Cl$ and $BaVO_3Cl$ at an incident photon energy of 5.0 keV. (c) XANES spectroscopy plots for α-V_2O_5, $BaVO_3Cl$ and $PbVO_3Cl$ at the V L-edge and O K-edge.

Electronic structure calculations were performed for both $BaVO_3Cl$ and $PbVO_3Cl$ to further understand the role of Pb $6s^2$ lone pair states in mediating the thermochromic transition. DFT is constrained in the treatment of strongly correlated systems because of band gap and localization errors, but the results nevertheless provide a guide to interpreting the origins and relative energy positioning of states observed in X-ray emission and absorption spectra. The projected density of states (PDOS) and total density of states (TDOS) for the ground state electronic structures of $BaVO_3Cl$ and $PbVO_3Cl$ are plotted in Figure 3-6. The PDOS of $BaVO_3Cl$ and $PbVO_3Cl$ indicates that in both compounds the valence band primarily comprises contributions from Cl 3*p* and O 2*p* states, whereas the conduction band is derived primarily from V 3*d* states. In addition to Cl and O *p*-states, notable contributions from Pb states, specifically Pb 6*s* and 6*p* states, can also be observed in the valence and conduction bands. The Pb 6*s* – O 2*p* and Pb 6*s* – Cl 3*p* bonding states reside deep in the valence band (as shaded in Figure 3-6b), as also observed in the HAPXES data shown in Figures 3-5a and 3-5b. No comparable contributions are discernible for

the Ba analog. The lone-pair-derived Pb 6*s* hybrid states at the top of the valence band are more pronounced in comparison to Ba 6*s* states in $BaVO_3Cl$. In other words, the DFT results corroborate the assignment of the HAXPES features at the valence band as arising from states with considerable Pb $6s^2$ character. Notable Pb 6*s*—O 2*p* hybrid states are further observed at the conduction band edge that are substantially more pronounced than for $BaVO_3Cl$ and have been further probed through XANES measurements.

The peak positions, relative intensities of spectral features, and line shapes of XANES spectra provide insight into atom-projected density of states (modified by self-energy effects), thereby serving as an excellent element-specific probe of electronic structure above the Fermi level.[35] XANES measurements were performed at the V L-edge ($2p \rightarrow 3d$) and O K ($1s \rightarrow 2p$)-edge to map the conduction band of $BaVO_3Cl$ and $PbVO_3Cl$. XANES data for $BaVO_3Cl$ and $PbVO_3Cl$ are plotted in Figure 3-5c and compared with α-V_2O_5 where reliable assignments of the spectral features are available from excited state time-dependent DFT calculations.[36] The V L_{III}-edge is characterized by sharp features corresponding to transitions from V 2*p* core states to V 3*d* states split by crystal field splitting in the square pyramidal coordination geometry.[37-38] The V L_{II}-edge cannot be interpreted solely in terms of electronic structure as a result of spectral broadening derived from Coster—Kronig Auger decay processes. The O K-edge comprises transitions from O 1*s* core states to O 2*p* states hybridized with V 3*d* states that are split by crystal-field splitting. The fine structure represents the transitions to π and σ-bonded hybrid states.[39]In accordance with our calculated PDOS for V in Figures 3-S1a and 3-S1b, the V L-edge XANES plots for $BaVO_3Cl$ and $PbVO_3Cl$ exhibit similar spectral features. Despite the similar VO_5 square pyramids observed in both $PbVO_3Cl$ and $BaVO_3Cl$, several finely structured features are observed in O K-edge spectra for the former that are not observed for the latter. Based on the DFT calculations, Pb 6*s* and 6*p*

hybridization with O 2*p* states is expected (Figure 3-6d) and indeed these lone-pair hybridized states are clearly discernible in O K-edge spectra.

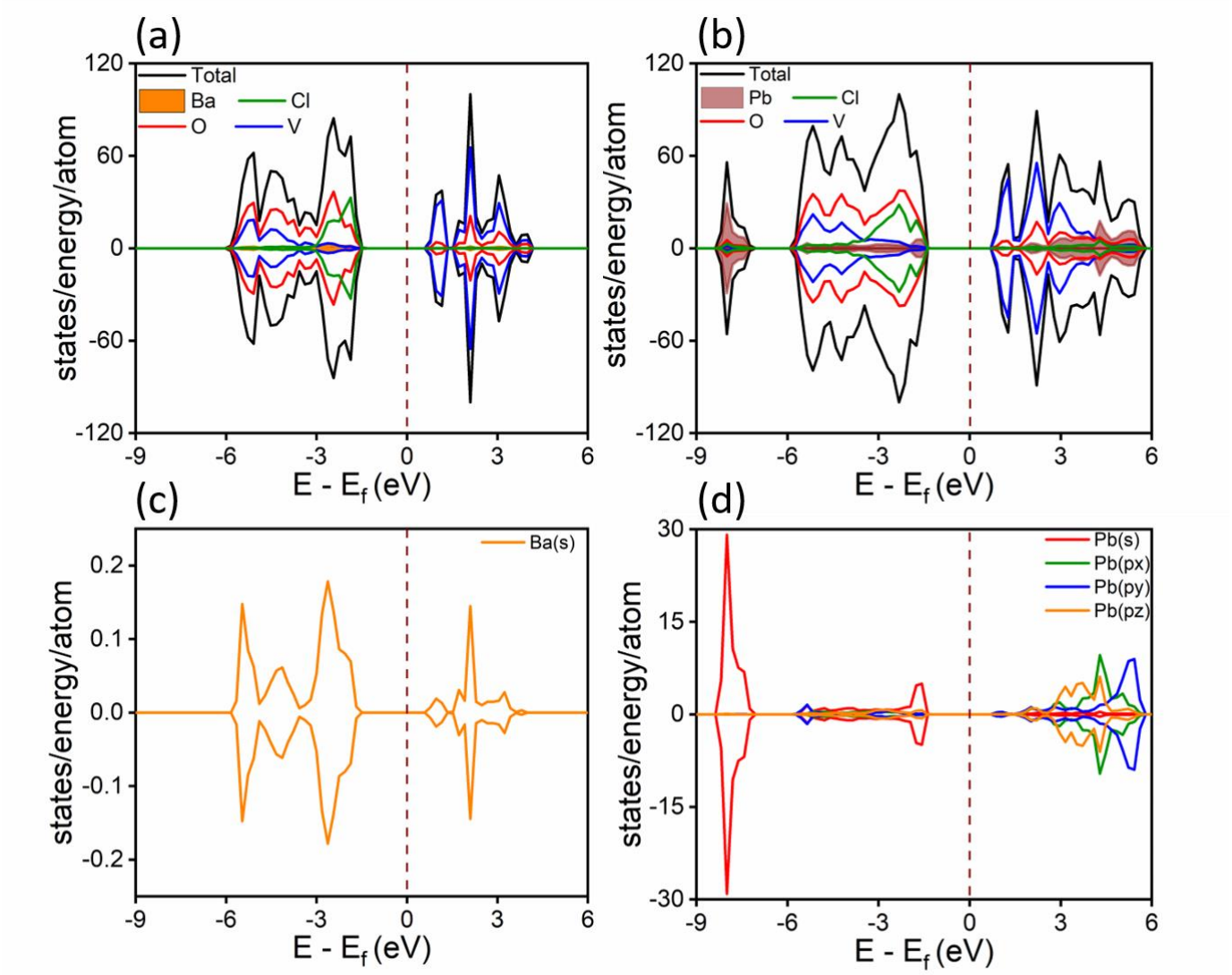

Figure 3-6: (a) GGA+U calculated ground state total density of states (TDOS) for $BaVO_3Cl$. (b) TDOS for $PbVO_3Cl$, Pb states are shaded in brown. (c) Calculated PDOS of Ba 6s in $BaVO_3Cl$. (d) PDOS of Pb 6s and 6p showing the presence of lone pair states at the VBM.

Lone pair states and concomitant structural distortions have been previously observed for lead oxides and chalcogenides as a result of the hybridization of unoccupied Pb 6*p* states with the

antibonding states originating from the interaction of Pb 6*s* states with anion *p* states (Figure 3-7).[10,18] However, in mixed-anion $PbVO_3Cl$, in addition to the Pb-O hybridization, the stereoactive lone pair states are also amenable to mixing with Cl states. Based on photoemission measurements, the Cl 3*p* (~6 eV) atomic states are higher in the valence band as compared to O 2*p* (~ 9eV) atomic states. The closer proximity of Pb 6*s* states with O 2*p* states facilitates improved hybridization and substantial *s*-character in hybrid B and AB states, which in turns promotes hybridization with Pb 6*p* states as sketched in Figure 3-7. Electronic structure calculations indicate that filled anti-bonding Pb-O and Pb-Cl lone pair states are present at the valence band maximum (Figure 3-6b).

3.4. Conclusion

The change in color from yellow to red observed for $PbVO_3Cl$ above 200°C has no parallels in the alkaline-earth or rare-earth counterparts and suggests a thermally driven diminution of the bandgap. To understand the role of Pb $6s^2$ lone pairs in inducing a thermochromic transition in $PbVO_3Cl$, the coupling between geometric and electronic structure needs to be understood. The XPDF and NPDF analyses show that warming the $PbVO_3Cl$ sample leads to an off-center Pb atom, likely because of lone-pair repulsions. The lattice anharmonicity arising from the Pb displacement brings the Pb and O atoms closer, whereas the Pb—Cl distances remain essentially unchanged. The stronger Pb—O interactions suggest improved mixing of Pb $6s^2$ and O 2*p* states, resulting in greater splitting of the B and AB states sketched in Figure 3-7. As a result, the occupied AB state will be positioned higher in energy, decreasing the effective bandgap of the system. A distinctive feature of V—O bonds in oxides is their highly tunable covalency/ionicity, which is manifested in the vast available array of binary vanadium oxide polymorphs.[40] The decreased bond length and increased hybridization of Pb—O states is furthermore compensated by an increase in V—O bond lengths and expansion of the VO_5 square pyramids, which is directly observed in the NPDF

measurements. In other words, the lattice anharmonicity invoked by the anisotropic movement of Pb atoms because of lone pair repulsions strengthens Pb—O interactions and weakens V—O interactions. The diminished V 3*d*—O 2*p* hybridization furthermore reduces the splitting of the O 2*p*-derived valence band and the V 3*d*-derived conduction band. As sketched in Figure 3-7, the effective bandgap shrinks because of the shifting of Pb $6s^2$—O 2*p* hybrid anti-bonding states to higher energies and the accompanying shift of the V 3*d*—O 2*p* hybridized conduction band edge to lower energies. XPDF data support this hypothesis; density of states plots calculated from structural models derived from the refined XPDF data for $PbVO_3Cl$ at 300 K and 570 K are shown in Figure 3-S6 and furthermore support the notion of the reduction of the band gap as a result of the shift of Pb $6s^2$—O 2*p* hybrid states in the valence band to higher energy (as a result of stronger Pb—O hybridization) and the concomitant shift of V 3*d*—O2*p* states in the conduction band to lower energy (as a result of expansion of the VO_5 square pyramids) as a result of the structural distortions induced with increasing temperature. The lone-pair driven structural distortions resulting in hybridization between a lone pair and O 2*p* and the covalency between the transition metal and O 2*p* are reminiscent of $BiMnO_3$.[41-42] The strongly correlated changes in lattice and electronic structure thus synergistically drive a decrease of the effective bandgap of $PbVO_3Cl$ resulting in a thermochromic transition from yellow to red at 200 ^oC. Future work will focus on single-crystal diffraction and *ab initio* molecular dynamics modeling to examine the evolution of atomistic and electronic structure with temperature.

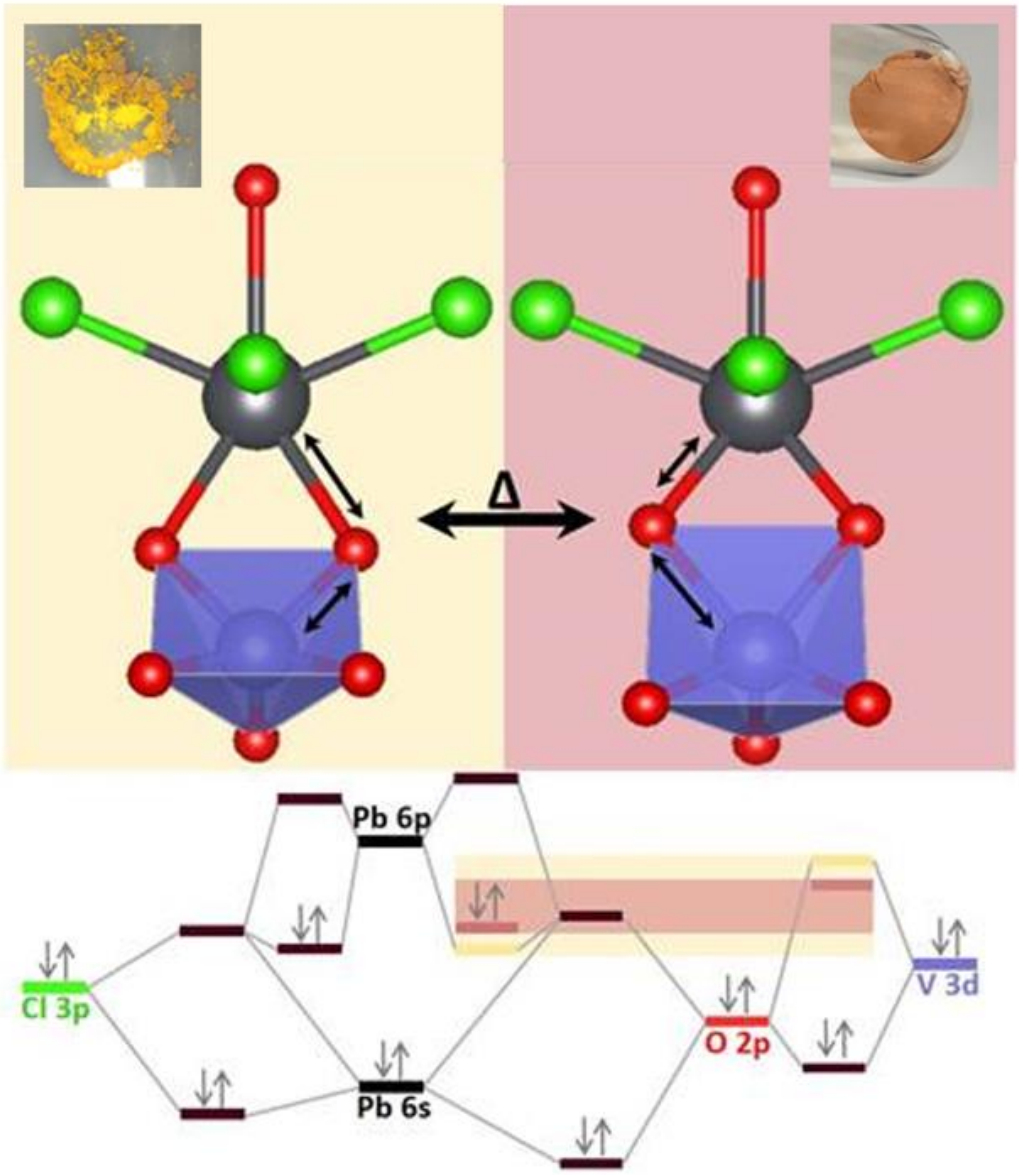

Figure 3-7: Pictorial representation of changes in the local geometric structure of Pb upon warming and its effects on the bandgap which enables the thermochromic transition in $PbVO_3Cl$. The Pb-O lone pair states constitute the HOMO (valence band maximum), whereas the empty V 3d – O 2p molecular states represent the LUMO (conduction band minimum.) The bandgap before and after the thermochromic transition is highlighted.

3.5. Acknowledgements

RM and UD acknowledge support from UTA Startup funds, and UD acknowledges Sigma Xi Grant-in-Aid #G20191001100810061 for support. WZ and SB acknowledge support from the National Science Foundation under DMR 1627197. DFT simulations were performed as part of a User Project at The Molecular Foundry (TMF), Lawrence Berkeley National Laboratory. TMF is supported by the Office of Science, Office of Basic Energy Sciences, of the U.S. Department of Energy, under Contract No. DE-AC02- 05CH11231. Portions of this research were conducted with the advanced computing resources provided by Texas A&M High Performance Research Computing. This research used resources of the National Synchrotron Light Source II, a U.S. Department of Energy (DOE) Office of Science User Facility operated for the DOE Office of Science by Brookhaven National Laboratory under Contract No. DE-SC0012704. WZ acknowledges support from the Advanced Light Source (ALS) doctoral fellowship in residence. Acknowledgment is made to Bates College Startup funds (WZ, AK,and GL) for support of this research. GL would like to thank Hayden A. Evans for helpful discussions. A portion of this research used resources at the Spallation Neutron Source, a DOE Office of Science User Facility operated by the Oak Ridge National Laboratory. Use of the Advanced Photon Source at Argonne National Laboratory was supported by the U. S. Department of Energy, Office of Science, Office of Basic Energy Sciences, under Contract No. DE-AC02-06CH11357.

Supporting Information. XRD results, X-ray fluorescence data, Partial neutron (NPDF) and X-ray pair distribution function (XPDF); Fits of temperature-dependent NPDF and XPDF data; Partial DOS; DOS for temperature-dependent $PbVO_3Cl$.

3.6. References

1. Jansen, M.; Letschert, H. P., Inorganic yellow-red pigments without toxic metals. *Nature* **2000,** *404*, 980-982.
2. Cho, J. S., A.; Suwandaratne, N.; Wangoh, L.; Andrews, J. L.; Zhang, P.; Piper, L. F. J.; Watson, D. F.; Banerjee, S. , The Middle Road Less Taken: Electronic-Structure-Inspired Design of Hybrid Photocatalytic Platforms for Solar Fuel Generation. *Acc. Chem. Res.* **2019,** *52*, 645-655.
3. Suzuki, H.; Kunioku, H.; Higashi, M.; Tomita, O.; Kato, D.; Kageyama, H.; Abe, R., Lead Bismuth Oxyhalides PbBiO2X (X = Cl, Br) as Visible-Light-Responsive Photocatalysts for Water Oxidation: Role of Lone-Pair Electrons in Valence Band Engineering. *Chemistry of Materials* **2018,** *30*, 5862-5869.
4. Kageyama, H.; Hayashi, K.; Maeda, K.; Attfield, J. P.; Hiroi, Z.; Rondinelli, J. M.; Poeppelmeier, K. R., Expanding Frontiers in Materials Chemistry and Physics with Multiple Anions. *Nat. Comm.* **2018,** *9*, 772.
5. Huang, X.; Zeng, Z.; Zhang, H., Metal Dichalcogenide Nanosheets: Preparation, Properties and Applications. *Chem. Soc. Rev.* **2013,** *42*, 1934-1946.
6. Cheng, W.-D.; Lin, C.-S.; Luo, Z.-Z.; Zhang, H., Designing the Syntheses and Photophysical Simulations of Noncentrosymmetric Compounds. *Inorg. Chem. Front.* **2015,** *2*, 95-107.
7. Li, Y.-Y.; Wang, W.-J.; Wang, H.; Lin, H.; Wu, L.-M., Mixed-Anion Inorganic Compounds: A Favorable Candidate for Infrared Nonlinear Optical Materials. *Cryst. Growth Des.* **2019,** *19*, 4172-4192.
8. Yang, Z.; Hu, C.; Mutailipu, M.; Sun, Y.; Wu, K.; Zhang, M.; Pan, S., Oxyhalides: Prospecting Ore for Optical Functional Materials with Large Laser Damage Thresholds. *J. Mat. Chem. C* **2018,** *6*, 2435-2442.
9. Gągor, A.; Banach, G.; Węcławik, M.; Piecha-Bisiorek, A.; Jakubas, R., The Lone-Pair-Electron-Driven Phase Transition and Order–Disorder Processes in Thermochromic (2-MIm)SbI_4 Organic–Inorganic Hybrid. *Dalt. Trans.* **2017,** *46*, 16605-16614.
10. Walsh, A.; Payne, D. J.; Egdell, R. G.; Watson, G. W., Stereochemistry of Post-Transition Metal Oxides: Revision of the Classical Lone Pair Model. *Chem. Soc. Rev.* **2011,** *40*, 4455-4463.
11. Waghmare, U. V.; Spaldin, N. A.; Kandpal, H. C.; Seshadri, R., First-Principles Indicators of Metallicity and Cation Off-Centricity in the IV-VI Rocksalt Chalcogenides of Divalent Ge, Sn, and Pb. *Phys. Rev. B* **2003,** *67*, 125111.
12. Fabini, D. H.; Laurita, G.; Bechtel, J. S.; Stoumpos, C. C.; Evans, H. A.; Kontos, A. G.; Raptis, Y. S.; Falaras, P.; Van der Ven, A.; Kanatzidis, M. G.; Seshadri, R., Dynamic Stereochemical Activity of the Sn^{2+} Lone Pair in Perovskite $CsSnBr_3$. *J. Am. Chem. Soc.* **2016,** *138*, 11820-11832.
13. Hu, Y. Z.; Zhang, H. B.; Chong, W. K.; Li, Y. X.; Ke, Y. J.; Ganguly, R.; Morris, S. A.; You, L.; Yu, T.; Sum, T. C.; Long, Y.; Fan, H. J., Molecular Engineering Toward Coexistence of Dielectric and Optical Switch Behavior in Hybrid Perovskite Phase Transition Material. *J. Phys. Chem. A* **2018,** *122*, 6416-6423.
14. Jensen, K. M. Ø.; Božin, E. S.; Malliakas, C. D.; Stone, M. B.; Lumsden, M. D.; Kanatzidis, M. G.; Shapiro, S. M.; Billinge, S. J. L., Lattice Dynamics Reveals a Local Symmetry Breaking in the Emergent Dipole Phase of PbTe. *Phys. Rev. B* **2012,** *86*, 085313.

15. Walsh, A.; Watson, G. W., The Origin of the Stereochemically Active Pb(II) Lone Pair: DFT Calculations on PbO and PbS. *J. Solid State Chem.* **2005,** *178*, 1422-1428.
16. Andrews, J. L. C., J.; Wangoh, L.; Suwandaratne, N.; Sheng, A.; Chauhan, S.; Nieto, K.; Mohr, A.; Kadassery, K. J.; Popeil, M. R.; Thakur, P. K.; Sfeir, M.; Lacy, D. C.; Lee, T.-L.; Zhang, P.; Watson, D. F.; Piper, L. F. J.; Banerjee, S. , Hole Extraction by Design in Photocatalytic Architectures Interfacing CdSe Quantum Dots with Topochemically Stabilized Tin Vanadium Oxide. *J. Am. Chem. Soc.* **2018,** *140*, 17163–17174.
17. Razek, S. A. P., M. R.; Wangoh, L.; Rana, J.; Suwandaratne, N.; Andrews, J. L.; Watson, D. F.; Banerjee, S.; Piper, L. F. J., Designing Catalysts for Water Splitting Based on Electronic Structure Considerations. *Electronic Structure* **2020,** *2*, 1-26.
18. Jo, V.; Kim, M. K.; Shim, I. W.; Ok, K. M., Synthesis, Structure, and Characterization of a Layered Mixed Metal oxychloride, $PbVO_3Cl$. *Bull. Korean Chem. Soc.* **2009,** *30*, 2145-2148.
19. Borel, M. M. C., J.; Leclaire, A.; Raveau, B., Chlorovanadates with original chain and layered structures: AVO_3Cl (A = Ba, Sr, Cd). *J. Solid State Chem.* **1999,** *145*, 634-638.
20. Neuefeind, J.; Feygenson, M.; Carruth, J.; Hoffmann, R.; Chipley, K. K., The Nanoscale Ordered MAterials Diffractometer NOMAD at the Spallation Neutron Source SNS. *Nucl. Instrum. Methods Phys. Res., B* **2012,** *287*, 68-75.
21. Qiu, X.; Thompson, J. W.; Billinge, S. J. L., PDFgetX2: a GUI-driven program to obtain the pair distribution function from X-ray powder diffraction data. *Journal of Applied Crystallography* **2004,** *37*, 678.
22. Farrow, C. L.; Juhas, P.; Liu, J. W.; Bryndin, D.; Božin, E. S.; Bloch, J.; Proffen, T.; Billinge, S. J. L., PDFfit2 and PDFgui: Computer Programs for Studying Nanostructure in Crystals. *J. Phys.: Cond. Matt.* **2007,** *19*, 335219.
23. Momma, K.; Izumi, F., VESTA 3 for three-dimensional visualization of crystal, volumetric and morphology data. *J. Appl. Crystallogr.* **2011,** *44*, 1272-1276.
24. Joubert, D., From Ultrasoft Pseudopotentials to the Projector Augmented-Wave Method. *Phys. Rev. B: Condens. Matter Mater. Phys.* **1999,** *59*, 1758-1775.
25. Kresse, G.; Furthmüller, J., Efficient Iterative Schemes for Ab Initio Total-Energy Calculations Using a Plane-Wave Basis *Phys. Rev. B: Condens. Matter Mater. Phys.* **1996,** *54*, 11169–11186.
26. Kresse, G.; Hafner, J., Ab initio molecular dynamics for open-shell transition metals. *Phys. Rev. B* **1993,** *48*, 13115-13118.
27. Perdew, J. P.; Burke, K.; Ernzerhof, M., Generalized gradient approximation made simple. *Phys. Rev. Lett.* **1996,** *77*, 3865-3868.
28. Jain, A. H., G.; Moore, C. J.; Ping Ong, S.; Fischer, C. C.; Mueller, T.; Persson, K. A.; Ceder, G. , A High-Throughput Infrastructure for Density Functional Theory Calculations. *Comput. Mater. Sci.* **2011,** *50*, 2295-2310.
29. Shannon, R. D. P., C. T., Effective Ionic Radii in Oxides and Fluorides. *Acta Cryst.* **1969,** *B25*, 925.
30. Wangoh, L. M., P. M.; Quackenbush, N. F.; Sallis, S., Fischer, D. A.; Woicik, J. C.; Banerjee, S.; Piper, S. L. J., Electron Lone Pair Distortion Facilitated Metal-Insulator Transition in β-$Pb_{0.33}V_2O_5$ Nanowire. *Appl. Phys. Lett.* **2014,** *104*, 182101-182108.

31. Trzhaskovskaya, M. B.; Nefedov, V. I.; Yarzhemsky, V. G., Photoelectron Angular Distribution Parameters for Elements Z = 55 to Z = 100 in the Photoelectron Energy Range 100-5000 eV. *At. Data Nucl. Data Tables* **2002,** *82*, 257-311.
32. Yeh, J. J.; Lindau, I., Atomic Subshell Photoionization Cross Sections and Asymmetry Parameters: $1 \leqslant Z \leqslant 103$. *At. Data Nucl. Data Tables* **1985,** *32*, 1-155.
33. Weiland, C.; Rumaiz, A. K.; Pianetta, P.; Woicik, J. C., Recent Applications of Hard X-ray Photoelectron Spectroscopy. *J. . Vac. Sci. Technol. A* **2016,** *34*, 030801.
34. Weinen, J.; Koethe, T. C.; Chang, C. F.; Agrestini, S.; Kasinathan, D.; Liao, Y. F.; Fujiwara, H.; Schüßler-Langeheine, C.; Strigari, F.; Haupricht, T.; Panaccione, G.; Offi, F.; Monaco, G.; Huotari, S.; Tsuei, K. D.; Tjeng, L. H., Polarization Dependent Hard X-ray Photoemission Experiments for Solids: Efficiency and Limits for Unraveling the Orbital Character of the Valence Band. *J. Electron Spectrosc.* **2015,** *198*, 6-11.
35. Chen, J. G., NEXAFS Investigations of Transition Metal Oxides, Nitrides, Carbides, Sulfides and Other Interstitial Compounds. *Surf. Sci. Rep.* **1997,** *30*, 1-152.
36. De Jesus, L. R. H., G. A.; Liang, Y.; Parija, A.; Jaye, C.; Wangoh, L.; Wang, J.; Fischer, D. A.; Piper, L. F. J.; Prendergast, D.; Banerjee, S. , Mapping Polaronic States and Lithiation Gradients in Individual V_2O_5 Nanowires. *Nature Commun.* **2016,** *7*, 12021-12029.
37. Velazquez, J. M. J., C.; Fischer, D. A.; Banerjee, S., Near Edge X-ray Absorption Fine Structure Spectroscopy Studies of Single-Crystalline V_2O_5 Nanowire Arrays. *J. Phys. Chem. C 113*, 7639-7645.
38. Maganas, D. R., M.; Hävecker, M.; Trunschke, A.; Knop-Gericke, A.; Schlögl, R.; Neese, F., First Principles Calculations of the Structure and V L-Edge X-ray Absorption Spectra of V_2O_5 Using Local Pair Natural Orbital Coupled Cluster Theory and Spin–Orbit Coupled Configuration Interaction Approaches. *Phys. Chem. Chem. Phys.* **2013,** *15*, 7260-7276.
39. Goering, E.; Müller, O.; Klemm, M.; denBoer, M. L.; Horn, S., Angle Dependent Soft-X-ray Absorption Spectroscopy of V_2O_5. *Phil. Mag. B* **1997,** *75*, 229-236.
40. Parija, A. W., G. R.; Andrews, J. L.; Banerjee, S., Traversing Energy Landscapes Away From Equilibrium: Strategies for Accessing and Utilizing Metastable Phase Space. *J. Phys. Chem. C* **2018,** *122*, 25709-25728.
41. Baettig, P.; Seshadri, R.; Spaldin, N. A., Anti-polarity in Ideal $BiMnO_3$. *J. Am. Chem. Soc.* **2007,** *129*, 9854-9855.
42. Seshadri, R.; Hill, N. A., Visualizing the Role of Bi 6s "Lone Pairs" in the Off-Center Distortion in Ferromagnetic $BiMnO_3$. *Chem. Mater.* **2001,** *13*, 2892-2899.

Chapter 4 Vacancy-Driven Disorder and Elevated Dielectric Response in the Pyrochlore $Pb_{1.5}Nb_2O_{6.5}$

Reprinted with permission from U. Dang, J. O'Hara, H. A. Evans, D. Olds, J. Chamorro, D. Hickox-Young, G. Laurita, and R. T. Macaluso. Vacancy-Driven Disorder and Elevated Dielectric Response in the Pyrochlore $Pb_{1.5}Nb_2O_{6.5}$. *Inorg. Chem.* **2022,** *61*, 46, 18601-18610.

Abstract

Lone pair driven distortions are a hallmark of many technologically important lead (Pb)-based materials. The role of Pb^{2+} in polar perovskites is well understood and easily manipulated for applications in piezo- and ferroelectricity, but the control ordered lone pair behavior in Pb-based pyrochlores is less clear. Crystallographically and geometrically more complex than the perovskite structure, the pyrochlore structure is prone to geometric frustration of local dipoles due to a triangular arrangement of cations on a diamond lattice. The role of vacancies on the O' site of the pyrochlore network has been implicated as an important driver for the expression and correlation of stereochemically active lone pairs in pyrochlores such as $Pb_2Ru_2O_{6.5}$ and $Pb_2Sn_2O_6$. In this work we report on the structural, dielectric, and heat capacity behavior of the cation- and anion-deficient pyrochlore $Pb_{1.5}Nb_2O_{6.5}$ upon cooling. We find that local distortions are present at all temperatures that can be described by cristobalite-type cation ordering, and this ordering persists to longer length scales upon cooling. From a crystallographic perspective, the material remains disordered and does not undergo an observable phase transition. In combination with density function calculations, we propose that the stereochemical activity of the Pb^{2+} lone pairs is driven by proximity to O' vacancies, and the crystallographic site disorder of the O' vacancies prohibits long range correlation of lone pair driven distortions. This in turn prevents a low temperature phase transition and results in an elevated dielectric permittivity across a broad temperature range.

4.1. Introduction

Pyrochlores have been extensively studied for a variety of technologically important properties, including high electrical conductivity,[1,2] ferroelectricity,[3] photocatalysis,[4,5] frustrated magnetism,[6–8] ordered magnetism,[9] photoluminescence,[10] and ionic conductivity.[11–14] Some pyrochlores, such as $(Bi_{1.5}Zn_{0.5})(Nb_{1.5}Zn_{0.5})O_7$ (BZN),[15] $Bi_2Ti_2O_7$,[16–19] and mixed-anion $Pb_2Ti_2O_{5.4}F_{1.2}$[20] have attracted considerable attention as high-κ materials where the large dielectric constants are closely tied to short-range displacements of the metal cations. Of particular recent interest are pyrochlores where dipole moments are geometrically frustrated within a topological lattice leading to spin (magnetic dipoles)[21] and charge (electric dipoles)[15] ice behavior.

The ideal pyrochlore with the chemical formula $A_2B_2O_7$ (often written $A_2B_2O_6O'$) is described with the cubic $Fd\bar{3}m$ space group.[22] The *A* cations (typically a +2 or +3 cation) and *B* cations (typically a +5 or +4 cation, respectively) are located on separate but interpenetrating A_2O' and B_2O_6 frameworks, illustrated in Figure 4-1a. The A_2O' framework consists of corner-linked $A_{4/2}O'$ tetrahedra, and the B_2O_6 framework consists of BO_6 octahedra. These octahedra are corner-linked, forming a six-membered ring (Figure 4-1b) where the *A*-site cations are ideally positioned at the 16*d* site at the center of the BO_6 ring and linearly coordinated to the O' anions perpendicular to the ring. This ring structure creates a channel within the overall structure, and the size of this structure allows for flexibility of atom positions; for example, the *A* cation can shift towards the ring into the 96*g* site,[17,19,23–26] and the O' can shift above and below the ring plane to the 32*e* site.[17,22] The rigid channel structure additionally allows for compositional flexibility in the form of vacancies on both the *A* and O' sites.[22]

The arrangement of dipoles (magnetic or electrical) on the pyrochlore lattice has drawn considerable attention in the solid state and condensed matter communities. Akin to the triangular arrangement of points on kagomé lattice, the cations in the pyrochlore structure comprise corner-

sharing tetrahedra with each cation on the vertices of the tetrahedra. This three-dimensional triangular arrangement leads to frustration of dipoles, as there are a number of degenerate low energy spin arrangements. This has been detailed for magnetic dipoles in the formation of spin ices[21] and the more recent proposal of the existence of magnetic monopoles,[27] and this effect can be observed with electric dipoles in the analogous charge-ice.[15] Electrical dipoles are often driven by cations with electron shell configurations that contribute to off-centering within their bonding environment, particularly those with ns^2 stereochemically active lone pairs[28] or nd^0 second-order Jahn-teller (SOJT) active cations.[29] The displacement of these dipoles can be enhanced through cooperative distortions of lone pair and SOJT cations, such as in the prototypical perovskite $PbTiO_3$.[30]

While most pyrochlores display frustration of dipoles that prevents long-range ordering, a few compositions overcome this geometric constraint and exhibit polar low energy crystal structures.[3,31–36] The most prominent of these is the highly-studied ferroelectric $Cd_2Nb_2O_7$.[3,37,38] The material undergoes a phase transition at approximately 204 K followed by a series of phase transitions around 196 K.[39] There are two further phase transitions reported at approximately 85 K to an uncharacterized monoclinic phase, and the fourth at approximately 45 K to another unique monoclinic phase.[40–42] There is a vast amount of sometimes-conflicting literature surrounding the nature of the intermediate phases above 196 K,[40–49] while the ferroelectric phase below this temperature is reported as orthorhombic *Ima*2.[41,50] As a testament to the complexity of the interpenetrating pyrochlore networks, this structural behavior can be altered by substitution on either network (including anion substitution on the 8*b* Wyckoff site), and this is proposed to be due to changes in covalency of the overall system.[50] The existence of a polar phase in $Cd_2Nb_2O_7$ and the ability to alter structural behavior points to the need to further investigate the pyrochlore structure through related chemistries.

The combination of lone pair cations and vacancies in pyrochlores significantly impacts their structure and physical behavior. In $Bi_2Ti_2O_7$, there are no vacancies on the O' site, and the material exhibits frustration and charge ice behavior at low temperatures.[15] In $Pb_2Sn_2O_6$, vacancies due to the complete absence of O' anions result in topological frustration of the lone pair, where the lone pair cannot localize into a single lobe of electron density and instead splits into two lobes in adjacent vacancy sites for every fourth Pb atom in the structure.[15] These lone pair distortions remain frustrated and no coherent long-range ordering is achieved. In the 'ordered-ice' $Pb_2Ru_2O_6O'_{0.5}$, ordered vacancies of the O' sites direct $6s^2$ lone pairs towards the O', relieving geometric frustration.[51] This is reflected in heat capacity measurements, where the lattice-only contribution is significantly lower upon cooling in the ordered $Pb_2Ru_2O_6O'_{0.5}$ vs. the completely disordered $Bi_2Ti_2O_7$. More broadly, Pb-based pyrochlores are a fascinating study on the stoichiometric constraints for forming the cubic $Fd\bar{3}m$ structure, as some only have vacancies on the O' site (such as $Pb_2Sn_2O_6$ and $Pb_2Ru_2O_6O'_{0.5}$), whereas others only form the cubic structure with vacancies on both the Pb and O' sites (such as pyrochlores $Pb_{2-x}B_2O_{7-x}$ where *B*= Nb, Ta, Sb.[22,52,53])

The pyrochlore $Pb_{1.5}Nb_2O_{6.5}$ presents a unique opportunity to investigate interactions between lone pairs of electrons, cations with the potential for SOJT distortions, and vacancies on both the *A* and O' site. Herein we have performed analyses of temperature-dependent neutron and X-ray total scattering data across various length scales to follow Pb and Nb displacements. We found that the ideal cubic structure describes the pyrochlore at room temperature, but short-range cristobalite-like distortions are needed to more adequately describe the structure at low temperatures. It appears that the crystallographic disorder of the lone pair distortions is directly related to the proximity of the crystallographically disordered O' vacancies in the material. We additionally observe an *emphanisis*-like effect[54–56] of local symmetry breaking upon warming associated with *M* –O correlations, highlighting the complex behavior of lone pair expression and correlation in

$Pb_{1.5}Nb_2O_{6.5}$. This behavior plays a crucial role in the structural and dielectric response of the material upon cooling, preventing a crystallographic phase transition accompanied by elevated dielectric permittivity down to the measured temperature of 100 K.

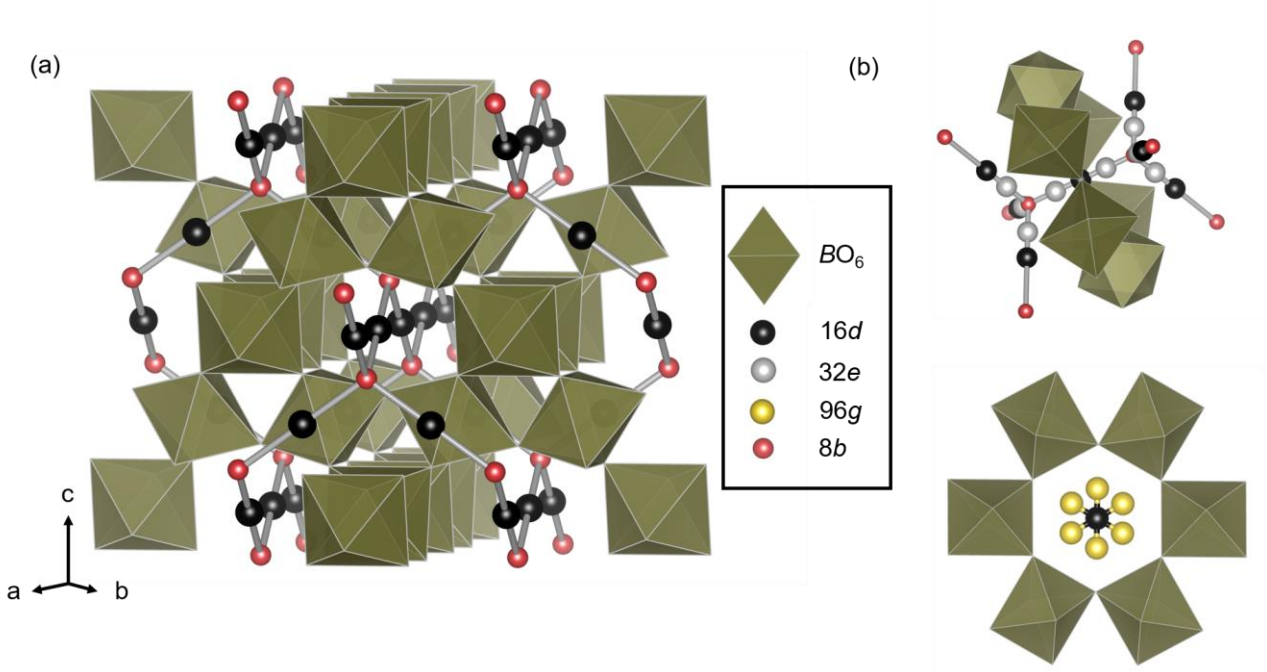

Figure 4-1: (a) The full $A_2B_2O_6O'$ pyrochlore structure illustrating the interpenetrated networks of A_2O' chains and BO_6 octahedra. (b) Highlight of the various atomic positions within the BO_6 channel; each color corresponds to a specific Wyckoff site (16d in black, 8b in pink, 96g in yellow, and 32e in grey).

4.2.Methods

4.2.1. Sample Preparation

Traditional ceramic synthesis routes were utilized to synthesize a powder sample of $Pb_{1.5}Nb_2O_{6.5}$. Stoichiometric amounts of PbO (Sigma-Aldrich, 99%) and Nb_2O_5 (Alfa Aesar, 99.9985%) were ground in a mortar and pestle and then transferred into an alumina crucible. The crucible was placed inside a fused silica ampoule, which was then sealed under vacuum and heated at a rate of 10 K/min to 1273.15 K. The samples dwelled at 1273.15 K for 10 hours, after which they were cooled to 298.15 K at 20 K/min. The powder products appeared yellow in color.

X-ray powder diffraction data was collected using a PANalytical Empyrean diffractometer to determine phase purity. The instrument was equipped with a PIXcel^{3D} detector and a Cu tube, operating at 45 kV and 40 mA, and a wavelength of 1.54 ˚Å. Data was collected between the angular range of $10^{\circ} \leq 2\theta \leq 90^{\circ}$. Step width and step rate were 0.008˚ and 0.0557 ˚/s, at room temperature, respectively. Once determined phase pure, the sample was prepared for further measurements as described below.

The sample was prepared for dielectric measurement by placing 0.5g of powder mixed with 1 mL of ethanol and placed in a ball-mill chamber. The sample was ball-milled for 9 hours. Sample chambers were removed from the ball-mill and placed in an oven at 373.15 K until the ethanol evaporated and only a dry powder sample remained. The sample was then ground with 2-3 drops of 1 % polyvinyl alcohol (PVA) in a mortar and pestle for 15 minutes, and then pressed into a pellet using a hydraulic press. The pellet was placed in a new alumina crucible and placed into a tube furnace where it was heated to 1273.15 K with a slow ramp to remove the binding agent, resulting in a pellet with 85% theoretical density based off of refined neutron values. After sintering, silver paint was applied onto one side of the pellet. The pellet was placed in an oven at 373.15 K for 10 minutes to dry the silver paint. This process was repeated for the other side of the pellet, so that there was one electrode on each side. The pellet with electrodes was dried in a box furnace at 1073.15 K for 10 minutes.

4.2.2. Neutron Diffraction

Neutron scattering data were collected on the sample at room temperature from a reactor source at the NIST Center for Neutron Research. Data were measured on the BT-1 beamline in indium cans sealed under a helium atmosphere. A Ge(733) monochromator was used with a wavelength of 1.197 Å. The data were refined using the LeBail[57] and Rietveld[58] methods in the

GSAS-II[59] software. The LeBail Method was first performed. The background was modeled with a Chebyschev function and 12 coefficients. Histogram scale factor, unit cell parameters, and sample size were also refined. Following LeBail refinements, Rietveld refinements were performed on each data set.

Neutron total scattering data were obtained utilizing the *Mantid* software framework.[60,61] The PDF was generated with a Q_{max} of 31.4 Å^{-1}. The Q_{max} value was chosen to balance between resolution and termination ripples in the reduced data for each sample. Least-squares refinement of PDF data was performed using PDFGUI.[62]

4.2.3. Synchrotron X-ray Diffraction

Synchrotron X-ray diffraction data were obtained with λ = 0.1665 Å at the National Synchrotron Light Source II at Brookhaven National Laboratory in Upton, New York. Both X-ray powder diffraction and PDF data were collected. The data were collected on cooling, with one measurement taken per 20 K. A total of 12 measurements were taken persample, at temperatures between 293 K and 73 K. X-ray PDF data were obtained using the program PDFgetX3[63] with a Qmax = 22 Å^{-1}. Least-squares refinement of PDF data was performed using PDFGUI.[62]

4.2.4. Structural visualization

Density Functional Theory (DFT) for visualization of the electron localization functions (ELFs) was performed using the Quantum Espresso software suite. [64,65] Calculations were carried out on the $P4_32_12$ cristobalite model obtained from the local fit of the neutron PDF data of $Pb_{1.5}Nb_2O_{6.5}$ at 300 K. Calculations utilized a plane wave basis set and the Perdew-Burke-Ernzerhof functional for solids (PBEsol).[66,67] Calculations were performed using a 5 × 5 × 5 Monkhorst-Pack grid for Brillouin zone sampling and Gaussian smearing for self-consistent field (SCF) calculations to achieve convergence. Electron localization functions (ELFs), with an isosurface level of 0.4 e/Å^3,

were used to visualize the presence of stereochemically active lone pairs in the partially occupied structures. All crystal structures were visualized using the VESTA software suite.[68]

4.2.5. Dielectric Characterization

Dielectric characterization was performed with in-house probes connected to a Keysight Technologies impedance analyzer. High temperature data were obtained on heating, where the sample was placed between a parallel plate capacitor and heated, such that its capacitance was measured as a function of temperature. Samples were heated up to 423.15 K; heating was performed with an Elite Thermal Systems tube furnace, with one measurement being taken per degree increased. Similarly, low temperature data were obtained on cooling. The sample, again placed between a parallel plate capacitor, was lowered into liquid nitrogen via a stepper motor connected to an Arduino. Capacitance values were measured as the sample was cooled to 173.15 K. For each sample, capacitance values were measured at five frequencies (1, 10, 100, 250, and 100 kHz) per scan. These capacitance values were converted to relative permittivity values factoring in sample density and dimensions and plotted as a function of temperature.

4.2.6. Heat Capacity

Sintered pellets of $Pb_{1.5}Nb_2O_{6.5}$ were prepared as described above. A 5.6 mg sample was used for heat capacity measurements on a Quantum Design DynaCool Physical Properties Measurement System down to T = 1.8 K. High temperature heat capacity measurements (170 – 400 K) were additionally performed on a TA Instruments DSC 2500 using the same sample.

4.3. Results

Previous reports on $Pb_{1.5}Nb_2O_{6.5}$ indicate the room-temperature structure to be cubic with $Fd\bar{3}m$ space group.[69] To verify and quantify composition, particularly oxygen content, constant wavelength neutron diffraction data were collected at room temperature at BT-1, NCNR, NIST. Neutron scattering is a useful tool to investigate relatively light elements such as oxygen within a matrix of heavy elements, e.g., Pb and Nb.

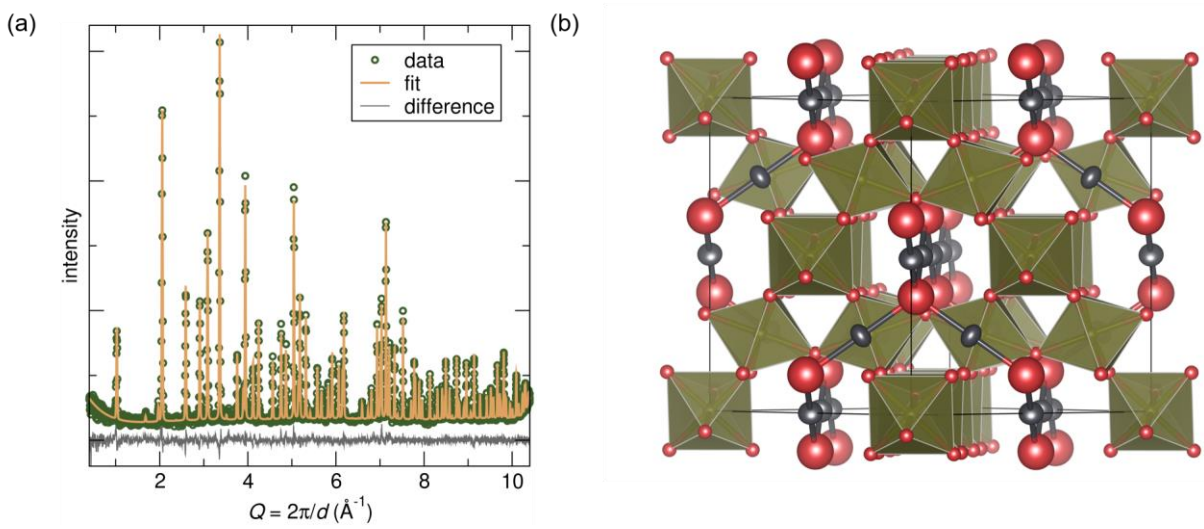

Figure 4-2: (a) Rietveld fit of neutron diffraction data (BT-1, NCNR, NIST) against the cubic $Fd\bar{3}m$ 16d model (resulting R_w = 7.3 %). (b) Refined structure with anisotropic atomic displacement parameters (shown at 90% probability) indicates disorder on the A and O' sites. Note that vacancies are not shown in this image and were assumed to be disordered on the A and O' sites for the model.

In addition to increased sensitivity to light atoms using neutron radiation, the use of the Ge(733) monochromator provides high FWHM resolution out to high Q, allowing more confidence in the refined oxygen-dependent parameters. The two best fits were achieved by modeling Pb either at the 16*d* Wyckoff position with anisotropic atomic displacement parameters (ADPs) or at the 96*g* site with isotropic ADPs (R_w = 7.33% and 7.28%, respectively), with the fit to the 16*d* model shown in Figure 4-2a. Vacancy disorder on the 8*b* site was determined for both models as fits to an

O'/vacancy- ordered $F\bar{4}3m$ model (with 4*a* site empty and 4*c* site fully occupied and vice versa) resulted in R_w = 18 %, significantly higher than an R_w of approximately 7 % for the 16*d* and 96*g* models, indicating that the vacancies are not ordered on the 8*b* site. Modeling Pb at the 16d site led to enlarged U_{xx} ADP of 0.024 Å^2, indicating displacement perpendicular to the Pb–O' bond (illustrated in Figure 4-2b) while modeling Pb at 96g led to a smaller U_{iso} value of 0.003 Å^2. For both models, Pb site occupancies were refined with Pb vacancies disordered across the site. This reduction in Pb U_{isos} with off-centering suggests the Pb atoms are statically disordered from the ideal 16*d* position perpendicular to the Pb–O' bond, as has been observed for other lone-pair bearing pyrochlores such as $Bi_2Ti_2O_7$[19] and $Bi_2Ru_2O_7$.[70] This is notably different than other Pb^{2+} pyrochlores such as $Pb_2Ru_2O_{6.5}$[51] and $Pb_2Sn_2O_6$[15] where the Pb atoms are displaced along the Pb-O'/vacancy direction. In addition to disorder on the Pb site in $Pb_{1.5}Nb_2O_{6.5}$, a large isotropic ADP of 0.061Å^2 on the O' site was found regardless of model, indicating a large amount of disorder on this site. Refined isotropic ADPs of the Nb site indicate reasonable behavior of the Nb cations, with slightly elevated ADPs (0.010 Å^2). This could indicate distortion due to SOJT-behavior but cannot be resolved with the Rietveld crystallographic model.

The pyrochlore structure is prone to both short-range atomic displacements and long- range correlated distortions depending on the chemistry of the composition and the nature of the distortions. Figure 4-3 compares two models of correlated distortions that have been observed in the literature. In the cubic $Fd\bar{3}m$ structure, the cations are found on the vertices of regular tetrahedra, displayed for the *A*-site sub-network in Figure 4-3a. The *A*-site atoms can displace in a 2-in-2-out fashion, resulting in an ordered $P43m$ model,[71,72] illustrated in Figure 4-3b. Alternatively, their local displacements can be characterized with a beta-cristobalite model[17,73,74] in which the tetrahedral sub-units can rotate about the corner-shared vertices (depicted in Figures 4-3c and 4-d). The cristobalite-like displacements can be described with either the $P4_32_12$ (#96) or $P4_12_12$ (#92) space

groups, which are structural enantiomers and result in equivalent models for powder experiments. In the cristobalite model (either space group #96 or #92), the OPb_4 tetrahedral rotations break the planar symmetry of the ideal ring of OPb_4 tetrahedra in the $Fd\bar{3}m$ model. These established structural displacements, along with our observations of enlarged ADPs on the Pb and O' site, led us to perform variable temperature neutron total scattering experiments at NOMAD to further investigate the nature of the disorder across various length scales in $Pb_{1.5}Nb_2O_{6.5}$.

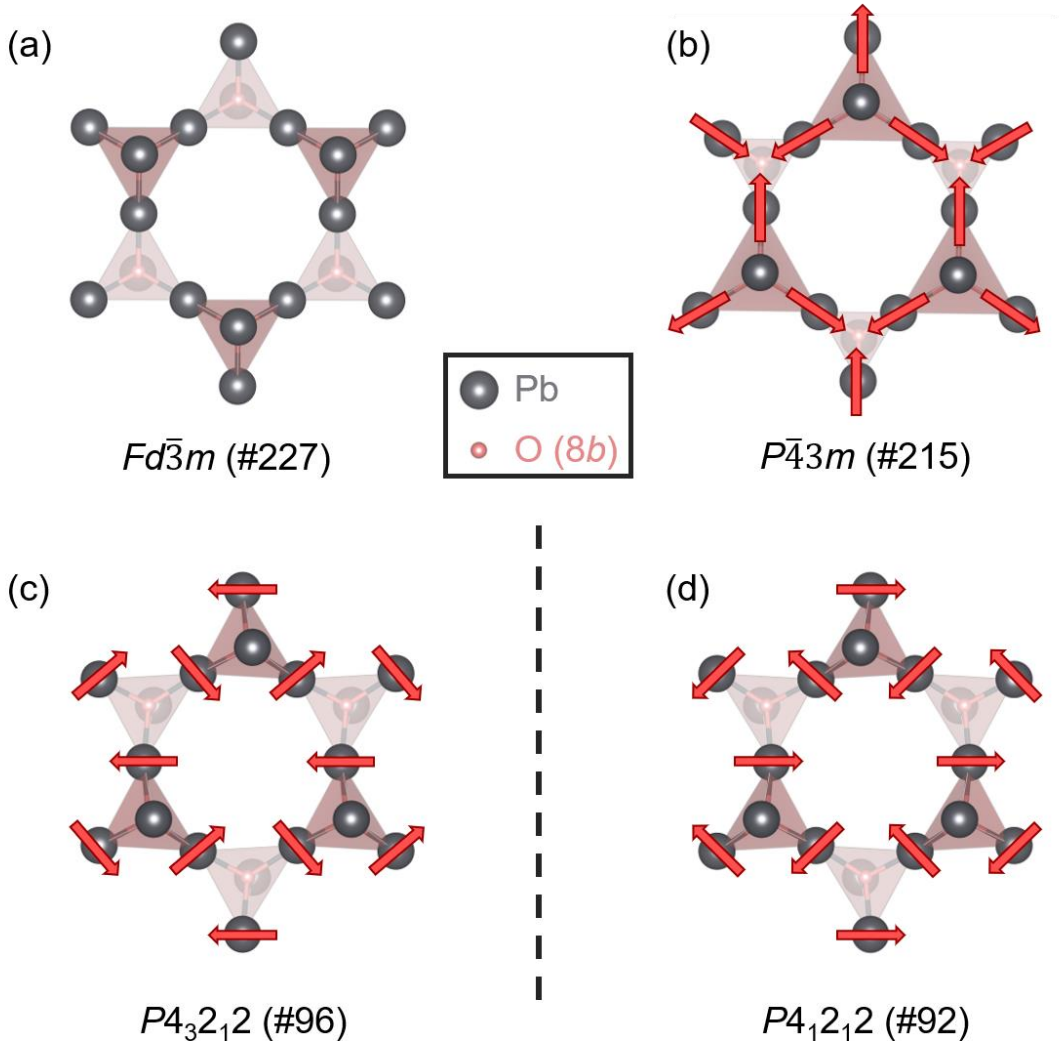

Figure 4-3: Illustration of Pb-distortions in the local models used for analysis of PDF data: (a) the cubic Fd$\bar{3}$m with no OPb_4 distortions, (b) cubic P$\bar{4}$3m model with "two in two out" distortions of Pb, (c) and (d) cristobalite-type distortions, shown here as the two enantiomorphic space groups with rotations of the OPb_4 tetrahedra.

Rietveld analyses of variable temperature neutron powder diffraction data (NOMAD, SNS, ORNL) indicate that an $Fd\bar{3}m$ model (either 16*d* or 96*g* variations) accurately describes the average structure at room temperature down to 100 K, with R_w values less than 10 % for all temperatures (fits shown in Supporting Information Figure 4-S1). The refinements indicate an increase in R_w with cooling, accompanied by elevated ADPs for Pb and O' at all temperatures. The Nb U_{iso} values decrease slightly upon cooling. This suggests the off-centering is static, and disorder on Pb and O' sites persist at all measured temperatures. A summary of the Rietveld refinements can be found in the Supporting Information Table 4-S1. To investigate the nature of the disorder on the Pb and O' site, joint analysis of the neutron (NOMAD, SNS, ORNL) and X-ray (PDF, NSLS-II, BNL) pair distribution function (PDF) was performed at 300, 200, and 100 K. The data was fit against various structural models over different real-space ranges in order to determine the best structural descriptor of the data over a given length scale. For example, the local structure is fit from 1.6–6 Å, which captures the coordination environments of the Nb and Pb cations, as well as intraoctahedral interactions such as Nb-Nb and O-O. The partial contributions to the PDF can be found in the supporting information, Figure 4-S2. Structural candidates were comparedand evaluated by the goodness-of-fit metric R_w and by observations of the fits of specific peaks in the data informed by the partial PDFs.

The data was initially fit against the two $Fd\bar{3}m$ models, and the fits to the datafor the 16*d* and 96*g* models can be seen in the supporting information Figures 4-S3 and 4-S4, respectively. The data is well-described by the models over the long-range (r > 6 Å), but it can be observed that the peaks are not completely described in the local range (r <6 Å) , indicated by dashed lines in the fits. This suggests that the local arrangements of atoms is lower in symmetry than $Fd\bar{3}m$, and prompts investigation using the distorted $P\bar{4}3m$ and cristobalite models.

The R_w values of the fits against the four candidate models - $Fd\bar{3}m$ (Pb in 16*d*), $Fd\bar{3}m$ (Pb

in 96*g*), $P\bar{4}3m$, and $P4_32_12/P4_12_12$ cristobalite - across different real-space distances (upper bound of fit indicated by r_{max}) are shown in Figure 4-4. At all temperatures, the local structure (fits up to 6 Å) is best described by the cristobalite model. At 300 K, this distortion is only observed locally, as either cubic $Fd\bar{3}m$ structure is the best description of the data at and greater than r_{max} of 12 Å. Upon cooling, the cristobalite structure appears to equally or better describe the data out to longer length scales (r_{max} of 30 Å). The R_w of the fit against the cristobalite model data is lowest for all length scales at 100 K, suggesting a long-range structural transition upon cooling.

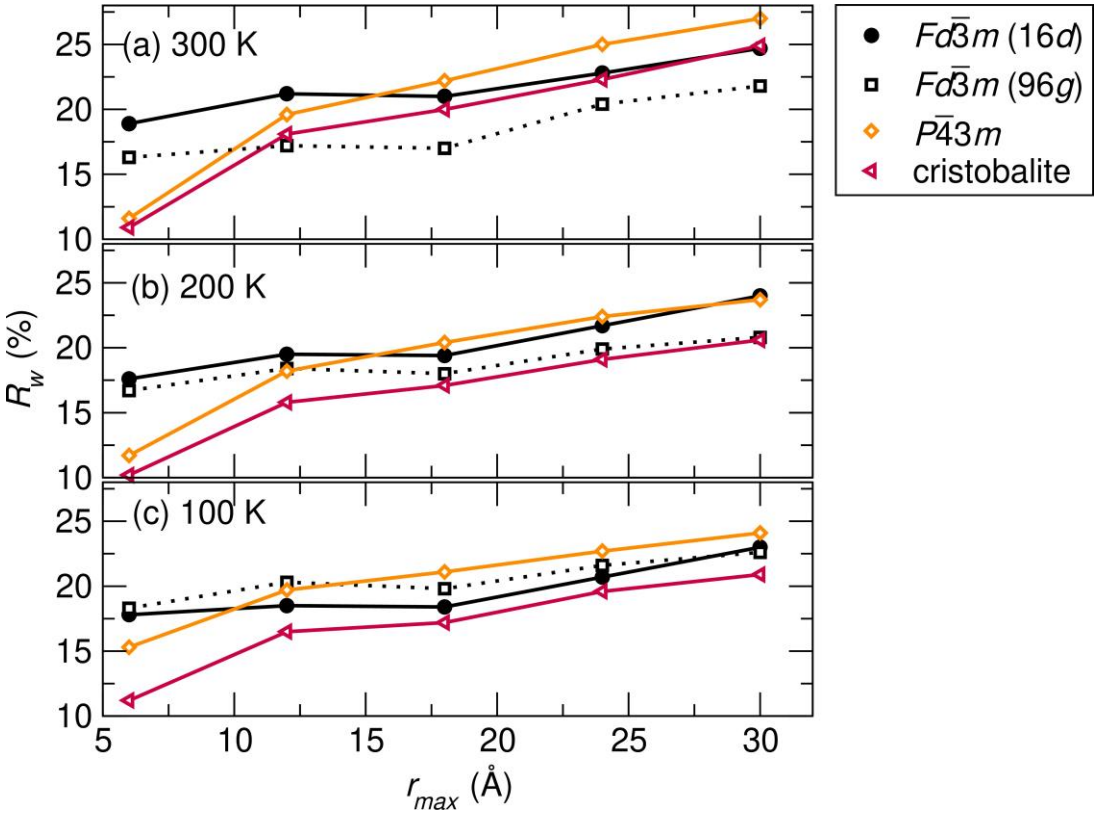

Figure 4-4: Goodness-of-fit parameter R_w of the various local models fit against joint NPDF (NOMAD, SNS) and XPDF (28-ID-1, BNL) data as a function of r-range at (a) 300 K,(b) 200 K, and (c) 100 K. The most local fit (r =1.6–6 Å) is best described with the lowest R_w by the cristobalite model at all temperatures, as well as intermediate (r =1.6–12,18 Å) and long-ranges (r =1.6–24, 30 Å) at lower temperatures, whereas the lowest R_w is observed for the cubic $Fd\bar{3}m$ (96g) model with the intermediate and long-range data at 300 K.

To investigate the presence of a phase transition upon cooling, the reciprocal space neutron diffraction data (NOMAD, SNS, ORNL) was fit against the cristobalite models obtained from the 30 Å fits at 300, 200, and 100 K. Compared to the $Fd\bar{3}m$ model, the cristobalite model yielded a higher R_w at room temperature (5.5% for cubic vs. 10.2% for cristobalite). Fits with the cristobalite model improved with lower temperature but were not statistically significant enough to suggest a long-range phase transition (6.2% for cubic vs. 9.1% for cristobalite at 100 K).

To further investigate the existence of structural transitions upon cooling and the structural influence on physical properties, heat capacity and dielectric permittivity measurements were performed on the samples. The dielectric permittivity at room temperature is in agreement with previous literature on lead niobates,[52] and indicates a feature at approximately 220 K, shown in Figure 4-5a, which is reproducible with other samples of the same composition. A relatively high and consistent dielectric permittivity is observed across the measured range, accompanied by low loss ($\tan\delta$ less than 0.01). The shape of the 220 K feature does not indicate a ferroelectric phase transition - which would be indicated by a peak in the dielectric data at a transition temperature - it does suggest there may be a structural change at this temperature, which is consistent with or observations of a cristobalite-type distortion persisting at longer length scales upon cooling.

The heat capacity measurements were performed through differential scanning calorimetry (DSC, Figure 4-5b) and using a physical properties measurement system (PPMS) to investigate behavior at lower temperatures. Heat capacity measurements do not indicate any apparent long-range phase transitions in the sample upon cooling, which supports $Fd\bar{3}m$ as the best structural description of the diffraction data at all temperatures.

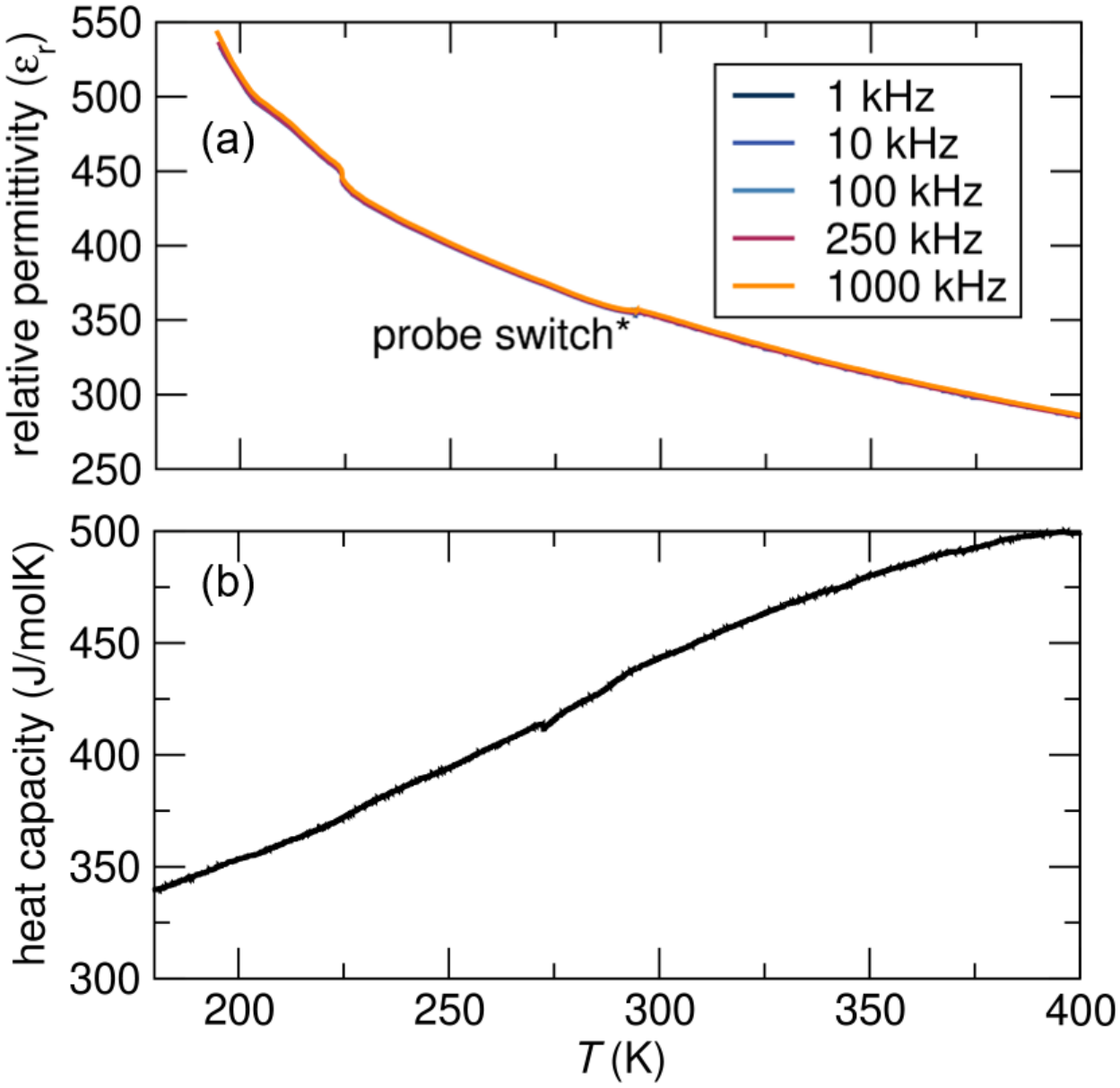

Figure 4-5: (a) Dielectric permittivity as a function of temperature at various frequencies; (b) heat capacity as a function of temperature measured by differential scanning calorimetry.

* indicates where the data was connected, collected by separate low temperature and high temperature probes.

4.4. Discussion

Of the candidate distortion models considered, the cristobalite-type distortion better describes the M-O bond lengths (compared to the $Fd\bar{3}m$ structure, illustrated in Figure 4-6) by capturing the metal coordination environments more successfully. The areas of the PDFs that are most improved with the cristobalite model are the Pb-dependent correlations, and while the distorted model may be a better description of the Nb–O peaks (indicating SOJT activity), it is difficult to assess given the overlap with the broadened Pb–O peaks. An element specific local probe such as solid-state NMR or X-ray absorption are needed to investigate distortions in the Nb coordination environment. In addition to the coordination environments, the peaks between 4–4.5 Å are better captured with this cristobalite model. The partial PDFs from the high symmetry $Fd\bar{3}m$ are plotted in Figure 4-S2, and it can be seen that the peaks between 4–4.5 Å are primarily the first M –M interaction as well as O–O correlations, indicating that the cristobalite structure is the best description of the interactions between neighboring tetrahedral sub-units. In addition to these local structural interactions, the cubic $Fd\bar{3}m$ models show poorer fits to the data up to approximately 13 Å (approximately the distance of the diagonal of the face of one unit cell), but the difference curves shown in the Figures 4-S3 and 4-S4 fits show a qualitatively better fit to the cubic model at all temperatures past 13 Å up to 30 Å. This supports our observations through Rietveld and calorimetric analysis that the material does not undergo a clear phase transition, but suggests that the global structure, while cubic, might be better described somewhat disordered version of the cristobalite structure that averages out to appear cubic.

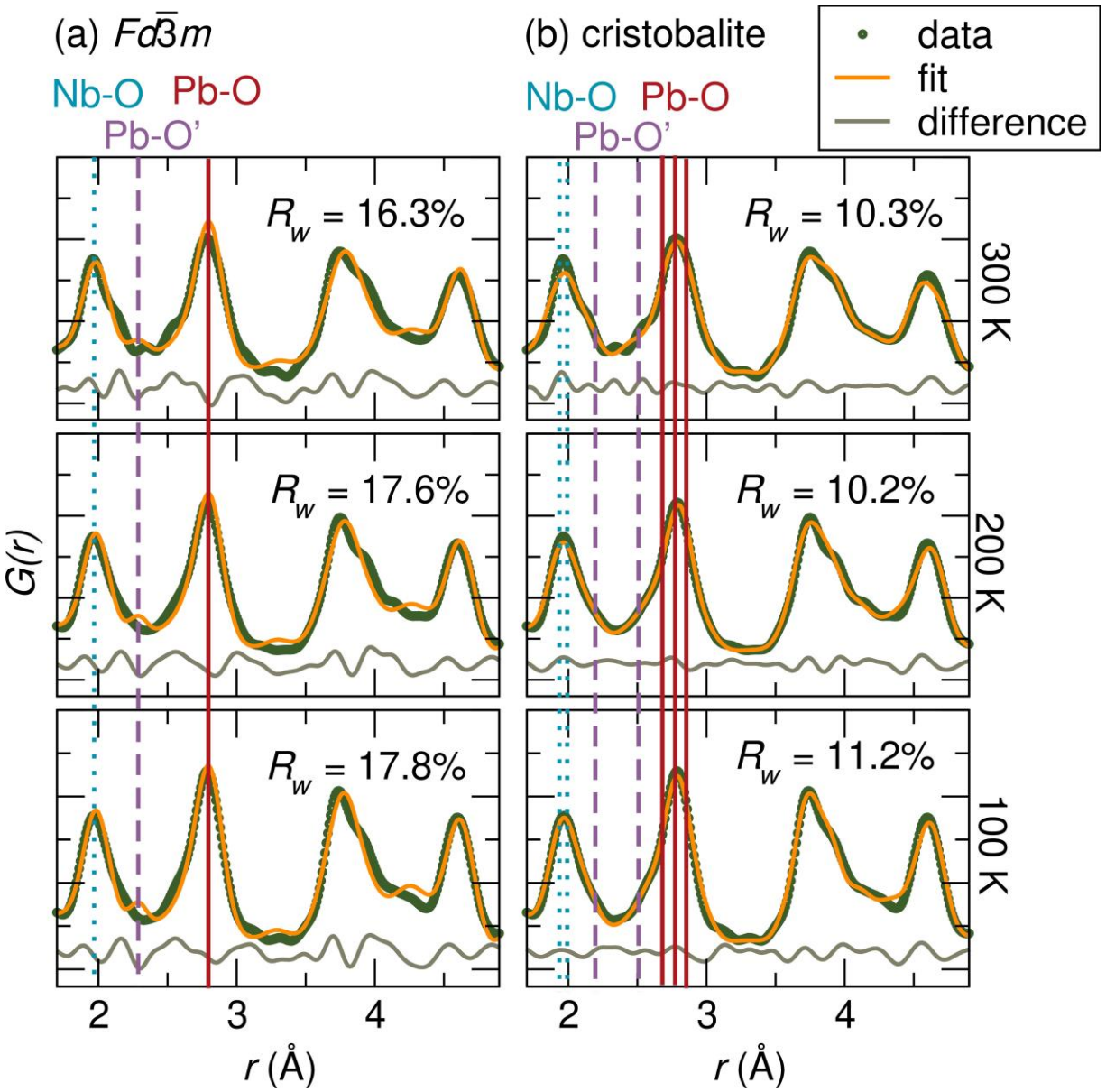

Figure 4-6: Local fits of the NPDF data (NOMAD, SNS) as a function of temperature against the (a) cubic Fd$\bar{3}$m model and the (b) cristobalite model indicates a better fit is obtained at all temperatures with the cristobalite-type distortion. Dashed lines indicate M -O bond lengths, which are still not well-described at room temperature, indicating a further distortion of the local structure upon warming.

It is well understood that the low temperature specific heats of highly disordered materials such as glasses and other amorphous systems illustrate deviation from the Debye Model,[75] which estimates the phonon contribution to the specific heat in a solid material. The observed excess specific heat arises from low energy vibrational modes that are not captured by the Debye model and is observed as a peak in a plot of C/T^3 as a function of temperature. This deviation from Debye behavior has been observed in pyrochlores that exhibit charge ice frustration of lone pair-bearing cations, with the temperature of the peak maxima occurring at lower temperatures (and higher C/T^3) the more disordered the material. Figure 4-7 illustrates our data presented in context with data from other pyrochlores in the literature. $Y_2Ti_2O_7$ serves as a good reference pyrochlore for Debye behavior,[76] as it lacks lone pair cations, and its low temperature heat capacity can be predicted by the Debye model. Contrary to $Y_2Ti_2O_7$, the charge-ice $Bi_2Ti_2O_7$ is documented to have a high degree of disorder due to the stereochemically active lone pair cation Bi^{3+}.[76] It can be observed that the data for $Bi_2Ti_2O_7$ peaks at the lowest temperature and has the highest value at its peak, a result of the highly-disordered lone pairs. While $Pb_2Ru_2O_{6.5}$ also has lone pairs associated with its *A*-site cation, the presence of ordered O' vacancies allows the lone pair distortions to order, resulting in a higher temperature and lower value of the peak maximum.[51] It should be noted that even though these lone pairs are ordered, they still contribute to the phonon behavior in excess of the Debye model. Our $Pb_{1.5}Nb_2O_{6.5}$ measurements exhibit temperature and peak maximum values closer to that of $Bi_2Ti_2O_7$, which is in agreement with disordered vacancies and lone pair driven distortions in the material.

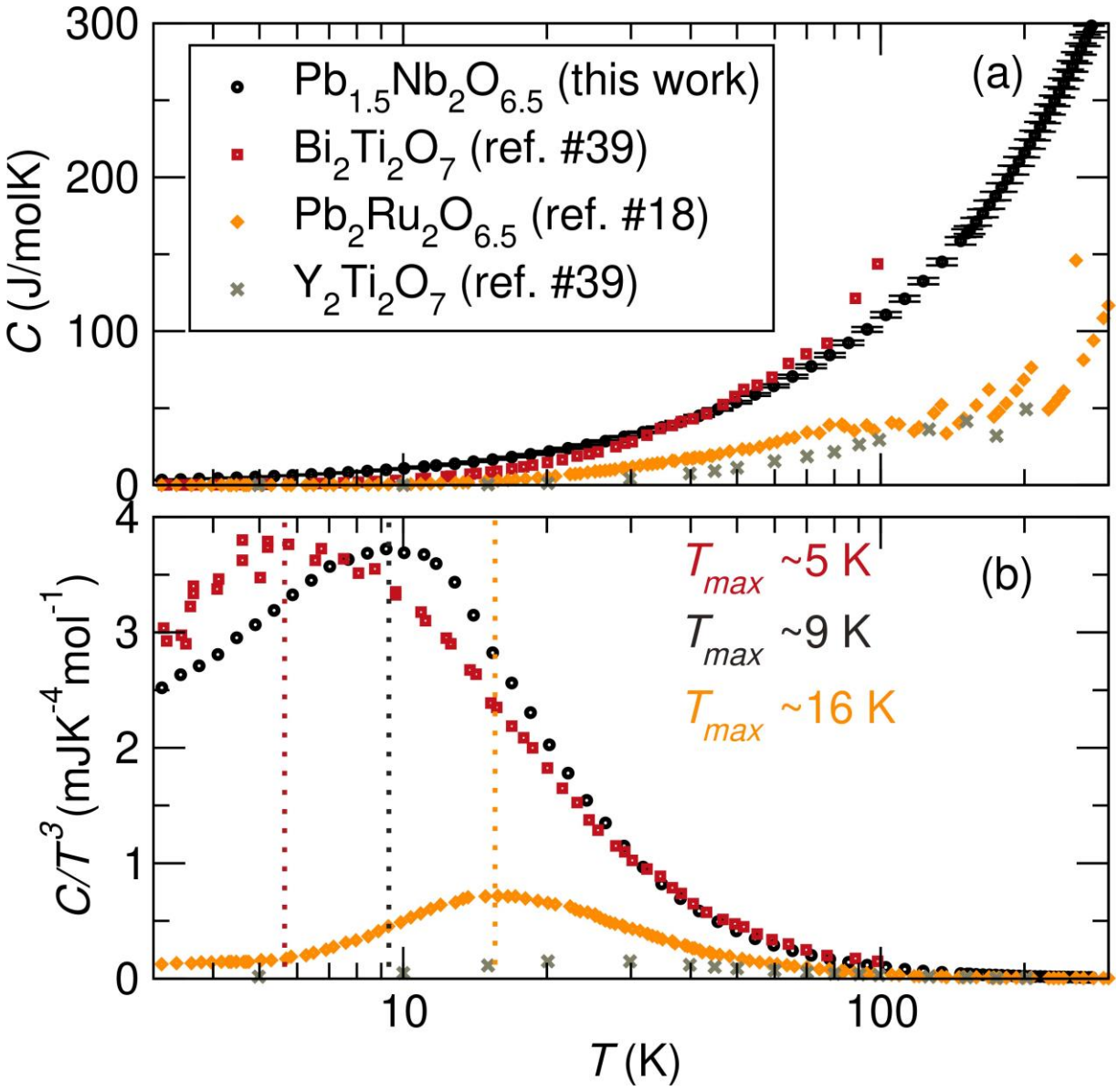

Figure 4-7: (a) Specific heat (C) and (b) C/T^3 vs. T of $Pb_{1.5}Nb_2O_{6.5}$ (black) compared with data from the literature on other pyrochlores (error bars represent one σ). $Y_2Ti_2O_7$ (grey) exhibits the least amount of disorder and Debye-like behavior (data from ref. 75.) $Pb_2Ru_2O_{6.5}$ (yellow) has a small degree of disorder due to stereochemically active lone pairs (data from ref. 51.), but the correlated ordering of these distortions results in a much more ordered structure than the charge ice $Bi_2Ti_2O_7$ (red), which has the highest amount of disorder of the samples (data from ref. 75).

The existence and ordering of the O' vacancies in $Pb_2Ru_2O_{6.5}$ are consequential on the ordering of lone pair driven distortions in the material. To understand the interplay between vacancy and lone pair distortions in $Pb_{1.5}Nb_2O_{6.5}$, density functional theory (DFT) calculations were performed on the distorted cristobalite model to understand the nature of the stereochemically active lone pair. Electron localization functions (ELF) reveal that lone pair density forms on Pb sites which are undercoordinated by O' and directly adjacent to a vacancy. However, lone pair density is not apparent on Pb sites which are fully coordinated by O' species, and the electron density around the Pb atom is spherical and more s-like in nature. Such behavior is demonstrated in Figure 4-8, where localized lone pair density is present on the undercoordinated Pb site next to a vacancy (indicated by a dashed circle) and faces towards the vacant O' site. This suggests that a lone pair driven distortion only occurs when a Pb cation is near a vacancy. This is similar to conclusions about the role of vacancies in the formation of dipoles in $Pb_2Ru_2O_{6.5}$,[51] where ordering of these vacancies is tied to the ordering of the lone pair distortions. In $Pb_{1.5}Nb_2O_{6.5}$, the vacancies are not ordered, and thus any lone pair driven dipoles are spatially disordered, preventing any global phase transition and giving rise to the observed low temperature structural and heat capacity behavior. This work additionally poses the question of chemical considerations and vacancy formation in the cubic $Fd\bar{3}m$ structure. A limited number of Pb-based pyrochlores form the cubic structure with vacancies on both the *A* and O' sites. Such pyrochlores, including $Pb_{1.5}Nb_2O_{6.5}$ [52] and $Pb_{1.5}Ta_2O_{6.5}$,[53] possess relatively electropositive *B*-site cations with a 5+ oxidation state. Other Pb-based cubic pyrochlores, such as $Pb_2Tc_2O_{7-x}$,[77] $Pb_2Ru_2O_{6.5}$,[51] $Pb_2Rh_2O_{7-x}$,[78] $Pb_2Re_2O_{7-x}$,[79] $Pb_2Os_2O_{7-x}$,[80] and $Pb_2Ir_2O_{6.5}$,[81] possess more electronegative *B*-site cations with mixed-valent 4+/5+ oxidation states and exhibit vacancies on the O' site. When the *B*-site cation only exhibits a 4+ oxidation state (such as in $Pb_2Sn_2O_6$[15]), the *A*-site is fully occupied and the O' vacant to maintain charge neutrality. This suggests that the identity and chemistry of the *B*-site cation is a critical component in the formation

of vacancies (and by extension lone pair behavior) in Pb-pyrochlores. A detailed DFT study of the relationship between vacancy formation, ordering schemes, proximity to Pb (and Pb vacancies) and consequent lone pair expression in the high symmetry $Fd\bar{3}m$ phase of $Pb_{1.5}Nb_2O_{6.5}$ is the subject of a forthcoming manuscript.

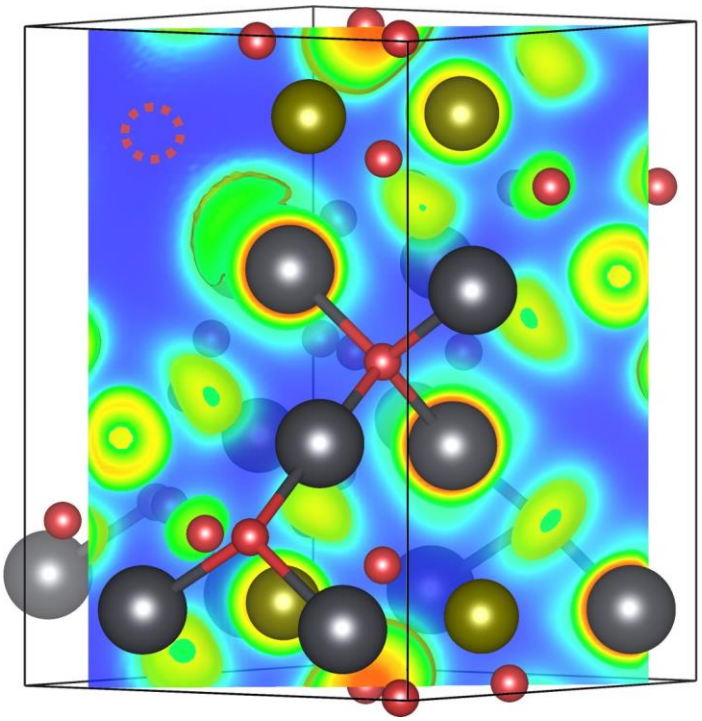

Figure 4-8: Electron localization function (ELF) of the distorted cristobalite structure shown along a (110) slice of the unit cell with an isosurface level set to 0.4. The location of an O' vacancy is indicated by the red dashed circle.

4.5. Conclusion

It is evident through this work that the lone pair behavior of $Pb_{1.5}Nb_2O_{6.5}$ is complex and directly tied to the nature of the vacancies on the O' site of the pyrochlore network. Both the vacancies and the lone pair driven distortions of the Pb cations are globally disordered in the cubic $Fd\bar{3}m$ structure, and local analysis reveals that these distortions can be described by the cristobalite structure. This cristobalite distortion persists to longer length scales upon cooling, and at low temperatures, it is suggested that the global structure may be more accurately described as a disordered cristobalite-type structure. Interestingly, closer inspection of the variable temperature data (displayed together in the supporting information Figure 4-S5) reveals the appearance of shoulders on the peaks that correspond to the Pb–O' bond distances in the pyrochlore structure. This apparent lowering of the local symmetry at high temperatures is similar to the observation of *emphanisis* in lone pair containing materials PbTe,[54] SnTe,[55] and $CsSnBr_3$,[56] suggesting that there may be multiple effects of the lone pair cation on the resulting structural behavior. This work reiterates the impact of vacancies on lone pair expression in Pb pyrochlores and demonstrates that controlling the ordering of vacancies is critical to long-range correlations of lone pair distortions on the pyrochlore network, which in turn are critical to driving properties, such as the sustained elevated dielectric behavior shown herein.

4.6. Acknowledgements

JO and GL were supported by Bates College internal funding and the National Science Foundation (NSF) through DMR 1904980. Work by UD and RTM was supported by the NSF under DMR 2113689. We acknowledge the support of the National Institute of Standards and Technology, U. S. Department of Commerce, in providing the neutron research facilities used in this work. Neutron diffraction data were collected at the National Institute of Standards and Technology Center for Neutron Research (NCNR). This research used resources at the Spallation Neutron Source, a DOE Office of Science User Facility operated by the Oak Ridge National Laboratory, and the authors thank Michelle Everett for assistance with data acquisition. This research used the Pair Distribution Function (PDF) beamline of the National Synchrotron Light Source II, a U.S. Department of Energy (DOE) Office of Science User Facility operated for the DOE Office of Science by Brookhaven National Laboratory under Contract No. DE-SC0012704. Computations were performed on the Bates High Performance Computing Center's *Leavitt* system. JO would like to thank Professor Jeff Oishi for his guidance in using the *Leavitt* HPC cluster at Bates College. GL additionally thanks Ram Seshadri for insightful discussions. Certain commercial equipment, instruments, or materials are identified in this document. Such identification does not imply recommendation or endorsement by the National Institute of Standards and Technology, nor does it imply that the products identified are necessarily the best available for the purpose.

Supporting Information Available

Refined crystallographic data for the nominal $Pb_{1.5}Nb_2O_{6.5}$ with the *A*-site cation in the ideal 16*d* position. Fits of the neutron diffraction data (NOMAD, SNS, ORNL, bank 5) at (a) 300 K, (b) 200 K, and (c) 100 K against the $Fd\bar{3}m$ model with Pb in the 16*d* Wyckoff position. Experimental data collected at various temperatures compared to calculated partials from cubic $Fd\bar{3}m$ model with the *A*-site cation in the 16*d* Wyckoff position. Fits of the NPDF data (NOMAD, SNS, ORNL) against

the cubic $Fd\bar{3}m$ model at (a) 300K, (b) 200 K, (c) 100K. Fits of the NPDF data (NOMAD, SNS, ORNL) against the cubic $Fd\bar{3}m$ model at 300K, (b) 200 K, (c) 100K. Variable temperature (a) neutron (NOMAD, SNS) and (b) X-ray (28-ID-1, BNL) PDF data from 300 to 100 K.

4.7. References

1. Converse, E. S.; Li, J.; Haskel, D.; LaBarre, P. G.; Ramirez, A. P.; Subramanian, M. A. Os^{4+} Instability in the Pyrochlore Structure: $Tl_{2-x}Bi_xOs_2O_{7-y}$. *Inorganic Chemistry* **2020**, *59*, 1227–1233.
2. Deng, Z. Q.; Niu, H. J.; Kuang, X. J.; Allix, M.; Claridge, J. B.; Rosseinsky, M. J. Highly Conducting Redox Stable Pyrochlore Oxides. *Chemistry of Materials* **2008**, *20*, 6911–6916.
3. Cook, W. R.; Jaffe, H. Ferroelectricity in Oxides of Fluorite Structure. *Physical Review* **1953**, *89*, 1297–1298.
4. Kako, T.; Kikugawa, N.; Ye, J. Photocatalytic activities of $AgSbO_3$ under visible light irradiation. *Catalysis Today* **2008**, *131*, 197–202, Recent advances in catalysis - selected papers from APCAT 4 (Singapore, 6-8 December 2006).
5. Uma, S.; Singh, J.; Thakral, V. Facile Room Temperature Ion-Exchange Synthesis of Sn^{2+} Incorporated Pyrochlore-Type Oxides and Their Photocatalytic Activities. *Inorganic Chemistry* **2009**, *48*, 11624–11630.
6. Reimers, J.; Greedan, J.; Sato, M. The crystal structure of the spin-glass pyrochlore, $Y_2Mo_2O_7$. *Journal of Solid State Chemistry* **1988**, *72*, 390–394.
7. Yang, J.; Dai, J.; Liu, Z.; Yu, R.; Hojo, H.; Hu, Z.; Pi, T.; Soo, Y.; Jin, C.; Azuma, M.; Long, Y. High-Pressure Synthesis of the Cobalt Pyrochlore Oxide $Pb_2Co_2O_7$ with Large Cation Mixed Occupancy. *Inorganic Chemistry* **2017**, *56*, 11676–11680.
8. Babu, G. S.; Valant, M.; Page, K.; Llobet, A.; Kolodiazhnyi, T.; Axelsson, A.-K. New $(Bi_{1.88}Fe_{0.12})(Fe_{1.42}Te_{0.58})O_{6.87}$ Pyrochlore with Spin-Glass Transition. *Chemistry of Materials* **2011**, *23*, 2619–2625.
9. Pomjakushina, E.; Pomjakushin, V.; Rolfs, K.; Karpinski, J.; Conder, K. New Synthesis Route and Magnetic Structure of Tm2Mn2O7 Pyrochlore. *Inorganic Chemistry* **2015**, *54*, 9092–9097.
10. Fujihara, S.; Tokumo, K. Multiband Orange-Red Luminescence of Eu^{3+} Ions Based on the Pyrochlore-Structured Host Crystal. *Chemistry of Materials* **2005**, *17*,5587–5593.
11. Burggraaf, A.; van Dijk, T.; Verkerk, M. Structure and conductivity of pyrochlore and fluorite type solid solutions. *Solid State Ionics* **1981**, *5*, 519–522, Proceedings of the International Conference on Fast Ionic Transport in Solids.
12. Pandey, J.; Shrivastava, V.; Nagarajan, R. Metastable $Bi_2Zr_2O_7$ with Pyrochlore-like Structure: Stabilization, Oxygen Ion Conductivity, and Catalytic Properties. *Inorganic Chemistry* **2018**, *57*, 13667–13678.
13. Radhakrishnan, A. N.; Prabhakar Rao, P.; Mahesh, S. K.; Vaisakhan Thampi, D. S.; Koshy, P. Role of Bond Strength on the Lattice Thermal Expansion and Oxide Ion Conductivity in Quaternary Pyrochlore Solid Solutions. *Inorganic Chemistry* **2012**, *51*, 2409–2419.
14. Marlton, F. P.; Zhang, Z.; Zhang, Y.; Proffen, T. E.; Ling, C. D.; Kennedy, B. J. Lattice Disorder and Oxygen Migration Pathways in Pyrochlore and Defect-Fluorite Oxides. *Chemistry of Materials* **2021**, *33*, 1407–1415.
15. Seshadri, R. Lone pairs in insulating pyrochlores: Ice rules and high-k behavior. *Solid state sciences* **2006**, *8*, 259–266.

16. Fennie, C. J.; Seshadri, R.; Rabe, K. M. Lattice instabilities in cubic pyrochlore $Bi_2Ti_2O_7$. *arXiv preprint arXiv:0712.1846* **2007**,
17. Shoemaker, D. P.; Seshadri, R.; Hector, A. L.; Llobet, A.; Proffen, T.; Fennie, C. J. Atomic displacements in the charge ice pyrochlore $Bi_2Ti_2O_6O$' studied by neutron total scattering. *Physical Review B* **2010**, *81*, 144113.
18. Esquivel-Elizondo, J. R.; Hinojosa, B. B.; Nino, J. C. Bi $_2Ti_2O_7$: It Is Not What You Have Read. *Chemistry of Materials* **2011**, *23*, 4965–4974.
19. Hector, A. L.; Wiggin, S. B. Synthesis and structural study of stoichiometric $Bi_2Ti_2O_7$ pyrochlore. *Journal of Solid State Chemistry* **2004**, *177*, 139–145.
20. Oka, K.; Hojo, H.; Azuma, M.; Oh-ishi, K. Temperature-Independent, Large Dielectric Constant Induced by Vacancy and Partial Anion Order in the Oxyfluoride Pyrochlore $Pb_2Ti_2O_{2-\delta}F_{2\delta}$. *Chemistry of Materials* **2016**, *28*, 5554–5559.
21. Gardner, J. S.; Gingras, M. J. P.; Greedan, J. E. Magnetic pyrochlore oxides. *Rev. Mod. Phys.* **2010**, *82*, 53–107.
22. Subramanian, M.; Aravamudan, G.; Rao, G. S. Oxide pyrochlores—a review. *Progress in Solid State Chemistry* **1983**, *15*, 55–143.
23. Radosavljevic, I.; Evans, J.; Sleight, A. Synthesis and Structure of Pyrochlore-Type Bismuth Titanate. *Journal of Solid State Chemistry* **1998**, *136*, 63–66.
24. Avdeev, M.; Haas, M.; Jorgensen, J.; Cava, R. Static disorder from lone-pair electrons in $Bi_{2-x}M_xRu_2O_{7y}$(M=Cu,Co;x=0,0.4) pyrochlores. *Journal of Solid State Chemistry* **2002**, *169*, 24–34.
25. Levin, I.; Amos, T.; Nino, J.; Vanderah, T.; Randall, C.; Lanagan, M. Structural Study of an Unusual Cubic Pyrochlore $Bi_{1.5}Zn_{0.92}Nb_{1.5}O_{6.92}$. *Journal of Solid State Chemistry* **2002**, *168*, 69–75.
26. Laurita, G.; Page, K.; Sleight, A. W.; Subramanian, M. A. Investigation of the Anion-Deficient Pyrochlore $AgSbO_3$ through Total Scattering Techniques. *Inorganic Chemistry* **2013**, *52*, 11530.
27. Khomskii, D. Electric dipoles on magnetic monopoles in spin ice. *Nature communications* **2012**, *3*, 1–5.
28. Laurita, G.; Seshadri, R. Chemistry, Structure, and Function of Lone Pairs in Extended Solids. *Accounts of Chemical Research* **2022**, *55*, 1004–1014.
29. Halasyamani, P. S. Asymmetric Cation Coordination in Oxide Materials: Influence of Lone-Pair Cations on the Intra-octahedral Distortion in d0 Transition Metals. *Chemistry of Materials* **2004**, *16*, 3586–3592.
30. Megaw, H. *Ferroelectricity in Crystals*; Methuen: London, 1957.
31. Bernard, D.; Lucas, J.; Rivoallan, L. Les Pyrochlores Ferroelectriques Derives de $Cd_2Nb_2O_6S$: Mise en Evidence des Transistions de Phase par des Techniques D'optique Non Lineare. *Solid State Communications* **1976**, *18*, 927–930.
32. Dong, X. W.; Wang, K. F.; Luo, S. J.; Wan, J. G.; Liu, J. M. Coexistence of Magnetic and Ferroelectric Behaviors of Pyrochlore $Ho_2Ti_2O_7$. *Journal of Applied Physics* **2009**, *106*, 104101.
33. Liu, D.; Lin, L.; Liu, M. F.; Yan, Z. B.; Dong, S.; Liu, J.-M. Multiferroicity in Spin Ice

$Ho_2Ti_2O_7$: An Investigation on Single Crystals. *Journal of Applied Physics* **2013**, *113*, 17D901.

34. Saitzek, S.; Shao, Z.; Bayart, A.; Ferri, A.; Huvé, M.; Roussel, P.; Desfeux, R. Ferroelec- tricity in $La_2Zr_2O_7$ Thin Films with a Frustrated Pyrochlore-Type Structure. *Journal of Materials Chemistry C* **2014**, *2*, 4037.
35. Kimura, M.; Nanamatsu, S.; Kawamura, T.; Matsushita, S. Ferroelectric, Electro-optic and Piezoelectric Properties of $Nd_2Ti_2O_7$ Single Crystal. *Japanese Journal of Applied Physics* **1974**, *13*, 1473–1474.
36. McQueen, T. M.; West, D. V.; Muegge, B.; Huang, Q.; Noble, K.; Zandbergen, H. W.; Cava, R. J. Frustrated Ferroelectricity in Niobate Pyrochlores. *Journal of Physics Con- densed Matter* **2008**, *20*, 235210.
37. Shirane, G.; Pepinsky, R. Dielectric, X-Ray, and Optical Study of Ferroelectric $Cd_2Nb_2O_7$ and Related Compounds. *Physical Review* **1953**, *92*, 504.
38. Jona, F.; Shirane, G.; Pepinsky, R. Dielectric, X-Ray, and Optical Study of Ferroelectric $Cd_2Nb_2O_7$ and Related Compounds. *Physical Review* **1955**, *98*, 903–909.
39. Tachibana, M.; Kawaji, H.; Atake, T. Calorimetric Investigation of Successive Phase Transitions in $Cd_2Nb_2O_7$. *Physical Review B* **2004**, *70*, 064103.
40. Fischer, M.; Malcherek, T.; Bismayer, U.; Blaha, P.; Schwarz, K. Structure and Stability of $Cd_2Nb_2O_7$ and $Cd_2Ta_2O_7$ Explored by Ab Initio Calculations. *Physical Review B* **2008**, *78*, 014108.
41. Malcherek, T.; Bismayer, U.; Paulmann, C. The Crystal Structure of $Cd_2Nb_2O_7$): Sym- metry Mode Analysis of the Ferroelectric Phase. *Journal of Physics Condensed Matter* **2010**, *22*, 205401.
42. Tachibana, M.; Fritsch, K.; Gaulin, B. D. X-ray Scattering Studies of Structural Phase Transitions in Pyrochlore $Cd_2Nb_2O_7$. *Journal of Physics Condensed Matter* **2013**, *25*, 435902.
43. Smolenskii, G. A.; Salaev, F. M.; Kamzina, L. S.; Krainik, N. N.; Dorogovtsev, S. N. The Investigation of Successive Phase Transitions in Cadmium Pyroniobate Crystal. *Soviet Technical Physics Letter* **1983**, *10*, 253.
44. Smolenskii, G. A.; Krainik, N. N.; Trepakov, V. A.; Babinsky, A. V. Photoluminescence and Carrier Drift Mobility at the Ferroelectric Phase Transitions. *Ferroelectrics* **2011**, *26*, 835–838.
45. Lukaszewicz, K.; Pietraszko, A.; Stepie-Damm, J.; Kolpakova, N. Temperature De- pendence of the Crystal Structure and Dynamic Disorder of Cadmium in Cadmium Pyroniobates $Cd_2Nb_2O_7$ and $Cd_2Ta_2O_7$. *Materials Research Bulletin* **1994**, *29*, 987– 992.
46. Kolpakova, N. N.; Waplak, S.; Bednarski, W. EPR Spectroscopy and Optical Mi- croscopy Study of Ferroic States in Pyrochlore. *Journal of Physics Condensed Matter* **1998**, *10*, 9309–9316.
47. Buixaderas, E.; Kamba, S.; Petzelt, J.; Savinov, M.; Kolpakova, N. N. Phase Transitions Sequence in Pyrochlore $Cd_2Nb_2O_7$ Studied by IR Reflectivity. *Phase Transitions* **2001**, *16*, 9–16.
48. Kolpakova, N. N.; Syrnikov, P. P.; Lebedev, A. O.; Czarnecki, P.; Nawrocik, W.; Perrot, C.;

Szczepanska, L. 2-5 Pyrochlore Relaxor Ferroelectric $Cd_2Nb_2O_7$ and its Fe^{2+}/Fe^{3+} Modifications. *Journal of Applied Physics* **2001**, *90*, 6332–6340.

49. Ye, Z. G.; Kolpakova, N. N.; Rivera, J.-P.; Schmid, H. Optical and Electric Investi- gations of the Phase Transitions in Pyrochlore $Cd_2Nb_2O_7$. *Ferroelectrics* **1991**, *124*, 275–280.
50. Laurita, G.; Hickox-Young, D.; Husremovic, S.; Li, J.; Sleight, A. W.; Macaluso, R.; Rondinelli, J. M.; Subramanian, M. A. Covalency-driven Structural Evolution in the Polar Pyrochlore Series $Cd_2Nb_2O_{7-x}S_x$. *Chemistry of Materials* **2019**, *31*, 7626–7637.
51. Shoemaker, D. P.; Llobet, A.; Tachibana, M.; Seshadri, R. Reverse Monte Carlo neutron scattering study of the 'ordered-ice' oxide pyrochlore $Pb_2Ru_2O_{6.5}$. *Journal of Physics: Condensed Matter* **2011**, *23*, 315404.
52. Ubic, R.; Reaney, I. M. Structure and Dielectric Properties of Lead Pyrochlores. *Journal of the American Ceramic Society* **2002**, *85*, 2472–2478.
53. Menguy, N.; Thuriès, F.; Caranoni, C. Stoichiometry, Defects, and Ordering in Lead Tantalum Oxides with Pyrochlore-Related Structures. *Journal of Solid State Chemistry* **1996**, *126*, 253–260.
54. Bozin, E. S.; Malliakas, C. D.; Souvatzis, P.; Proffen, T.; Spaldin, N. A.; Kanatzidis, M. G.; Billinge, S. J. L. Entropically Stabilized Local Dipole Formation in Lead Chalcogenides. *Science* **2010**, *330*, 1660–1663.
55. Knox, K. R.; Bozin, E. S.; Malliakas, C. D.; Kanatzidis, M. G.; Billinge, S. J. L. Local Off-Centering Symmetry Breaking in the High-Temperature Regime of SnTe. *Phys. Rev. B* **2014**, *89*, 014102.
56. Fabini, D. H.; Laurita, G.; Bechtel, J. S.; Stoumpos, C. C.; Evans, H. A.; Kontos, A. G.; Raptis, Y. S.; Falaras, P.; Van der Ven, A.; Kanatzidis, M. G.; Seshadri, R. Dynamic Stereochemical Activity of the Sn^{2+} Lone Pair in Perovskite $CsSnBr_3$. *J. Amer. Chem. Soc.* **2016**, *138*, 11820–11832.
57. Le Bail, A. Whole Powder Pattern Decomposition Methods and Applications: A Retrospection. *Powder Diffraction* **2005**, *20*, 316–326.
58. Rietveld, H. M. A Profile Refinement Method for Nuclear and Magnetic Structures. *Journal of Applied Crystallography* **1969**, *2*, 65–71.
59. Toby, B. H.; Von Dreele, R. B. *GSAS-II*: the genesis of a modern open-source all-purpose crystallography software package. *Journal of Applied Crystallography* **2013**, *46*, 544–549.
60. Arnold, O. et al. Mantid–Data analysis and visualization package for neutron scattering and μ SR experiments. *Nuclear Instruments and Methods in Physics Research Section A: Accelerators, Spectrometers, Detectors and Associated Equipment* **2014**, *764*, 156 – 166.
61. Olds, D.; Saunders, C. N.; Peters, M.; Proffen, T.; Neuefeind, J.; Page, K. Precise implications for real-space pair distribution function modeling of effects intrinsic to modern time-of-flight neutron diffractometers. *Acta Crystallographica Section A* **2018**, *74*, 293–307.
62. Farrow, C. L.; Juhas, P.; Liu, J. W.; Bryndin, D. B.; Bloch, E. S. J.; Proffen, T.; Billinge, S. J. L. PDFfit2 and PDFgui: computer programs for studying nanostructure in crystals. *J. Phys.: Condens. Matt.* **2007**, *19*, 335219.
63. Juhás, P.; Davis, T.; Farrow, C. L.; Billinge, S. J. L. PDFgetX3: a rapid and highly automatable program for processing powder diffraction data into total scattering pair

distribution functions. *Journal of Applied Crystallography* **2013**, *46*, 560–566.
64. Giannozzi, P.; Baseggio, O.; Bonfà, P.; Brunato, D.; Car, R.; Carnimeo, I.; Cavaz- zoni, C.; de Gironcoli, S.; Delugas, P.; Ferrari Ruffino, F.; Ferretti, A.; Marzari, N.; Timrov, I.; Urru, A.; Baroni, S. Quantum ESPRESSO toward the exascale. *The Journal of Chemical Physics* **2020**, *152*, 154105.
65. Giannozzi, P. et al. Advanced capabilities for materials modelling with Quantum ESPRESSO. *Journal of Physics: Condensed Matter* **2017**, *29*, 465901.
66. Prandini, G.; Marrazzo, A.; Castelli, I. E.; Mounet, N.; Marzari, N. Precision and efficiency in solid-state pseudopotential calculations. *npj Computational Materials* **2018**, *4*, 1–13.
67. Lejaeghere, K.; Bihlmayer, G.; Bj¨orkman, T.; Blaha, P.; Blu¨gel, S.; Blum, V.; Caliste, D.; Castelli, I. E.; Clark, S. J.; Dal Corso, A., et al. Reproducibility in density functional theory calculations of solids. *Science* **2016**, *351*.
68. Momma, K.; Izumi, F. VESTA 3 for Three-Dimensional Visualization of Crystal, Volu- metric and Morphology Data. *Journal of Applied Crystallography* **2011**, *44*, 1272–1276.
69. Bernotat-Wulf, H.; Hoffmann, W. Die Kristallstrukturen der Bleiniobate vom Pyrochlor-Typ. *Zeitschrift fu¨r Kristallographie - Crystalline Materials* **1982**, *158*, 101– 118.
70. Shoemaker, D. P.; Seshadri, R.; Tachibana, M.; Hector, A. L. Incoherent Bi off-centering in $Bi_2Ti_2O_6O'$ and $Bi_2Ru_2O_6O'$: Insulator versus metal. *Phys. Rev. B* **2011**, 84, 064117.
71. Blaha, P.; Singh, D. J.; Schwarz, K. Geometric Frustration, Electronic Instabilities, and Charge Singlets in $Y_2Nb_2O_7$. *Phys. Rev. Lett.* **2004**, *93*, 216403.
72. Talanov, M. V.; Talanov, V. M. Structural Diversity of Ordered Pyrochlores. *Chemistry of Materials* **2021**, *33*, 2706–2725.
73. Trump, B. A.; Koohpayeh, S. M.; Livi, K. J. T.; Wen, J.-J.; Arpino, K. E.; Ra- masse, Q. M.; Brydson, R.; Feygenson, M.; Takeda, H.; Takigawa, M.; Kimura, K.; Nakatsuji, S.; Broholm, C. L.; McQueen, T. M. Universal Geometric Frustration in Pyrochlores. *Nature Communications* **2018**, *9*, 1–10.
74. Bailey, O.; Husremovic, S.; Murphy, M.; Ross, J.; Gong, J.; Olds, D.; Laurita, G. Compositional influence of local and long-range polarity in the frustrated pyrochlore system $Bi_{2x}RE_xTi_2O_7$ (RE = Y^{3+},Ho^{3+}). *J. Mater. Chem. C* **2022**, *10*, 13886.
75. Safarik, D. J.; Schwarz, R. B.; Hundley, M. F. Similarities in the C_p/T^3 Peaks in Amorphous and Crystalline Metals. *Phys. Rev. Lett.* **2006**, *96*, 195902.
76. Melot, B. C.; Tackett, R.; O'Brien, J.; Hector, A. L.; Lawes, G.; Seshadri, R.; Ramirez, A. P. Large low-temperature specific heat in pyrochlore $Bi_2Ti_2O_7$. *Physical Review B* **2009**, *79*, 224111.
77. Kennedy, B. J.; Ablott, T. A.; Avdeev, M.; Carter, M. L.; Losurdo, L.; Saura- Muzquiz, M.; Thorogood, K. J.; Ting, J.; Wallwork, K. S.; Zhang, Z.; Zhu, H.;Thoro- good, G. J. Synthesis and Structure of Oxygen Deficient Lead-Technetium Pyrochlore, the First Example of a Valence V Technetium Oxide. *Frontiers in Chemistry* **2021**, *9*.
78. Sleight, A. W. High pressure synthesis of platinum metal pyrochlores of the type $Pb_2M_2O_{6-7}$. *Materials Research Bulletin* **1971**, *6*, 775–780.
79. Abakumov, A.; Shpanchenko, R.; Antipov, E.; Kopnin, E.; Capponi, J.; Marezio, M.; Lebedev, O.; Van Tendeloo, G.; Amelinckx, S. Synthesis and Structural Study of $Pb_2Re_2O_{7x}$

Pyrochlores. *Journal of Solid State Chemistry* **1998**, *138*, 220–225.
80. Reading, J.; Knee, C. S.; Weller, M. T. Syntheses, structures, and properties of some osmates(iv,v) adopting the pyrochlore and weberite structures. *J. Mater. Chem.* **2002**, *12*, 2376–2382.
81. Kennedy, B. J. Oxygen Vacancies in Pyrochlore Oxides: Powder Neutron Diffraction Study of $Pb_2Ir_2O_{6.5}$ and $Bi_2Ir_2O_{7-2y}$. *Journal of Solid State Chemistry* **1996**, *123*, 14– 20.

Chapter 5 Rietveld Refinement on Cubic Pyrochlore $Fd\bar{3}m$ against Different Models at 100K, 200K, and 300K in $Pb_{1.5}Nb_2O_{6.5}$

Different models including cubic $Fd\bar{3}m$ 16d, cubic $Fd\bar{3}m$ 96g, $F\bar{4}3m$, cristobalite $P2_12_12_1$, and cristobalite $P4_12_12$ were used for analysis of PDF data at 100 K, 200 K, and 300 K. The data were refined using the Rietveld methods in the GSAS-II software. The A-site cation atoms occupy at the Wyckoff 16d position which is in the center of the BO_6 hexagonal ring in an ideal pyrochlore structure, with $Fd\bar{3}m$ space group. When the symmetry of the cubic pyrochlore structure is reduced, the A-site cation is displaced into different Wyckoff positions including 96g (toward the ring) and 32e (above and below the ring plane) site. Banks 4 and 5 cover different *d*-spacing when collecting neutron diffraction data from the NOMAD instrument. Bank 5 has higher resolution than bank 4.

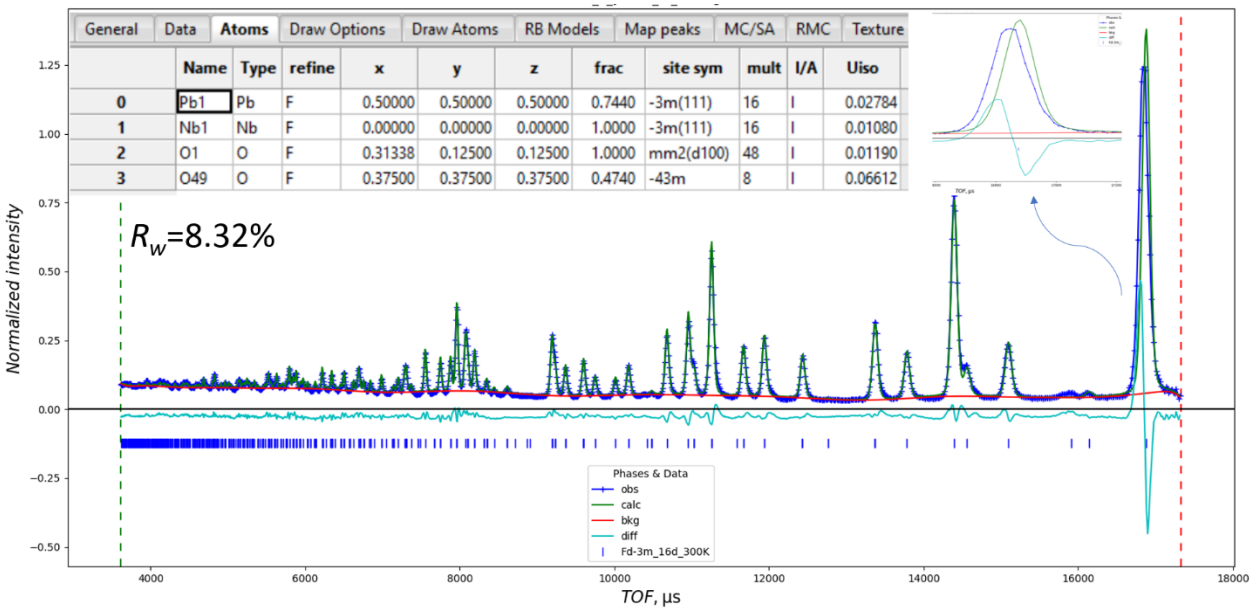

Figure 5-1: Rietveld fit of neutron diffraction data against the cubic $Fd\bar{3}m$ 16d model at 300 K using bank 4 (resulting R_w = 8.32%).

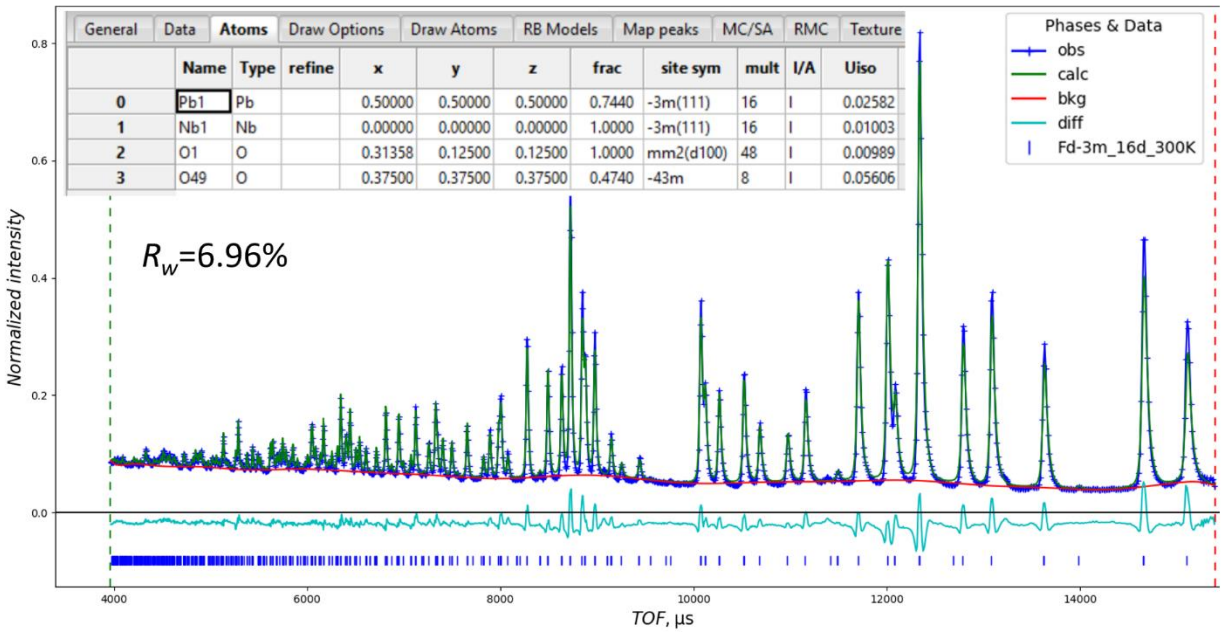

Figure 5-2: Rietveld fit of neutron diffraction data against the cubic $Fd\bar{3}m$ 16d model at 300 K using bank 5 (resulting R_w = 6.96%).

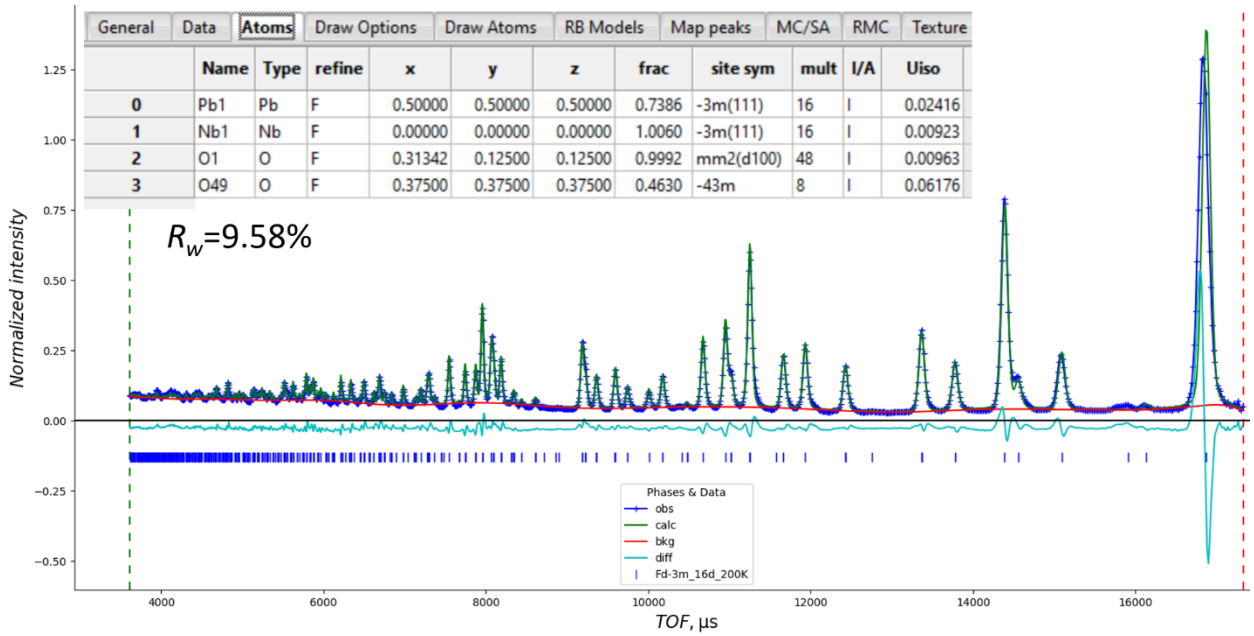

Figure 5-3: Rietveld fit of neutron diffraction data against the cubic $Fd\bar{3}m$ 16d model at 200 K using bank 4 (resulting R_w = 9.58%).

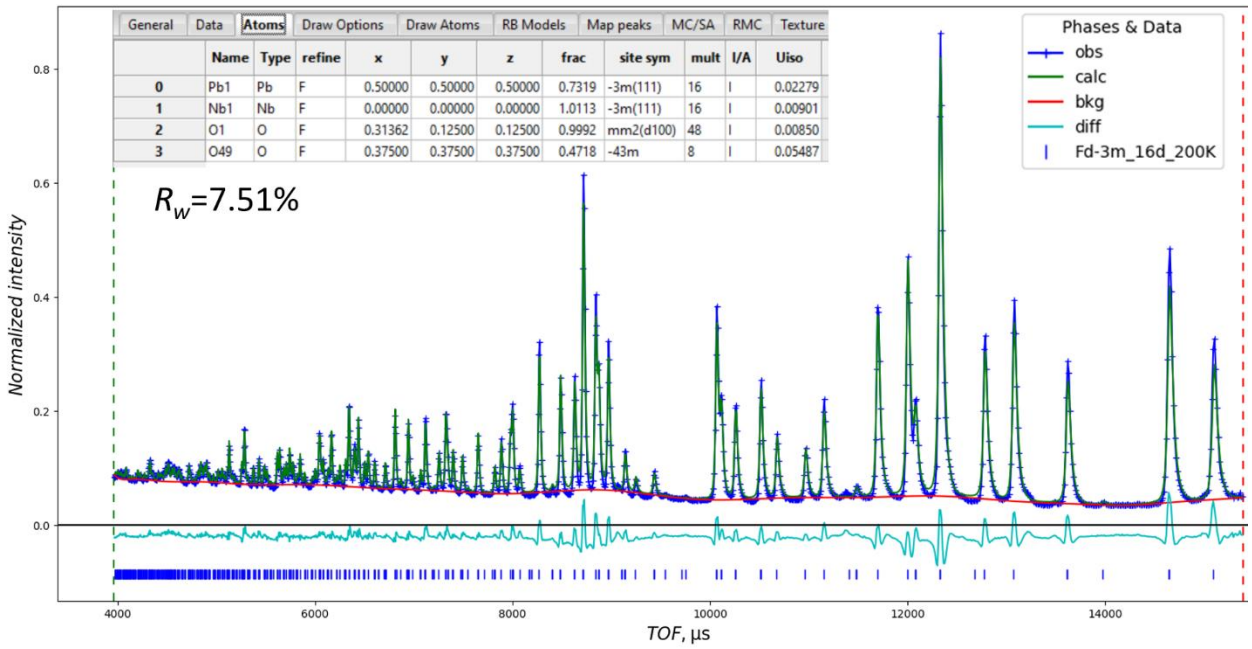

Figure 5-4: Rietveld fit of neutron diffraction data against the cubic $Fd\bar{3}m$ 16d model at 200 K using bank 5 (resulting R_w = 7.51%).

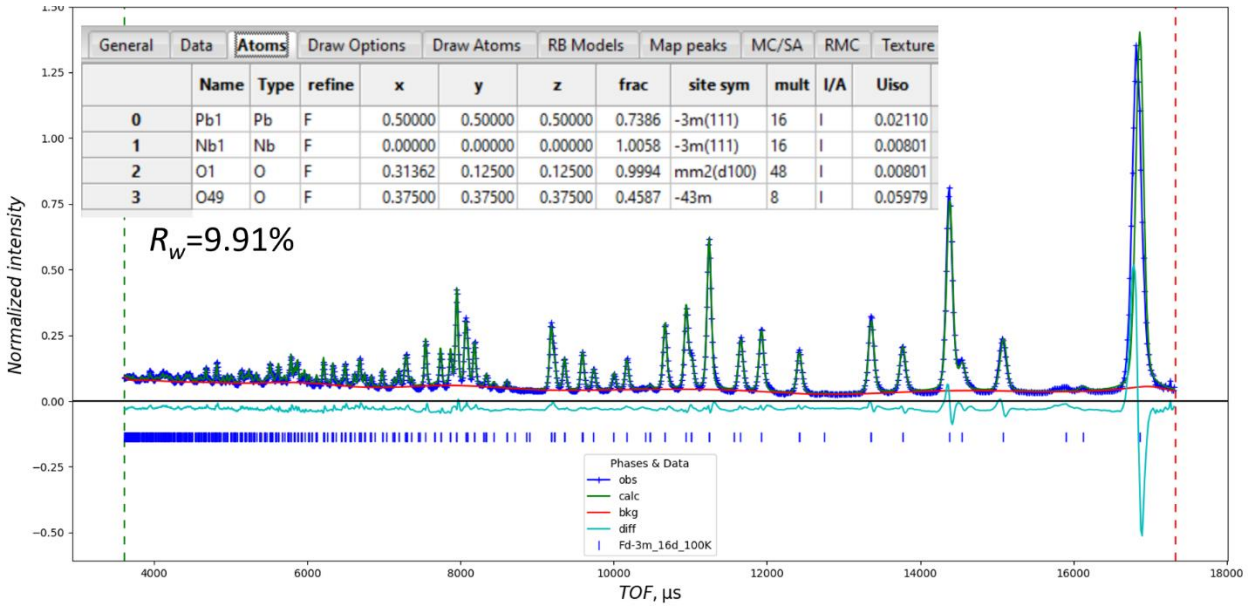

Figure 5-5: Rietveld fit of neutron diffraction data against the cubic $Fd\bar{3}m$ 16d model at 100 K using bank 4 (resulting R_w = 9.91%).

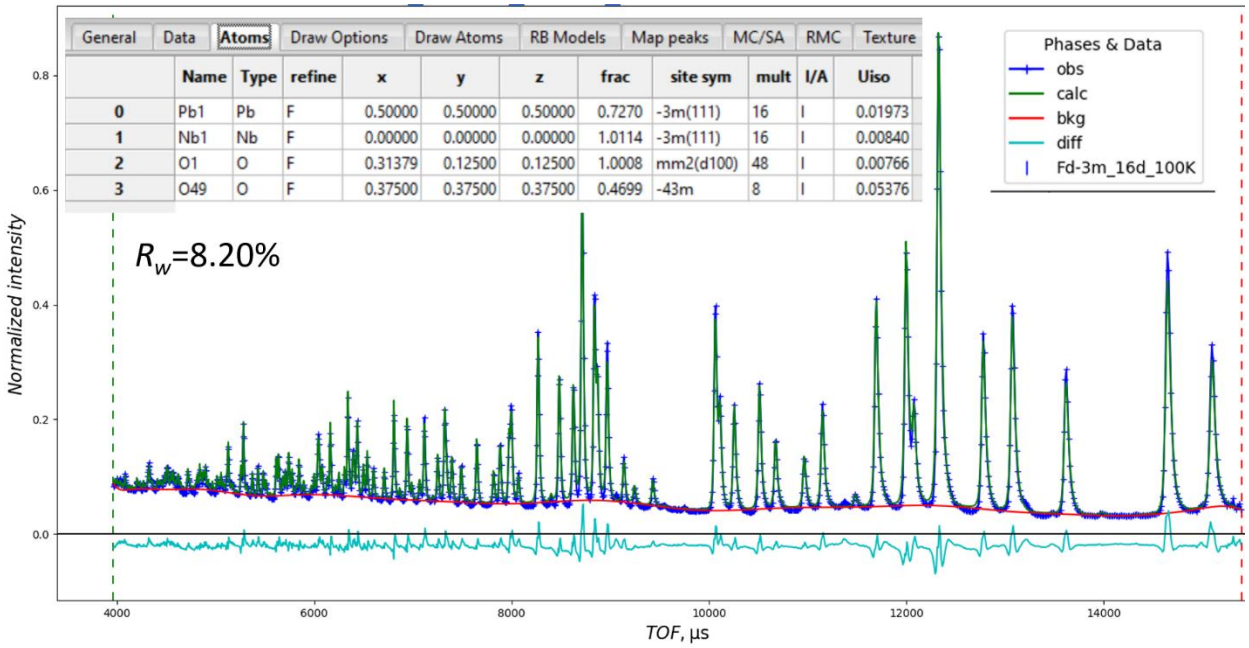

Figure 5-6: Rietveld fit of neutron diffraction data against the cubic Fd$\bar{3}$m 16d model at 100 K using bank 5 (resulting R_w = 8.20%).

Figures 5-1 to 5-6 show the Rietveld fit of diffraction data against the cubic $Fd\bar{3}m$ 16d model at 300 K, 200 K, and 100 K using banks 4 and 5. The summary of these refinements is reported in Figures 5-7 and 5-8 with banks 4 and 5, respectively. The cubic structure is best fit at 300 K and get worse upon colling based on our R_w values for both banks 4 and 5.

NOMAD Cubic Yellow at 300K_Bank 4_Fd-3m_16d R_w=8.32%

General | Data | **Atoms** | Draw Options | Draw Atoms | RB Models | Map peaks | MC/SA | RMC | Texture

	Name	Type	refine	x	y	z	frac	site sym	mult	I/A	Uiso
0	Pb1	Pb	F	0.50000	0.50000	0.50000	0.7440	-3m(111)	16	I	0.02784
1	Nb1	Nb	F	0.00000	0.00000	0.00000	1.0000	-3m(111)	16	I	0.01080
2	O1	O	F	0.31338	0.12500	0.12500	1.0000	mm2(d100)	48	I	0.01190
3	O49	O	F	0.37500	0.37500	0.37500	0.4740	-43m	8	I	0.06612

NOMAD Cubic Yellow at 200K_Bank 4_Fd-3m_16d R_w =9.58%

General | Data | **Atoms** | Draw Options | Draw Atoms | RB Models | Map peaks | MC/SA | RMC | Texture

	Name	Type	refine	x	y	z	frac	site sym	mult	I/A	Uiso
0	Pb1	Pb	F	0.50000	0.50000	0.50000	0.7386	-3m(111)	16	I	0.02416
1	Nb1	Nb	F	0.00000	0.00000	0.00000	1.0060	-3m(111)	16	I	0.00923
2	O1	O	F	0.31342	0.12500	0.12500	0.9992	mm2(d100)	48	I	0.00963
3	O49	O	F	0.37500	0.37500	0.37500	0.4630	-43m	8	I	0.06176

NOMAD Cubic Yellow at 100K_Bank 4_Fd-3m_16d R_w =9.92%

General | Data | **Atoms** | Draw Options | Draw Atoms | RB Models | Map peaks | MC/SA | RMC | Texture

	Name	Type	refine	x	y	z	frac	site sym	mult	I/A	Uiso
0	Pb1	Pb	F	0.50000	0.50000	0.50000	0.7386	-3m(111)	16	I	0.02110
1	Nb1	Nb	F	0.00000	0.00000	0.00000	1.0058	-3m(111)	16	I	0.00801
2	O1	O	F	0.31362	0.12500	0.12500	0.9994	mm2(d100)	48	I	0.00801
3	O49	O	F	0.37500	0.37500	0.37500	0.4587	-43m	8	I	0.05979

Figure 5-7: Refined crystallographic data of cubic $Fd\bar{3}m$ 16d at 100 K, 200 K, and 300 K from bank 4.

NOMAD Cubic Yellow at 300K_Bank 5_Fd-3m_16d R_w =6.96%

General | Data | **Atoms** | Draw Options | Draw Atoms | RB Models | Map peaks | MC/SA | RMC | Texture

	Name	Type	refine	x	y	z	frac	site sym	mult	I/A	Uiso
0	Pb1	Pb		0.50000	0.50000	0.50000	0.7440	-3m(111)	16	I	0.02582
1	Nb1	Nb		0.00000	0.00000	0.00000	1.0000	-3m(111)	16	I	0.01003
2	O1	O		0.31358	0.12500	0.12500	1.0000	mm2(d100)	48	I	0.00989
3	O49	O		0.37500	0.37500	0.37500	0.4740	-43m	8	I	0.05606

NOMAD Cubic Yellow at 200K_Bank 5_Fd-3m_16d R_w =7.53%

General | Data | **Atoms** | Draw Options | Draw Atoms | RB Models | Map peaks | MC/SA | RMC | Texture

	Name	Type	refine	x	y	z	frac	site sym	mult	I/A	Uiso
0	Pb1	Pb	F	0.50000	0.50000	0.50000	0.7319	-3m(111)	16	I	0.02279
1	Nb1	Nb	F	0.00000	0.00000	0.00000	1.0113	-3m(111)	16	I	0.00901
2	O1	O	F	0.31362	0.12500	0.12500	0.9992	mm2(d100)	48	I	0.00850
3	O49	O	F	0.37500	0.37500	0.37500	0.4718	-43m	8	I	0.05487

NOMAD Cubic Yellow at 100K_Bank 5_Fd-3m_16d R_w =8.20%

General | Data | **Atoms** | Draw Options | Draw Atoms | RB Models | Map peaks | MC/SA | RMC | Texture

	Name	Type	refine	x	y	z	frac	site sym	mult	I/A	Uiso
0	Pb1	Pb	F	0.50000	0.50000	0.50000	0.7270	-3m(111)	16	I	0.01973
1	Nb1	Nb	F	0.00000	0.00000	0.00000	1.0114	-3m(111)	16	I	0.00840
2	O1	O	F	0.31379	0.12500	0.12500	1.0008	mm2(d100)	48	I	0.00766
3	O49	O	F	0.37500	0.37500	0.37500	0.4699	-43m	8	I	0.05376

Figure 5-8: Refined crystallographic data of cubic Fd$\bar{3}$m 16d at 100 K, 200 K, and 300 K from bank 5.

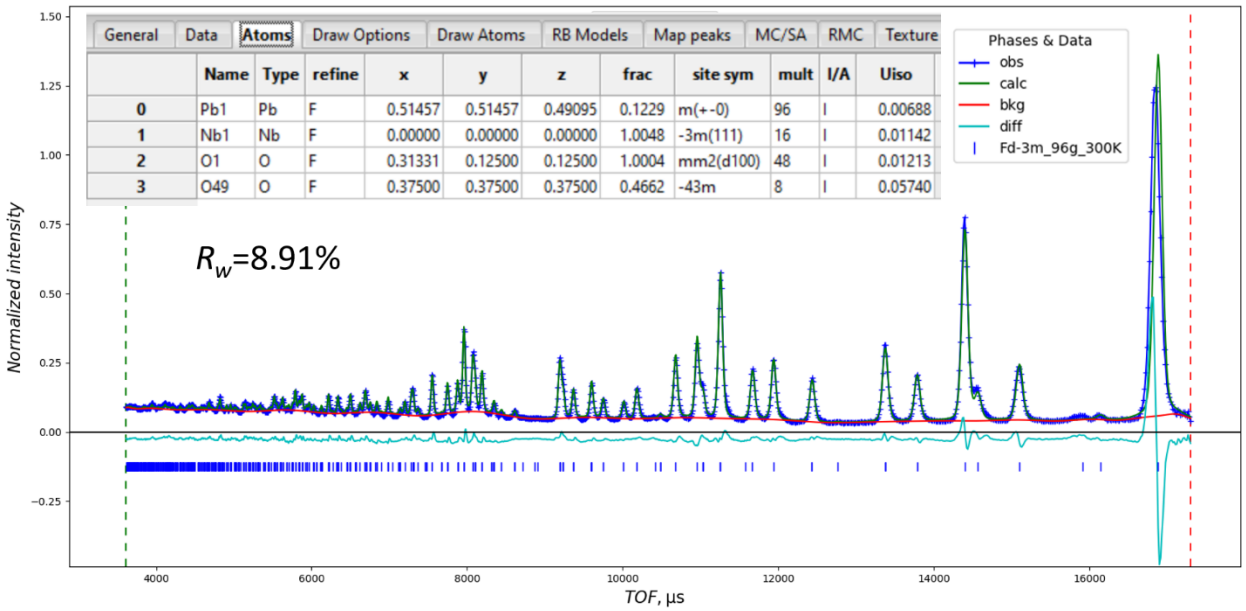

Figure 5-9: Rietveld fit of neutron diffraction data against the cubic $Fd\bar{3}m$ 96g model at 300 K using bank 4 (resulting R_w = 8.91%).

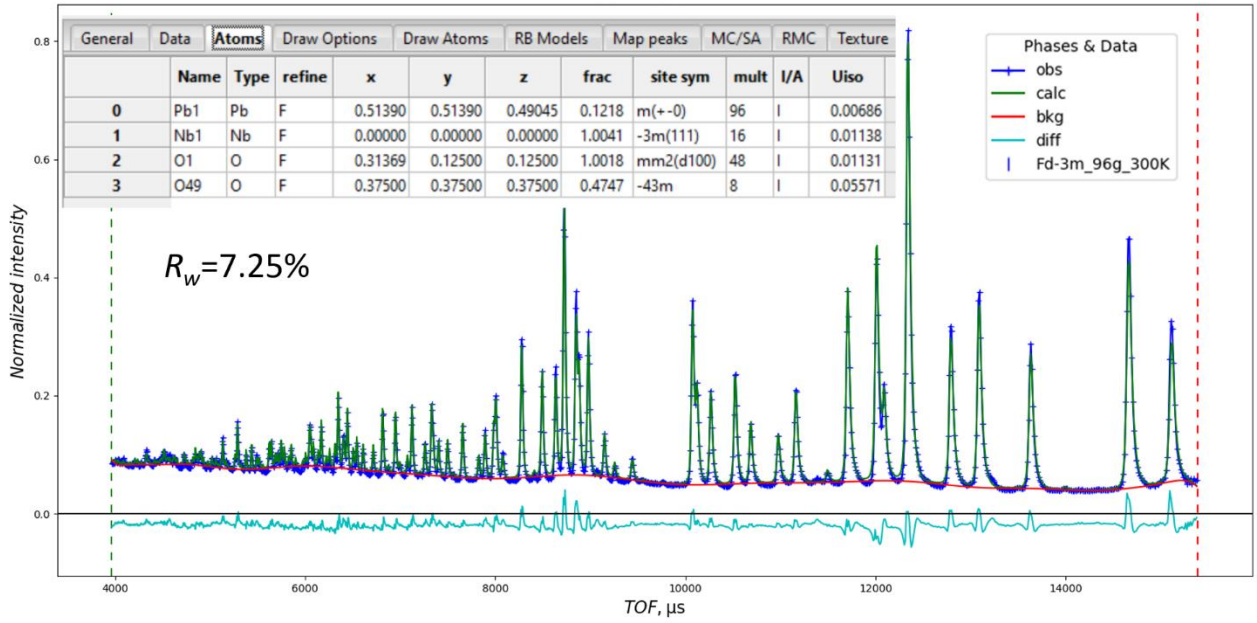

Figure 5-10: Rietveld fit of neutron diffraction data against the cubic $Fd\bar{3}m$ 96g model at 300 K using bank 5 (resulting R_w = 7.25%).

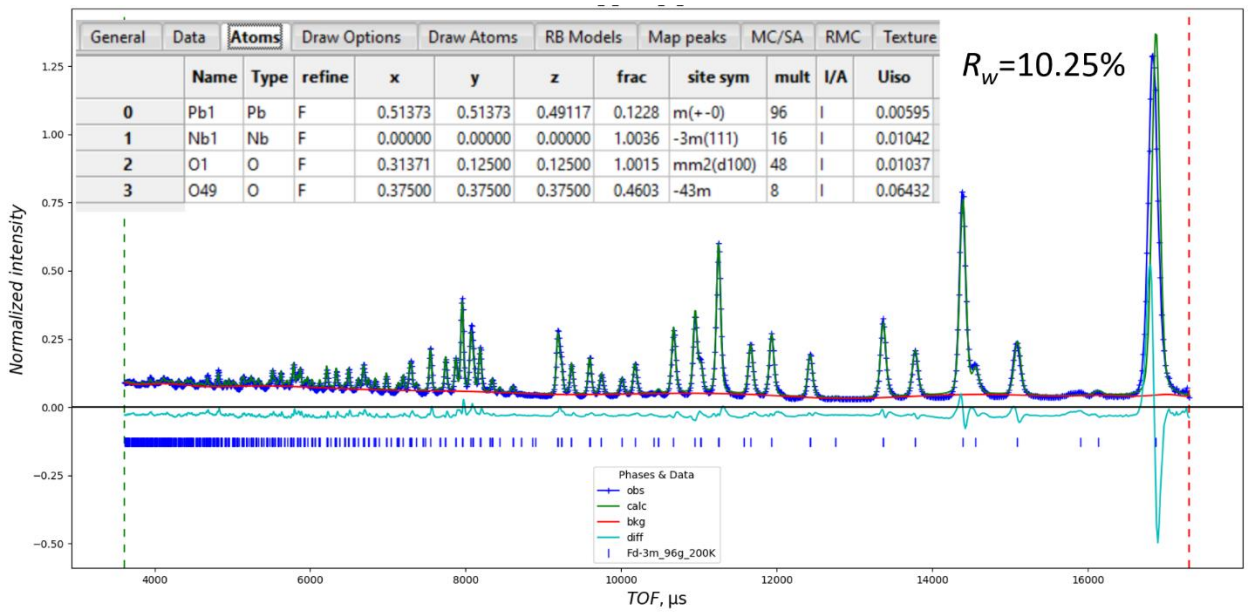

Figure 5-11: Rietveld fit of neutron diffraction data against the cubic Fd$\bar{3}$m 96g model at 200 K using bank 4 (resulting R_w = 10.25%).

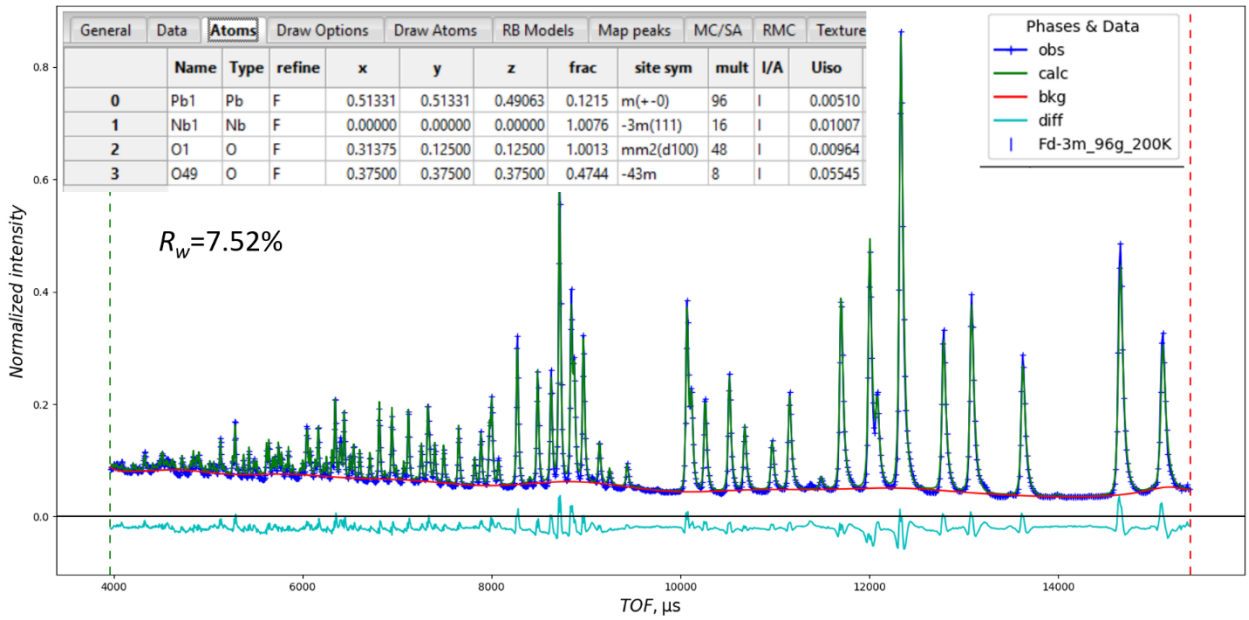

Figure 5-12: Rietveld fit of neutron diffraction data against the cubic Fd$\bar{3}$m 96g model at 200 K using bank 5 (resulting R_w = 7.52%).

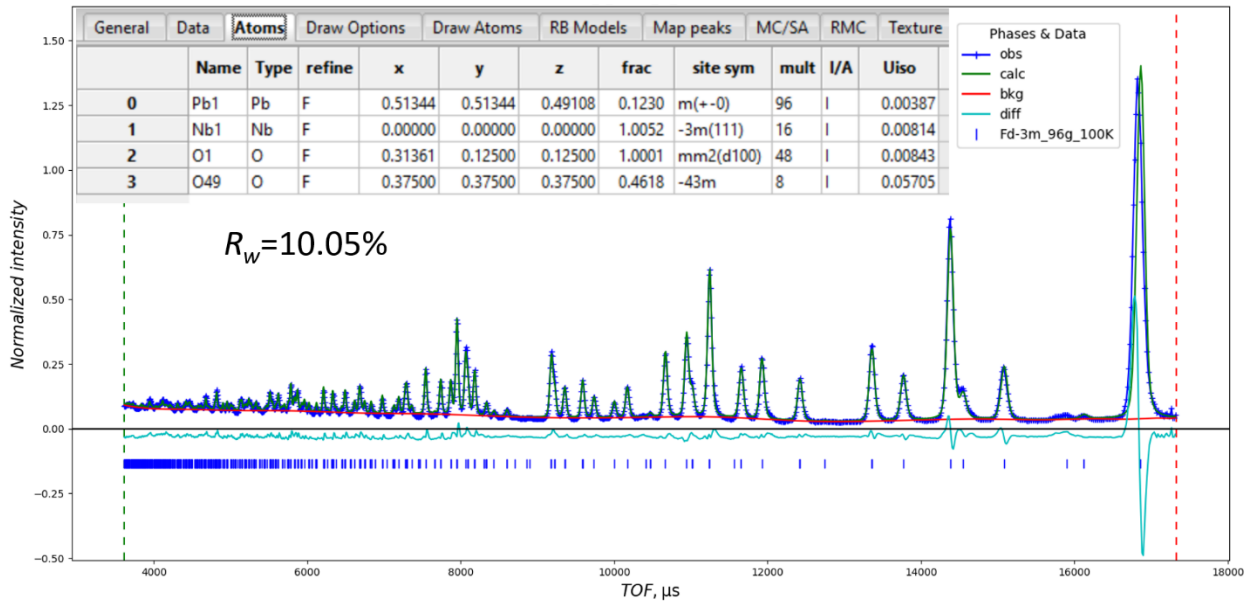

Figure 5-13: Rietveld fit of neutron diffraction data against the cubic $Fd\bar{3}m$ 96g model at 100 K using bank 4 (resulting R_w = 10.05%).

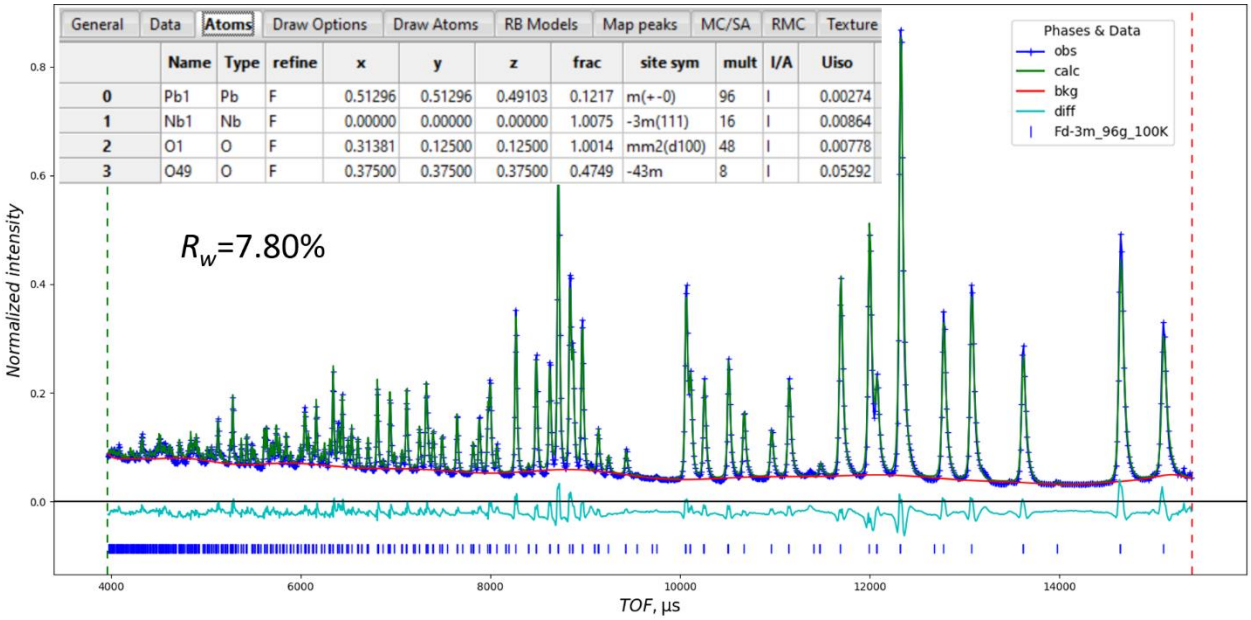

Figure 5-14: Rietveld fit of neutron diffraction data against the cubic $Fd\bar{3}m$ 96g model at 100 K using bank 5 (resulting R_w = 7.80%).

Figures 5-9 to 5-14 show the Rietveld fit of diffraction data against the cubic $Fd\bar{3}m$ 96g model at 300 K, 200 K, and 100 K using banks 4 and 5. The summary of these refinements is reported in Figures 5-15 and 5-16 with banks 4 and 5, respectively. Similar to the Rietveld fit of neutron data against the $Fd\bar{3}m$ 16d, the cubic $Fd\bar{3}m$ 96g is also best fit at 300 K and gets worse upon cooling.

NOMAD Cubic Yellow at 300K_Bank 4_Fd-3m_96g R_w=8.91%

General | Data | Atoms | Draw Options | Draw Atoms | RB Models | Map peaks | MC/SA | RMC | Texture

	Name	Type	refine	x	y	z	frac	site sym	mult	I/A	Uiso
0	Pb1	Pb	F	0.51457	0.51457	0.49095	0.1229	m(+-0)	96	I	0.00688
1	Nb1	Nb	F	0.00000	0.00000	0.00000	1.0048	-3m(111)	16	I	0.01142
2	O1	O	F	0.31331	0.12500	0.12500	1.0004	mm2(d100)	48	I	0.01213
3	O49	O	F	0.37500	0.37500	0.37500	0.4662	-43m	8	I	0.05740

NOMAD Cubic Yellow at 200K_Bank 4_Fd-3m_96g R_w=10.25%

General | Data | Atoms | Draw Options | Draw Atoms | RB Models | Map peaks | MC/SA | RMC | Texture

	Name	Type	refine	x	y	z	frac	site sym	mult	I/A	Uiso
0	Pb1	Pb	F	0.51373	0.51373	0.49117	0.1228	m(+-0)	96	I	0.00595
1	Nb1	Nb	F	0.00000	0.00000	0.00000	1.0036	-3m(111)	16	I	0.01042
2	O1	O	F	0.31371	0.12500	0.12500	1.0015	mm2(d100)	48	I	0.01037
3	O49	O	F	0.37500	0.37500	0.37500	0.4603	-43m	8	I	0.06432

NOMAD Cubic Yellow at 100K_Bank 4_Fd-3m_96g R_w=10.05%

General | Data | Atoms | Draw Options | Draw Atoms | RB Models | Map peaks | MC/SA | RMC | Texture

	Name	Type	refine	x	y	z	frac	site sym	mult	I/A	Uiso
0	Pb1	Pb	F	0.51344	0.51344	0.49108	0.1230	m(+-0)	96	I	0.00387
1	Nb1	Nb	F	0.00000	0.00000	0.00000	1.0052	-3m(111)	16	I	0.00814
2	O1	O	F	0.31361	0.12500	0.12500	1.0001	mm2(d100)	48	I	0.00843
3	O49	O	F	0.37500	0.37500	0.37500	0.4618	-43m	8	I	0.05705

Figure 5-15: Refined crystallographic data of cubic Fd$\bar{3}$m 96g at 100 K, 200 K, and 300 K from bank 4.

NOMAD Cubic Yellow at 300K_Bank 5_Fd-3m_96g R_w=7.25%

General | Data | Atoms | Draw Options | Draw Atoms | RB Models | Map peaks | MC/SA | RMC | Texture

	Name	Type	refine	x	y	z	frac	site sym	mult	I/A	Uiso
0	Pb1	Pb	F	0.51390	0.51390	0.49045	0.1218	m(+-0)	96	I	0.00686
1	Nb1	Nb	F	0.00000	0.00000	0.00000	1.0041	-3m(111)	16	I	0.01138
2	O1	O	F	0.31369	0.12500	0.12500	1.0018	mm2(d100)	48	I	0.01131
3	O49	O	F	0.37500	0.37500	0.37500	0.4747	-43m	8	I	0.05571

NOMAD Cubic Yellow at 200K_Bank 5_Fd-3m_96g R_w=7.52%

General | Data | Atoms | Draw Options | Draw Atoms | RB Models | Map peaks | MC/SA | RMC | Texture

	Name	Type	refine	x	y	z	frac	site sym	mult	I/A	Uiso
0	Pb1	Pb	F	0.51331	0.51331	0.49063	0.1215	m(+-0)	96	I	0.00510
1	Nb1	Nb	F	0.00000	0.00000	0.00000	1.0076	-3m(111)	16	I	0.01007
2	O1	O	F	0.31375	0.12500	0.12500	1.0013	mm2(d100)	48	I	0.00964
3	O49	O	F	0.37500	0.37500	0.37500	0.4744	-43m	8	I	0.05545

NOMAD Cubic Yellow at 100K_Bank 5_Fd-3m_96g R_w=7.80%

General | Data | Atoms | Draw Options | Draw Atoms | RB Models | Map peaks | MC/SA | RMC | Texture

	Name	Type	refine	x	y	z	frac	site sym	mult	I/A	Uiso
0	Pb1	Pb	F	0.51296	0.51296	0.49103	0.1217	m(+-0)	96	I	0.00274
1	Nb1	Nb	F	0.00000	0.00000	0.00000	1.0075	-3m(111)	16	I	0.00864
2	O1	O	F	0.31381	0.12500	0.12500	1.0014	mm2(d100)	48	I	0.00778
3	O49	O	F	0.37500	0.37500	0.37500	0.4749	-43m	8	I	0.05292

Figure 5-16: Refined crystallographic data of cubic $Fd\bar{3}m$ 96g at 100 K, 200 K, and 300 K from bank 5.

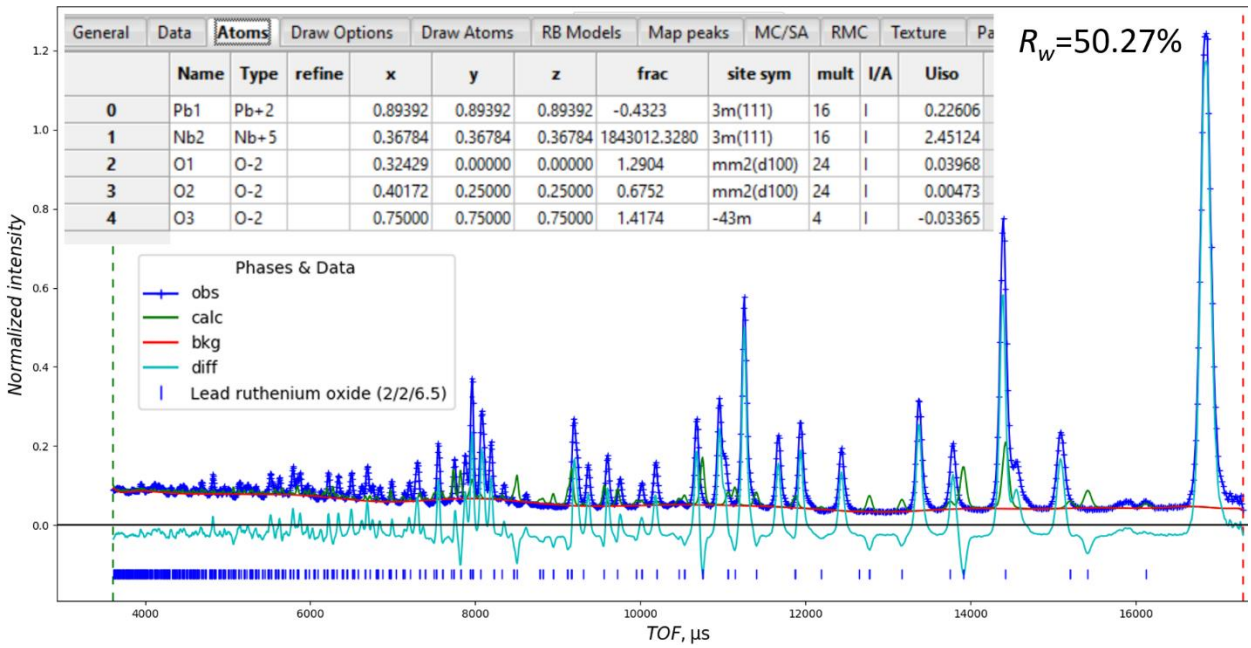

Figure 5-17: Rietveld fit of neutron diffraction data against the F$\bar{4}3m$ model at 300 K using bank 4 (resulting R_w = 50.27%).

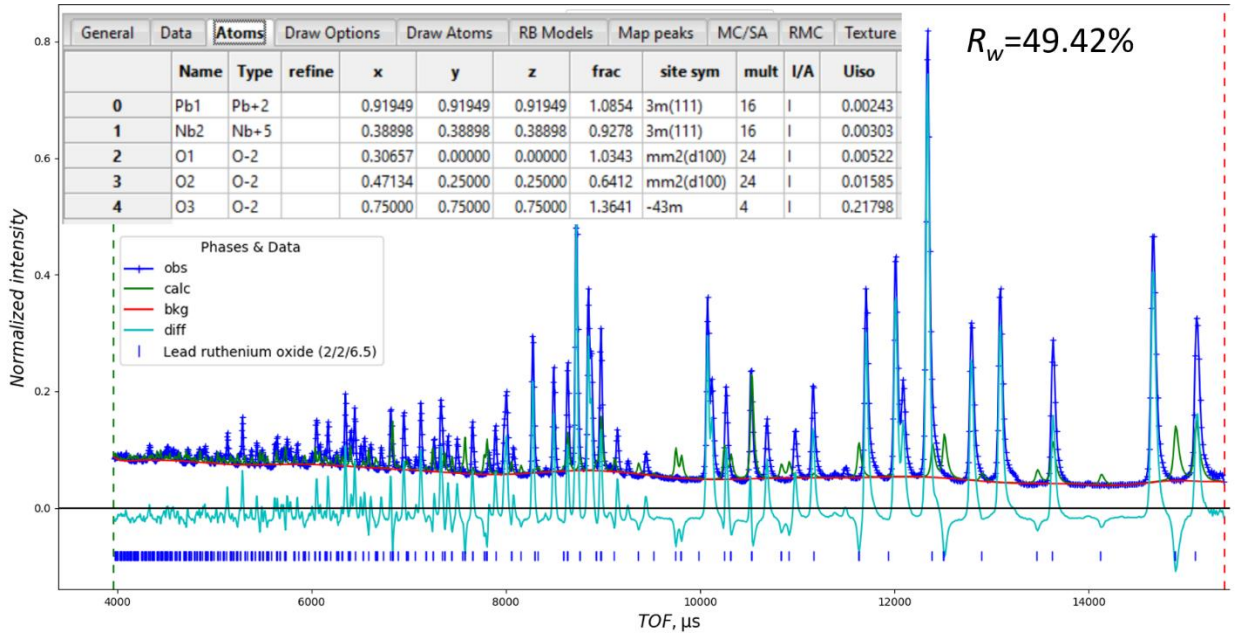

Figure 5-18: Rietveld fit of neutron diffraction data against the F$\bar{4}3m$ model at 300 K using bank 5 (resulting R_w = 49.42%).

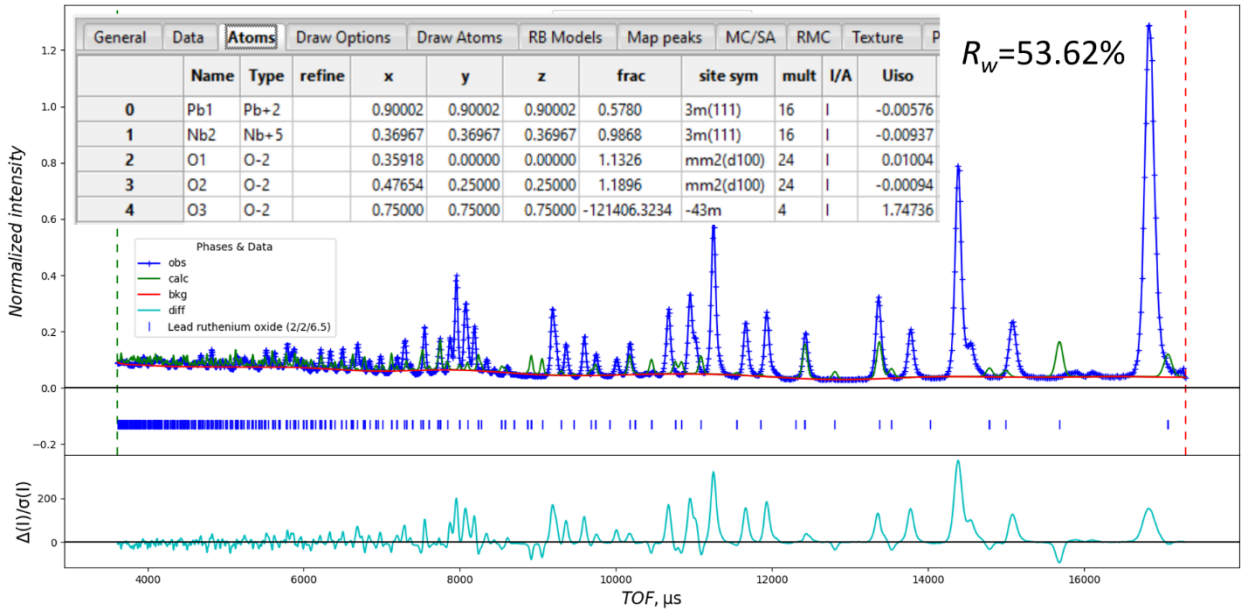

Figure 5-19: Rietveld fit of neutron diffraction data against the F$\bar{4}3m$ model at 200 K using bank 4 (resulting R_w = 53.62%).

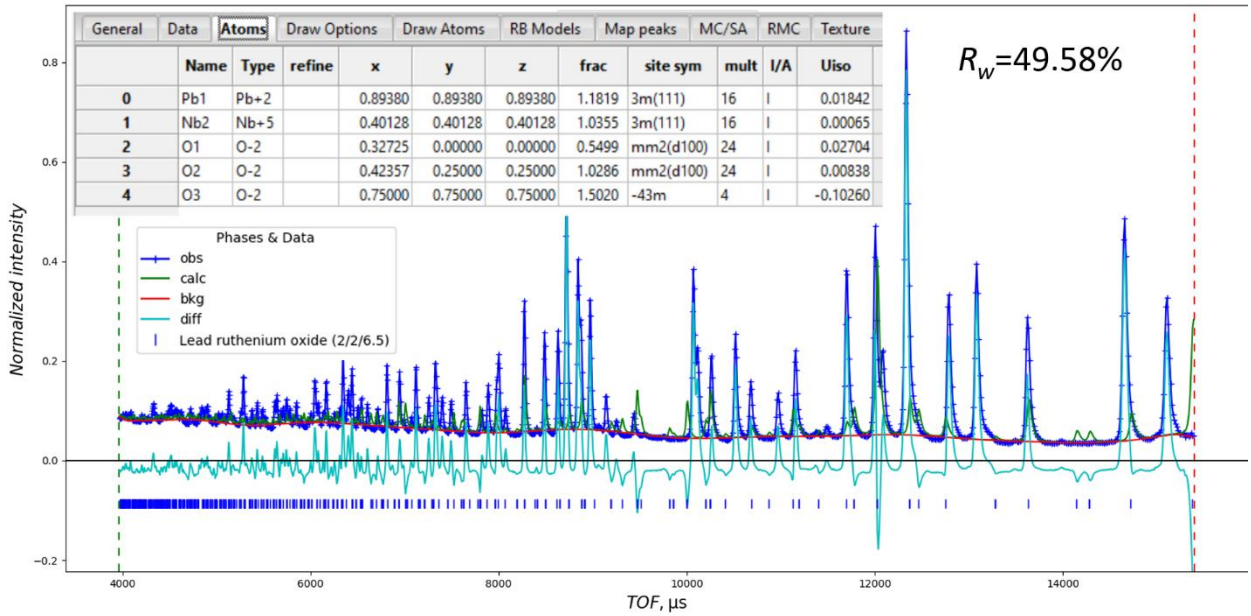

Figure 5-20: Rietveld fit of neutron diffraction data against the F$\bar{4}3m$ model at 200 K using bank 5 (resulting R_w = 49.58%).

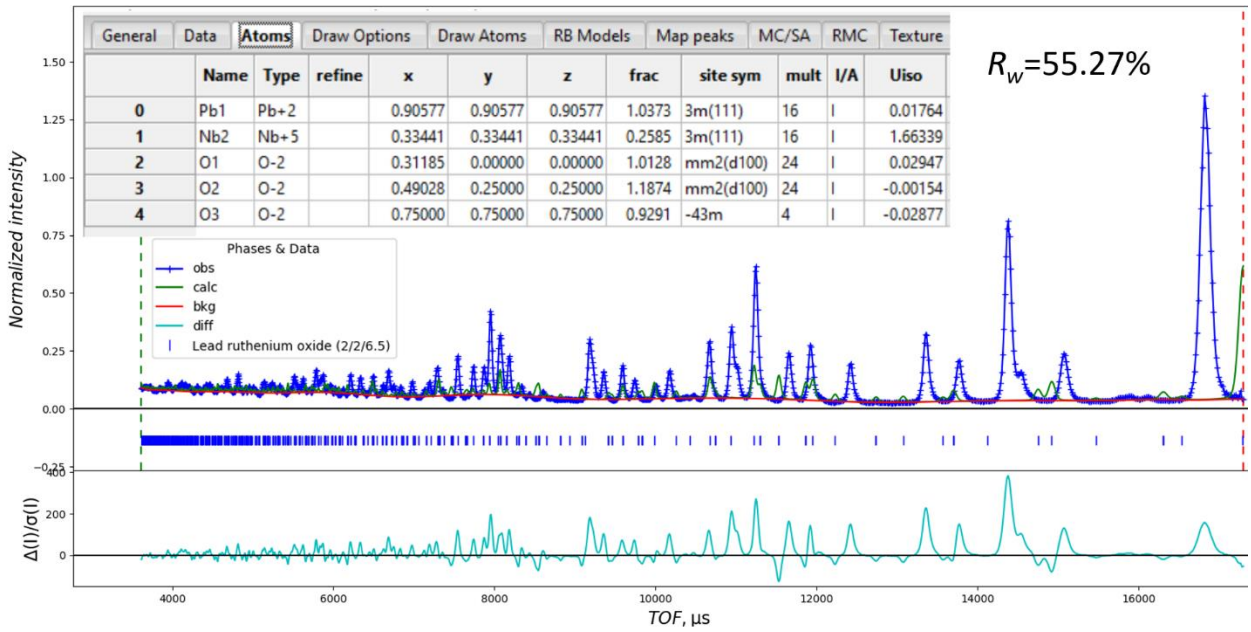

Figure 5-21: Rietveld fit of neutron diffraction data against the $F\bar{4}3m$ model at 100 K using bank 4 (resulting R_w = 55.27%).

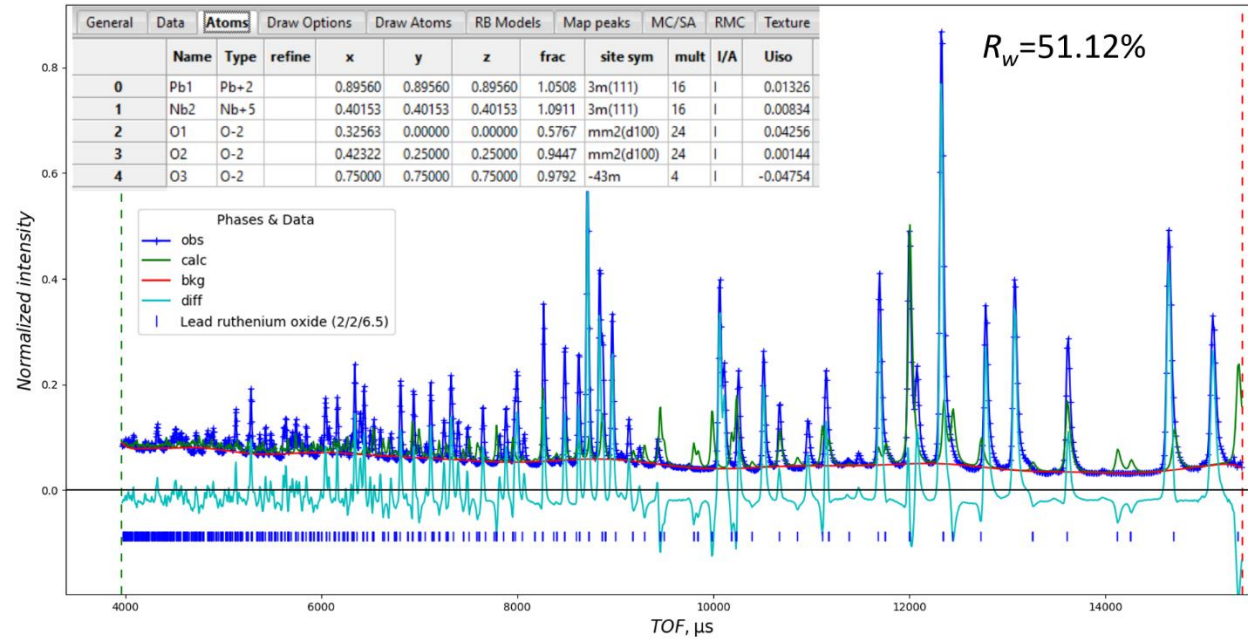

Figure 5-22: Rietveld fit of neutron diffraction data against the $F\bar{4}3m$ model at 100 K using bank 5 (resulting R_w = 51.12%).

Figures 5-17 to 5-22 show the Rietveld fit of diffraction data against the $F\bar{4}3m$ model at 300 K, 200 K, and 100 K using banks 4 and 5. The summary of these refinements is reported in Figures 5-23 and 5-24 with banks 4 and 5, respectively. Based on the R_w values, the $F\bar{4}3m$ model does not fit to the data at all temperatures. Therefore, our data cannot be described by this model.

NOMAD Cubic Yellow at 300K_Bank 4_F-43m R_w=50.27%

General | Data | **Atoms** | Draw Options | Draw Atoms | RB Models | Map peaks | MC/SA | RMC | Texture | Pa

	Name	Type	refine	x	y	z	frac	site sym	mult	I/A	Uiso
0	Pb1	Pb+2		0.89392	0.89392	0.89392	-0.4323	3m(111)	16	I	0.22606
1	Nb2	Nb+5		0.36784	0.36784	0.36784	1843012.3280	3m(111)	16	I	2.45124
2	O1	O-2		0.32429	0.00000	0.00000	1.2904	mm2(d100)	24	I	0.03968
3	O2	O-2		0.40172	0.25000	0.25000	0.6752	mm2(d100)	24	I	0.00473
4	O3	O-2		0.75000	0.75000	0.75000	1.4174	-43m	4	I	-0.03365

NOMAD Cubic Yellow at 200K_Bank4 _F-43m R_w=53.62%

General | Data | **Atoms** | Draw Options | Draw Atoms | RB Models | Map peaks | MC/SA | RMC | Texture | P

	Name	Type	refine	x	y	z	frac	site sym	mult	I/A	Uiso
0	Pb1	Pb+2		0.90002	0.90002	0.90002	0.5780	3m(111)	16	I	-0.00576
1	Nb2	Nb+5		0.36967	0.36967	0.36967	0.9868	3m(111)	16	I	-0.00937
2	O1	O-2		0.35918	0.00000	0.00000	1.1326	mm2(d100)	24	I	0.01004
3	O2	O-2		0.47654	0.25000	0.25000	1.1896	mm2(d100)	24	I	-0.00094
4	O3	O-2		0.75000	0.75000	0.75000	-121406.3234	-43m	4	I	1.74736

NOMAD Cubic Yellow at 100K_Bank4 _F-43m R_w=55.27%

General | Data | **Atoms** | Draw Options | Draw Atoms | RB Models | Map peaks | MC/SA | RMC | Texture

	Name	Type	refine	x	y	z	frac	site sym	mult	I/A	Uiso
0	Pb1	Pb+2		0.90577	0.90577	0.90577	1.0373	3m(111)	16	I	0.01764
1	Nb2	Nb+5		0.33441	0.33441	0.33441	0.2585	3m(111)	16	I	1.66339
2	O1	O-2		0.31185	0.00000	0.00000	1.0128	mm2(d100)	24	I	0.02947
3	O2	O-2		0.49028	0.25000	0.25000	1.1874	mm2(d100)	24	I	-0.00154
4	O3	O-2		0.75000	0.75000	0.75000	0.9291	-43m	4	I	-0.02877

Figure 5-23: Refined crystallographic data of F$\bar{4}3m$ at 100 K, 200 K, and 300 K from bank 4.

NOMAD Cubic Yellow at 300K_Bank 5_F-43m R_w =49.42%

General | Data | **Atoms** | Draw Options | Draw Atoms | RB Models | Map peaks | MC/SA | RMC | Texture

	Name	Type	refine	x	y	z	frac	site sym	mult	I/A	Uiso
0	Pb1	Pb+2		0.91949	0.91949	0.91949	1.0854	3m(111)	16	I	0.00243
1	Nb2	Nb+5		0.38898	0.38898	0.38898	0.9278	3m(111)	16	I	0.00303
2	O1	O-2		0.30657	0.00000	0.00000	1.0343	mm2(d100)	24	I	0.00522
3	O2	O-2		0.47134	0.25000	0.25000	0.6412	mm2(d100)	24	I	0.01585
4	O3	O-2		0.75000	0.75000	0.75000	1.3641	-43m	4	I	0.21798

NOMAD Cubic Yellow at 200K_Bank 5_F-43m R_w =49.58%

General | Data | **Atoms** | Draw Options | Draw Atoms | RB Models | Map peaks | MC/SA | RMC | Texture

	Name	Type	refine	x	y	z	frac	site sym	mult	I/A	Uiso
0	Pb1	Pb+2		0.89380	0.89380	0.89380	1.1819	3m(111)	16	I	0.01842
1	Nb2	Nb+5		0.40128	0.40128	0.40128	1.0355	3m(111)	16	I	0.00065
2	O1	O-2		0.32725	0.00000	0.00000	0.5499	mm2(d100)	24	I	0.02704
3	O2	O-2		0.42357	0.25000	0.25000	1.0286	mm2(d100)	24	I	0.00838
4	O3	O-2		0.75000	0.75000	0.75000	1.5020	-43m	4	I	-0.10260

NOMAD Cubic Yellow at 100K_Bank 5_F-43m R_w =51.12%

General | Data | **Atoms** | Draw Options | Draw Atoms | RB Models | Map peaks | MC/SA | RMC | Texture

	Name	Type	refine	x	y	z	frac	site sym	mult	I/A	Uiso
0	Pb1	Pb+2		0.89560	0.89560	0.89560	1.0508	3m(111)	16	I	0.01326
1	Nb2	Nb+5		0.40153	0.40153	0.40153	1.0911	3m(111)	16	I	0.00834
2	O1	O-2		0.32563	0.00000	0.00000	0.5767	mm2(d100)	24	I	0.04256
3	O2	O-2		0.42322	0.25000	0.25000	0.9447	mm2(d100)	24	I	0.00144
4	O3	O-2		0.75000	0.75000	0.75000	0.9792	-43m	4	I	-0.04754

Figure 5-24: Refined crystallographic data of $F\bar{4}3m$ at 100 K, 200 K, and 300 K from bank 5.

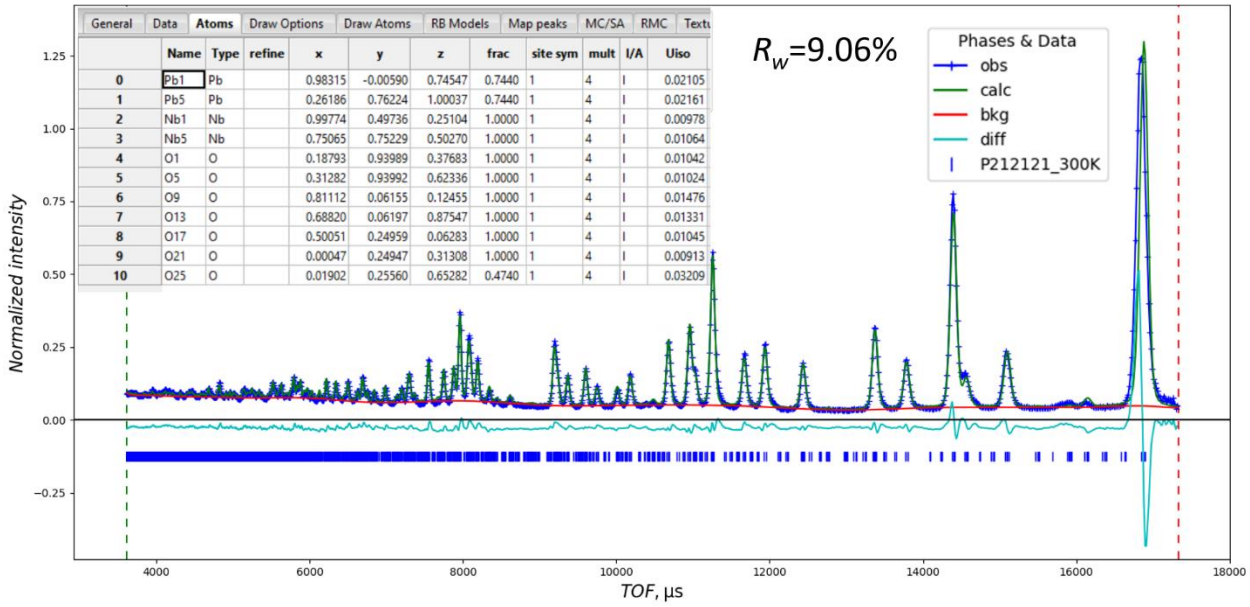

Figure 5-25: Rietveld fit of neutron diffraction data against the cristobalite $P2_12_12_1$ model at 300 K using bank 4 (resulting R_w = 9.06%).

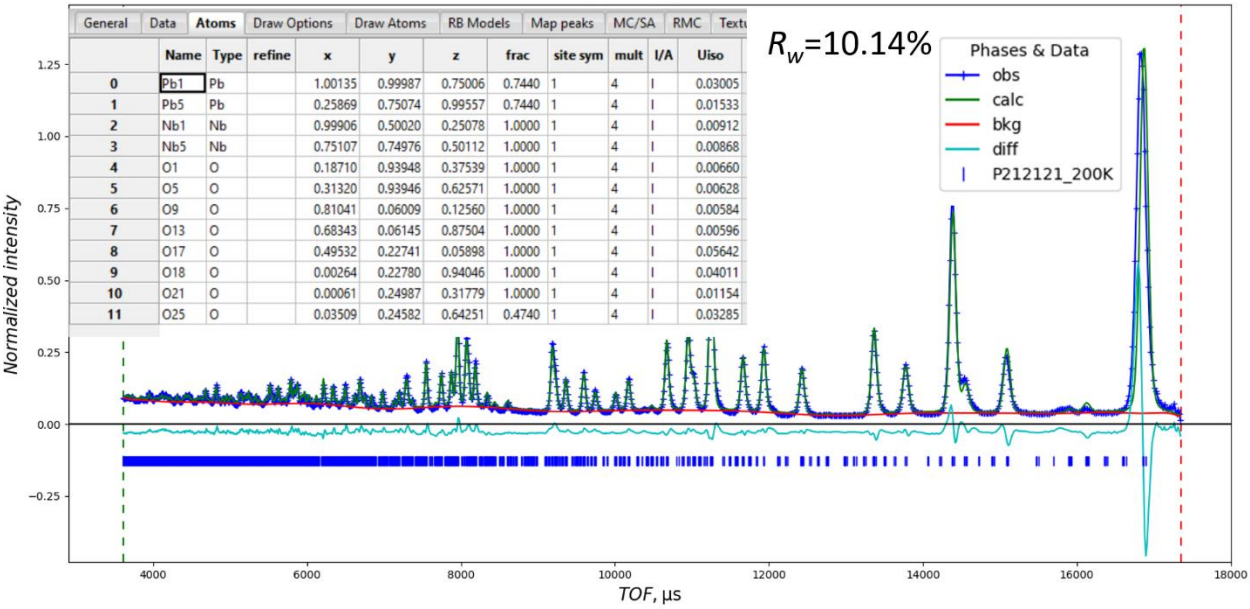

Figure 5-26: Rietveld fit of neutron diffraction data against the cristobalite $P2_12_12_1$ model at 200 K using bank 4 (resulting R_w = 10.14%).

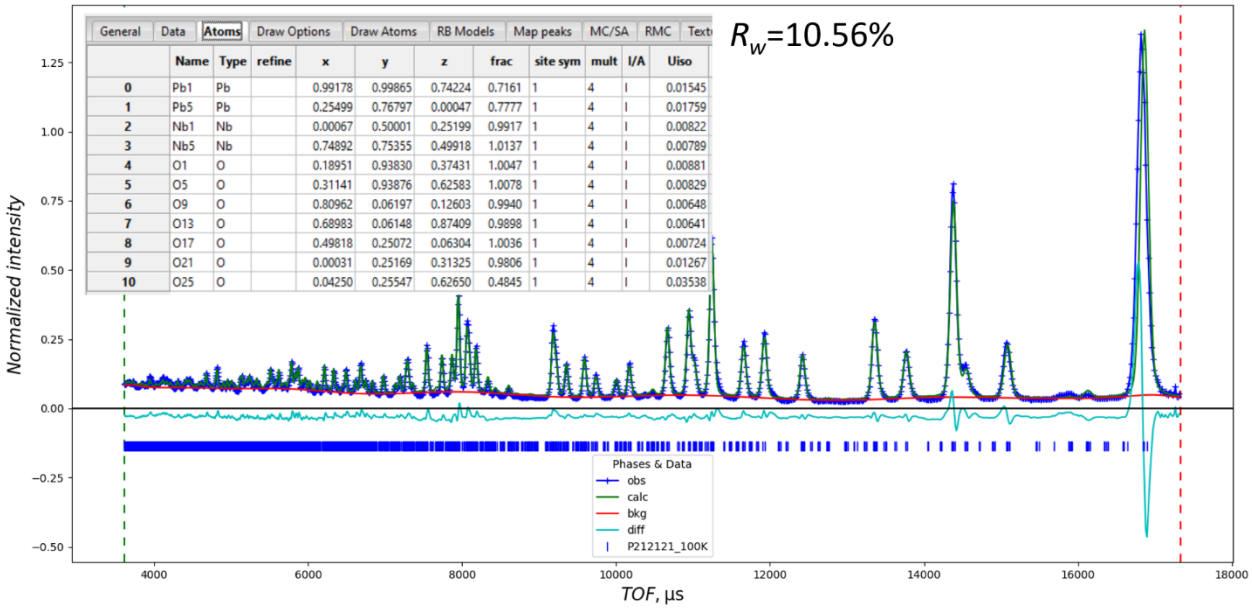

Figure 5-27: Rietveld fit of neutron diffraction data against the cristobalite $P2_12_12_1$ model at 100 K using bank 4 (resulting R_w = 10.56%).

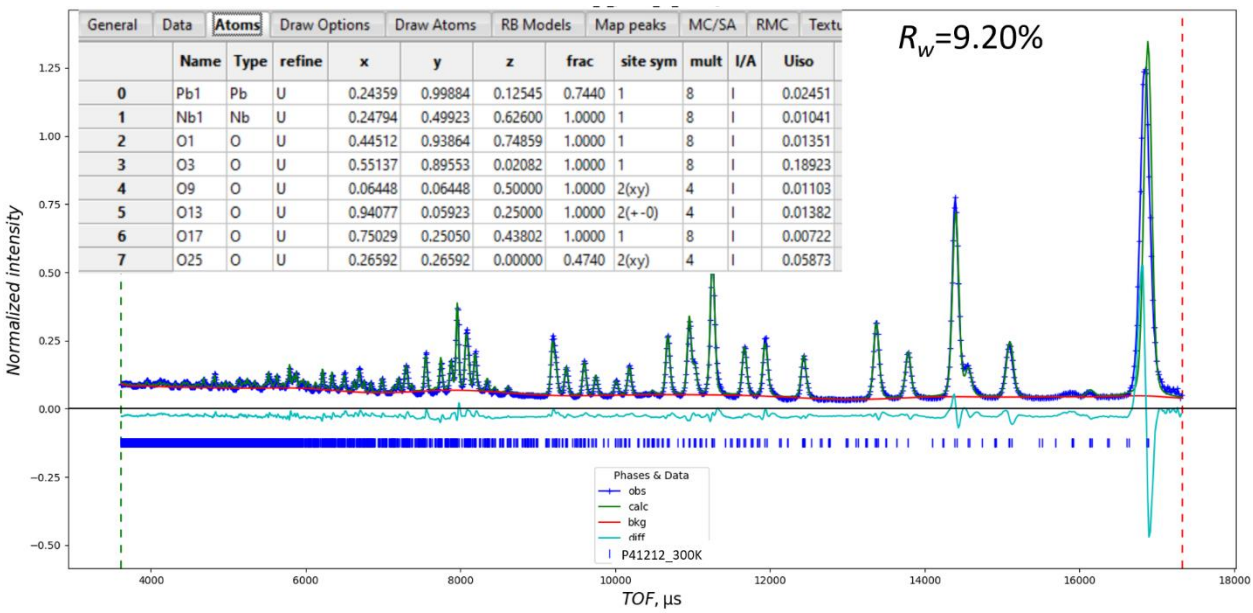

Figure 5-28: Rietveld fit of neutron diffraction data against the cristobalite $P4_12_12$ model at 300 K using bank 4 (resulting R_w = 9.20%).

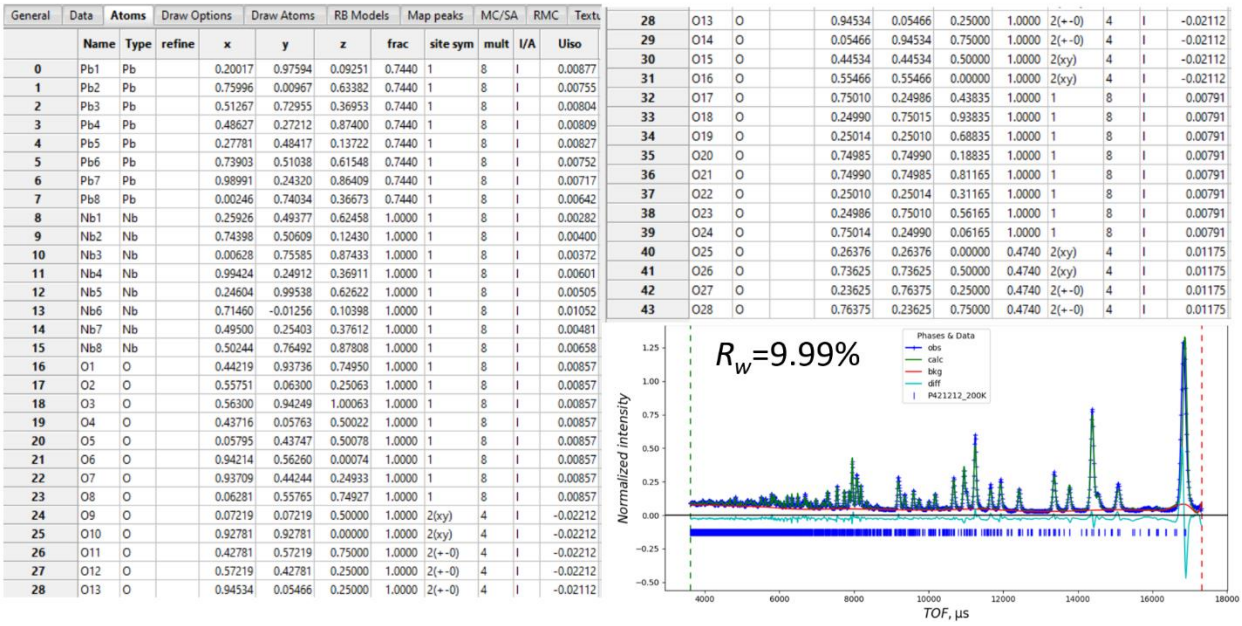

Figure 5-29: Rietveld fit of neutron diffraction data against the cristobalite $P4_12_12$ model at 200 K using bank 4 (resulting R_w = 9.99%).

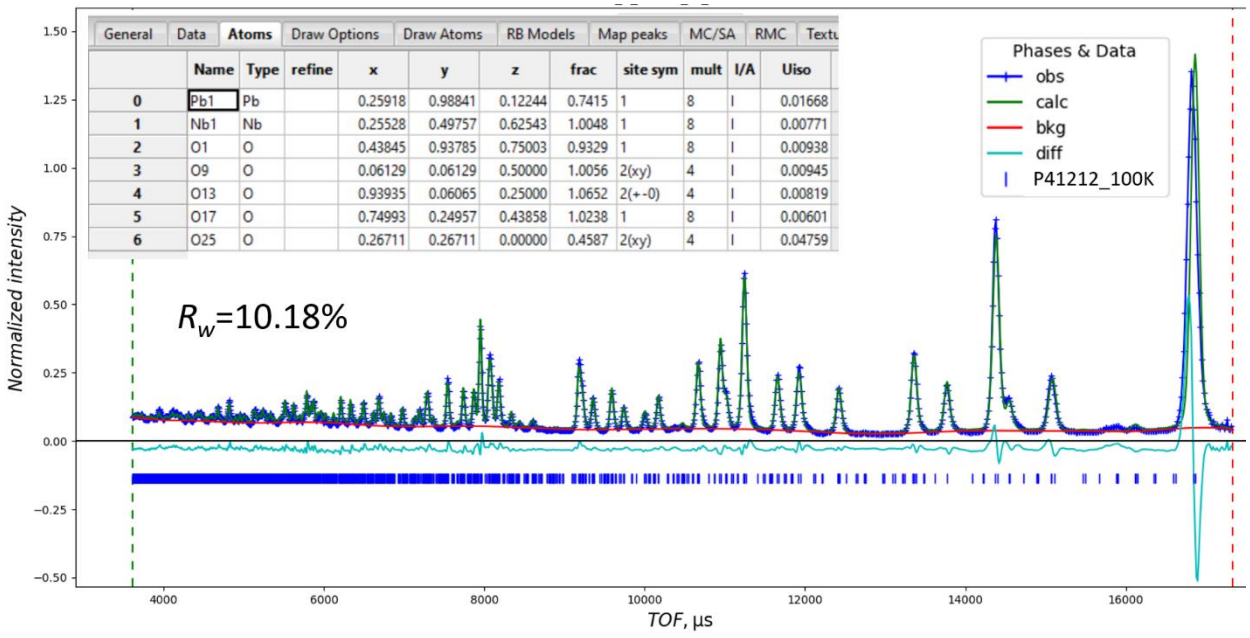

Figure 5-30: Rietveld fit of neutron diffraction data against the cristobalite $P4_12_12$ model at 100 K using bank 4 (resulting R_w = 10.18%).

Figures 5-25 to 5-27 and 5-31to 5-33 show the Rietveld fit of diffraction data against the cristobalite $P2_12_12_1$ at 300 K, 200 K, and 100 K using banks 4 and 5, respectively. The data is best fit at 300 K when using bank 5 and get worse upon cooling for both banks.

Figure 5-28 to 5-30 and 5-34 to 5-36 show the Rietveld fit of diffraction data against the cristobalite $P4_12_12$ at 300 K, 200 K, and 100 K using banks 4 and 5, respectively. The data is best fit at 300 K when using bank 4 and get worse upon cooling for both banks.

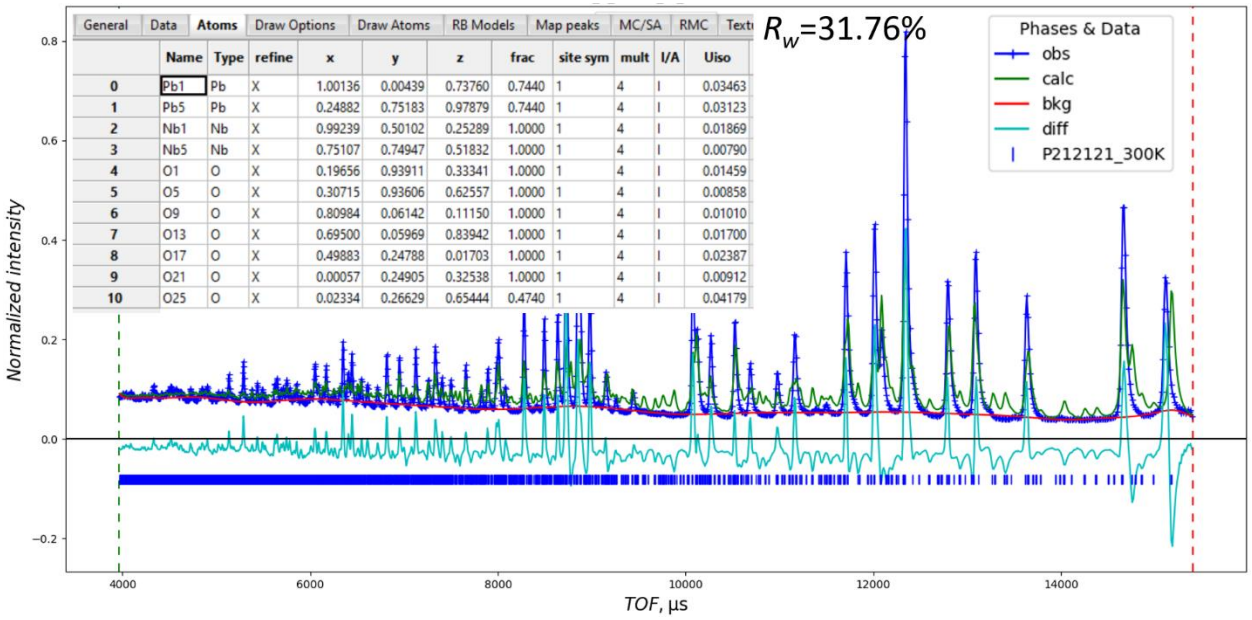

Figure 5-31: Rietveld fit of neutron diffraction data against the cristobalite $P2_12_12_1$ model at 300 K using bank 5 (resulting R_w = 31.76%).

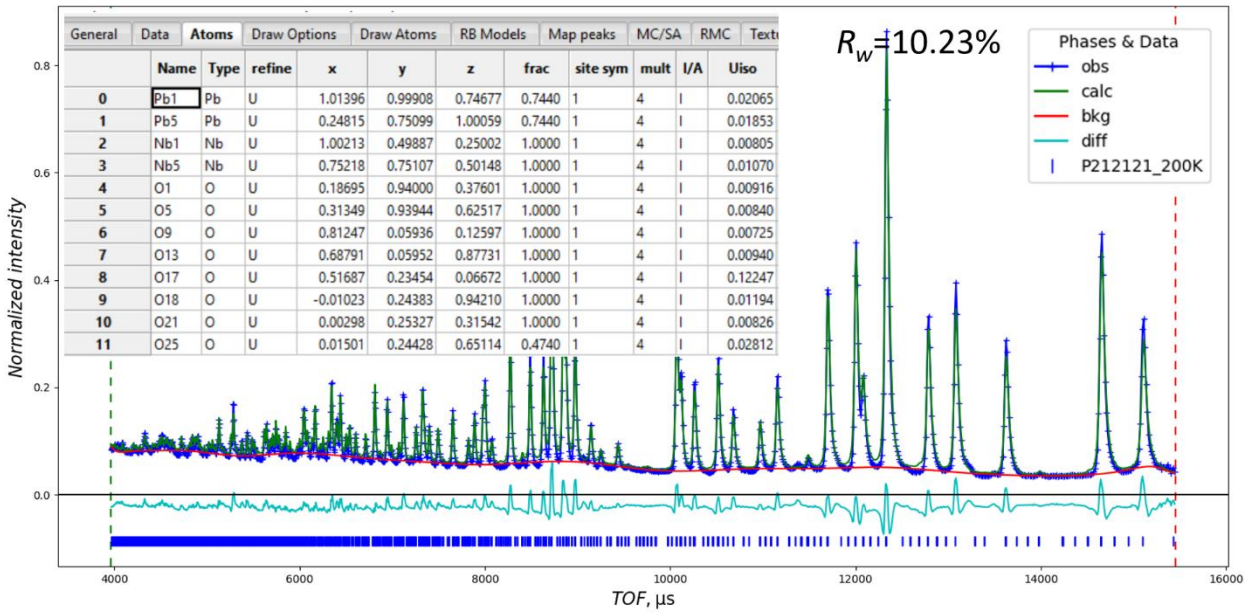

Figure 5-32: Rietveld fit of neutron diffraction data against the cristobalite $P2_12_12_1$ model at 200 K using bank 5 (resulting R_w = 10.23%).

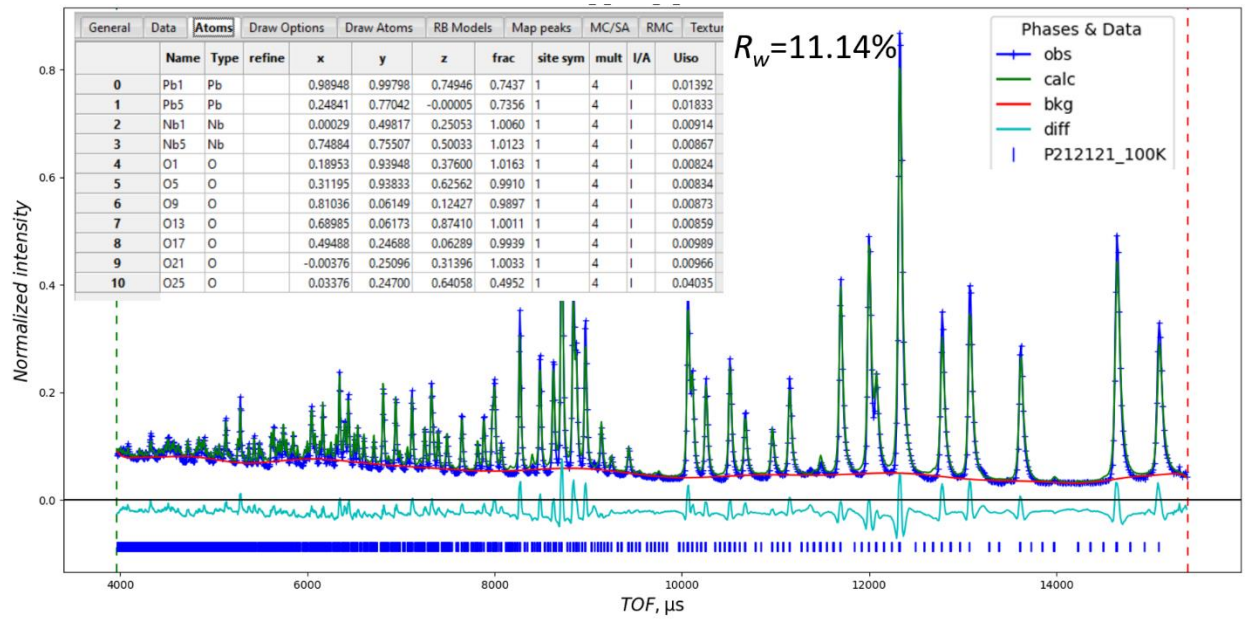

Figure 5-33: Rietveld fit of neutron diffraction data against the cristobalite $P2_12_12_1$ model at 100 K using bank 5 (resulting R_w = 11.14%).

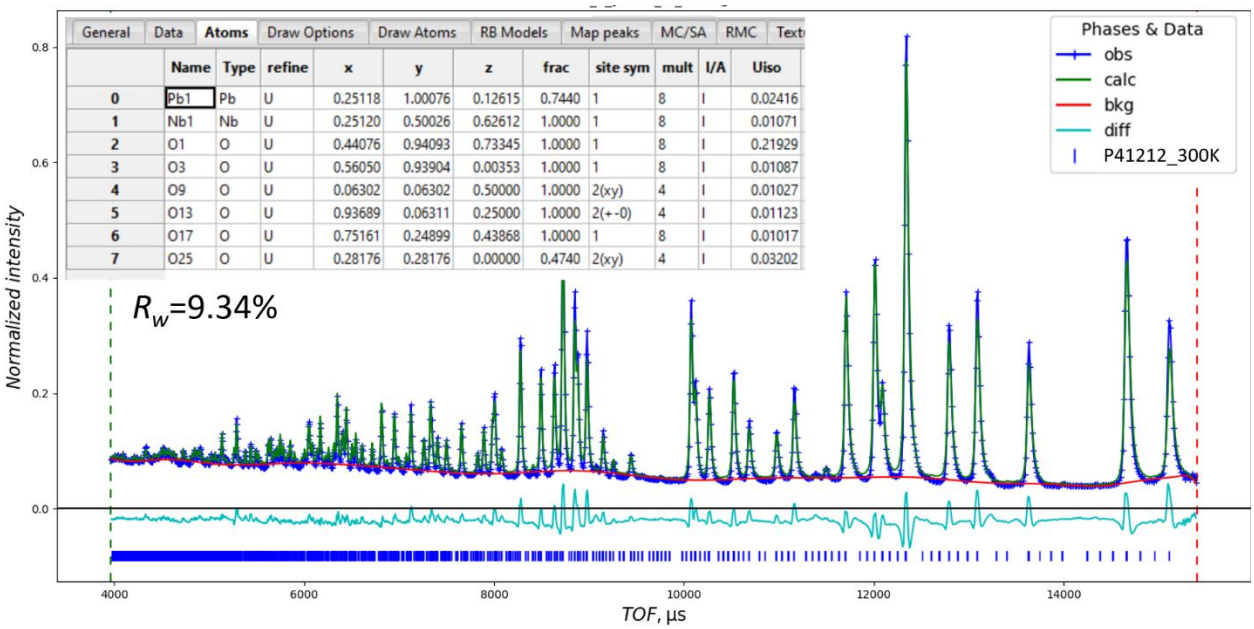

Figure 5-34: Rietveld fit of neutron diffraction data against the cristobalite $P4_12_12$ model at 300 K using bank 5 (resulting R_w = 9.34%).

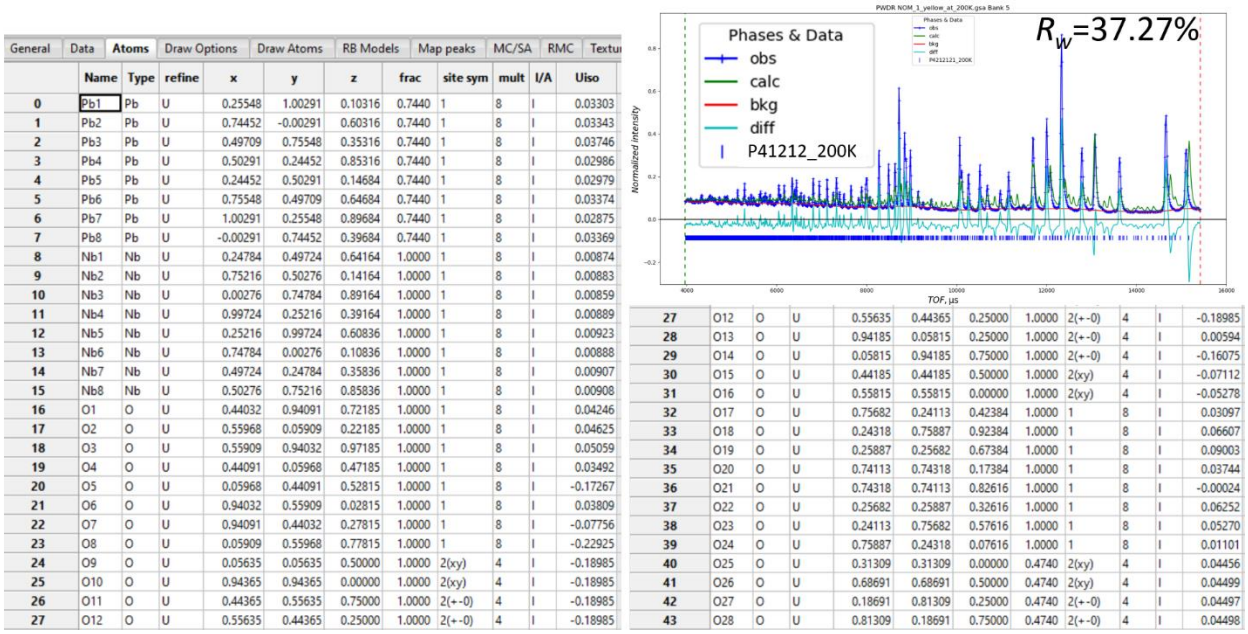

Figure 5-35: Rietveld fit of neutron diffraction data against the cristobalite $P4_12_12$ model at 200 K using bank 5 (resulting R_w = 37.27%).

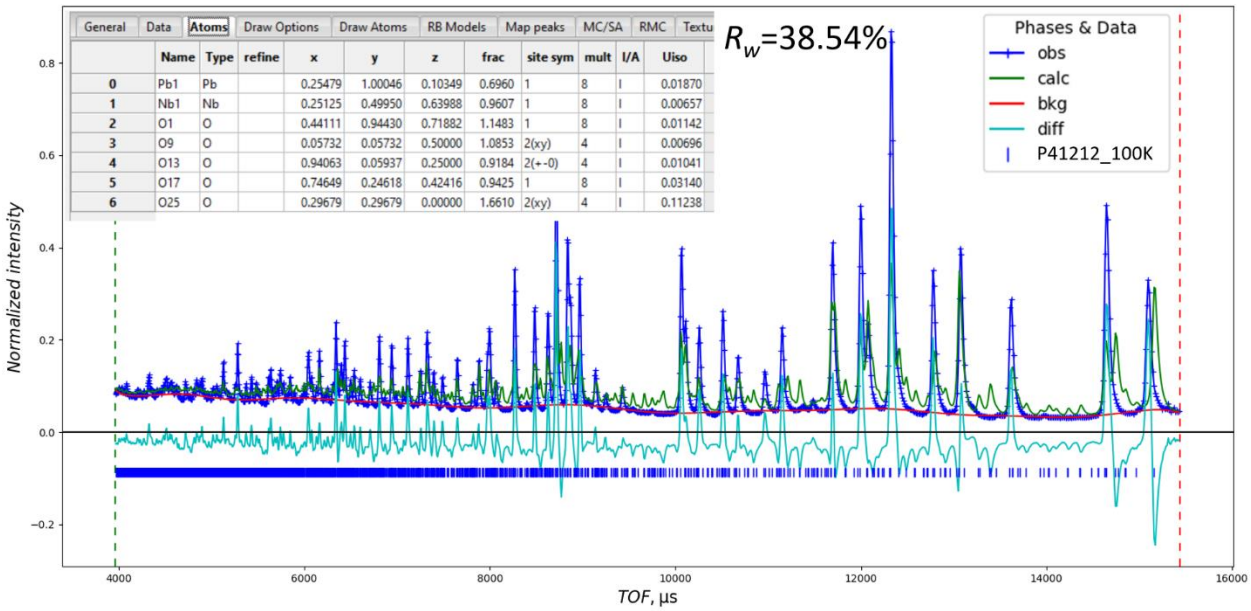

Figure 5-36: Rietveld fit of neutron diffraction data against the cristobalite $P4_12_12$ model at 100 K using bank 5 (resulting R_w = 38.54%).

Rietveld refinement results show that average structure is best described by $Fd\bar{3}m$ 16d model 300 K and gets worse upon cooling among all models. The data is also described well with cristobalite structure at 300 K and get worse upon cooling. The fit gets worse with temperatures indicating that the cubic model might not be best descriptor at low temperature. This does agree with what we were seeing in the PDF data at 30 Å (long-range order). Based on PDF R_w values, the cristobalite models show best fit at lower temperatures as at long-range order. Therefore, an outstanding question is a presence of phase transition or is this reflecting that disorder?

Table 5- 1: Goodness-of-fit parameters R_w of the various local models at 100 K, 200 K, and 300 K.

	Temperature	$Fd\bar{3}m$ 16d	$Fd\bar{3}m$ 96g	$P2_12_12_1$	$P4_12_12$
Bank 4	300 K	8.32	8.92	9.06	9.2
	200 K	9.58	10.26	10.14	9.99
	100 K	9.92	10.05	10.57	10.18
Bank 5	300 K	6.97	7.27	31.76	9.34
	200 K	7.53	7.54	10.23	37.27
	100 K	8.23	7.82	11.42	38.54

Chapter 6 General Summary

In this work, we focused the role of stereochemically active lone pair in the Pb $6s^2$ on the crystal structure and physical properties in the Pb-containing solid-state materials. The structural characterization was studied using total elastic scattering where both Bragg and diffuse scattering of diffraction patterns are analyzed by Rietveld and pair distribution function techniques, respectively.

Chapter 1 describes the classical and revised lone pair models to explain lone pairs of electrons, their interactions and their influence on structural distortions

Chapter 2 focuses on the fundamentals of structural characterization of materials including powder X-ray diffraction, Rietveld refinement and atomic pair distribution function.

Chapters 3 describes the study of the lone pair-driven thermochromic behavior in oxychloride $PbVO_3Cl$. $BaVO_3Cl$, which does not contain stereochemically active lone pair, is used as a control. Local structure details of $PbVO_3Cl$ and $BaVO_3Cl$ were studied via X-ray and neutron diffraction pair distribution function. X-ray photoelectron spectroscopy measurements were employed to probe the evidence of the presence of the $6s^2$ lone pair at the valence band maximum, which are corroborated by first-principles calculations.

Chapter 4 describes the study of the vacancy-driven disordered and elevated dielectric response in the defect pyrochlore $Pb_{1.5}Nb_2O_{6.5}$. Local distortions are presented by comparing two models of correlated distortion at all temperature using X-ray and neutron diffraction pair distribution function analysis. The structural transition upon cooling and the structural influence on physical properties were investigated by heat capacity and dielectric permittivity measurements.

Chapter 5 reports the Rietveld refinement results of neutron diffraction data on the cubic pyrochlore $Fd\bar{3}m$ against different models at 100K, 200K, and 300K in $Pb_{1.5}Nb_2O_{6.5}$ using the GSAS-II software.

Appendix A Publication Information and Contributing Authors

Chapter 3: A manuscript published in journal of Chemistry of Materials. U. Dang, W. Zaheer, W. Zhou, A. Kandel, M. Orr, R. W. Schwenz, G. Laurita, S. Banerjee, and R. T. Macaluso. **2020**, *32,* 17, 7404-7412.

Chapter 4: A manuscript published in journal of Inorganic Chemistry. U. Dang, J. O'Hara, H. A. Evans, D. Olds, J. Chamorro, D. Hickox-Young, G. Laurita, and R. T. Macaluso.

Publication Date: November 8, 2022.

DOI: 10.1021/acs.inorgchem.2c03031

Appendix B Supporting Information

Table 3-S1: Refinement results from powder X-ray diffraction of PbVO3Cl and BaVO3Cl

	$PbVO_3Cl$	**$BaVO_3Cl$**	
		$BaVO_3Cl$	**BaV_2O6**
Weight fraction (%)	100	93.7	6.3
Space group (No.)	*Pnma* (62)	*Pnma* (62)	*C222* (21)
Crystal system	Orthorhombic	Orthorhombic	Orthorhombic
a (Å)	10.05000(5)	10.46226(8)	8.4793(3)
b (Å)	5.28646(7)	5.28578(5)	12.6061(6)
c (Å)	7.18302(5)	7.35569(6)	7.9126(4)
α (°)	90	90	90
β (°)	90	90	90
γ (°)	90	90	90
GOF	1.80	1.71	
Rwp (%)	16.150	8.230	
Rp (%)	12.120	5.944	

Table 3-S 2: Refined Atomic Positions and Occupancies Obtained from Powder X-ray Diffraction for PbVO3Cl and BaVO3Cl

$PbVO_3Cl$					
	x	***y***	***z***	**U_{iso} (Å^2)**	**Occupancy**
Pb	0.17094(5)	¼	0.38505(9)	0.0254(1)	1
V	0.5285(2)	¼	0.5676(3)	0.0111(7)	1
O(1)	0.0934(4)	-0.006(1)	0.1143(8)	0.003(2)	1
O(2)	0.1359(6)	¼	0.775(1)	0.000(2)	1
Cl	0.3929(3)	¼	0.0556(5)	0.022(1)	1
$BaVO_3Cl$					
	x	***y***	***z***	**U_{iso} (Å^2)**	**Occupancy**
Ba	0.19519(7)	¼	0.1002(1)	0.0074(2)	1
V	-0.0428(2)	¼	0.4519(2)	0.0094(6)	1
O(1)	0.0946(3)	0.5074(7)	0.4093(6)	0.009(2)	1
O(2)	0.3544(5)	¾	0.2130(8)	0.010(3)	1
Cl	0.3934(2)	¼	0.4305(4)	0.0068(9)	1
BaV_2O_6					
	x	***y***	***z***	**U_{iso} (Å^2)**	**Occupancy**
Ba(1)	0.000000	0.000000	0.000000	0.0063	1
Ba(2)	0.000000	0.1660(7)	½	0.0063	1
V(1)	0.178(2)	0.549(2)	0.256(3)	0.0063	1
V(2)	¼	¼	0.071(3)	0.0063	1
O(1)	0.000000	0.500000	0.240(9)	0.0063	1
O(2)	0.158(5)	0.001(4)	0.294(6)	0.0063	1
O(3)	-0.136(8)	0.253(5)	0.175(7)	0.0063	1
O(4)	0.409(6)	0.103(5)	0.73(1)	0.0063	1
O(5)	0.199(8)	¾	0.272(8)	0.0063	1

Table 3-S3: X-Ray Fluorescence Results for $PbVO_3Cl$

Element	Line	Concentration (mg/L)	Mol/L
Pb	L1	53.1(2)	0.256(5)
V	K12	13.16(5)	0.259(1)

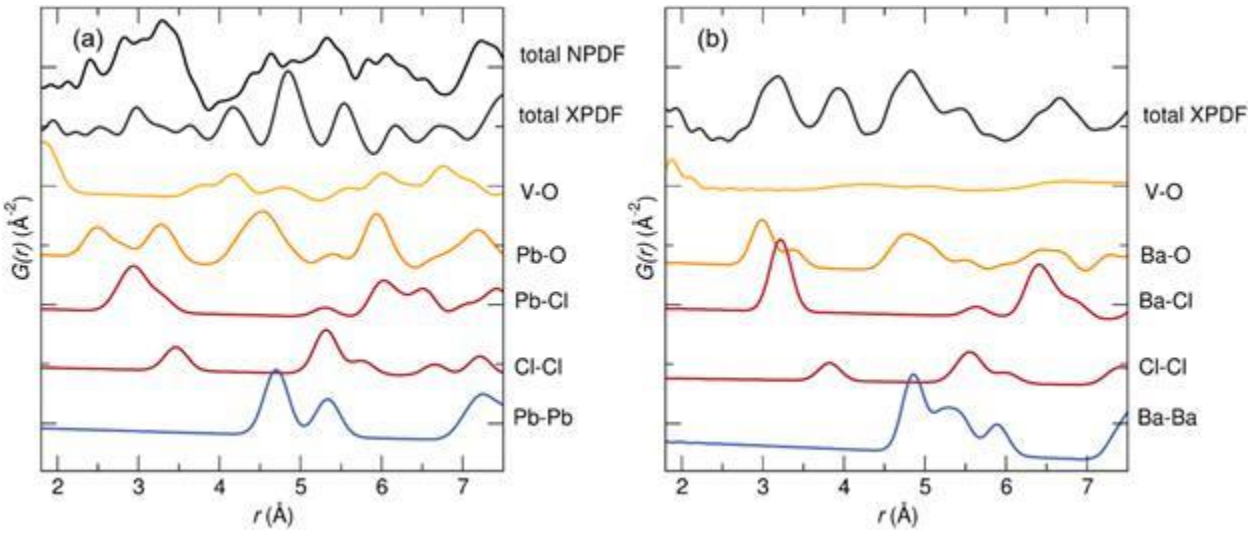

Figure 3-S1: Partial neutron (NPDF) and X-ray pair distribution function (XPDF) data for (a) $PbVO_3Cl$ and (b) $BaVO_3Cl$. Total PDF data is the experimental 300 K data for the respective sample.

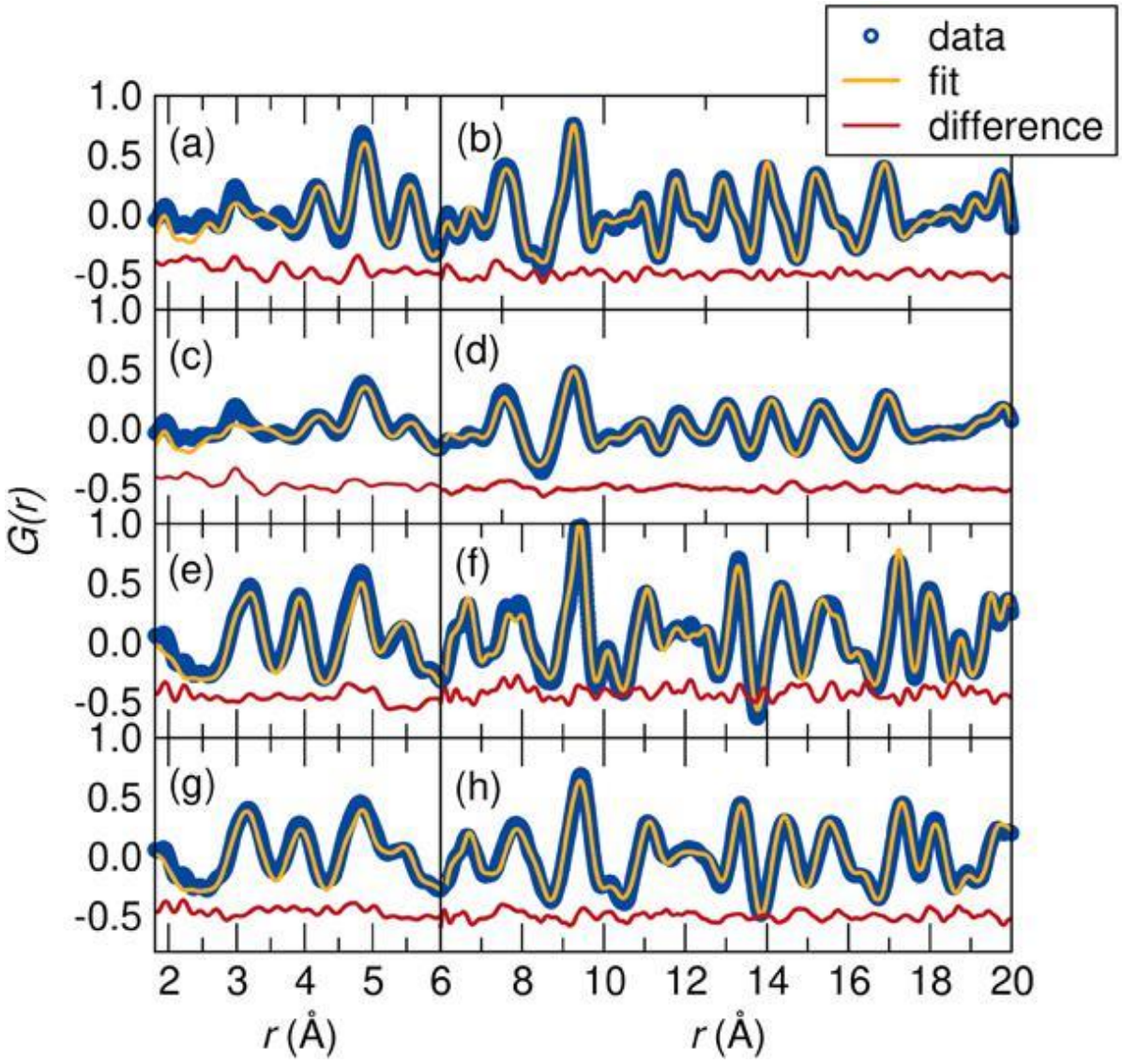

Figure 3-S2: Fits of the XPDF data against the Pnma crystallographic structure for $PbVO_3Cl$ at 300 K [(a) fit range of 1-6 Å, Rw = 9%; (b) fit range of 6-20 Å, Rw = 14%] and 573 K [(c) fit range of 1-6 Å, Rw = 10%; (d) fit range of 6-20 Å, Rw = 14%] and $BaVO_3Cl$ at 300 K [(e) fit range of 1-6 Å, Rw = 10%; (f) fit range of 6-20 Å, Rw = 16%] and 573 K [(c) fit range of 1-6 Å, Rw = 7%; (d) fit range of 6-20 Å, Rw = 17%].

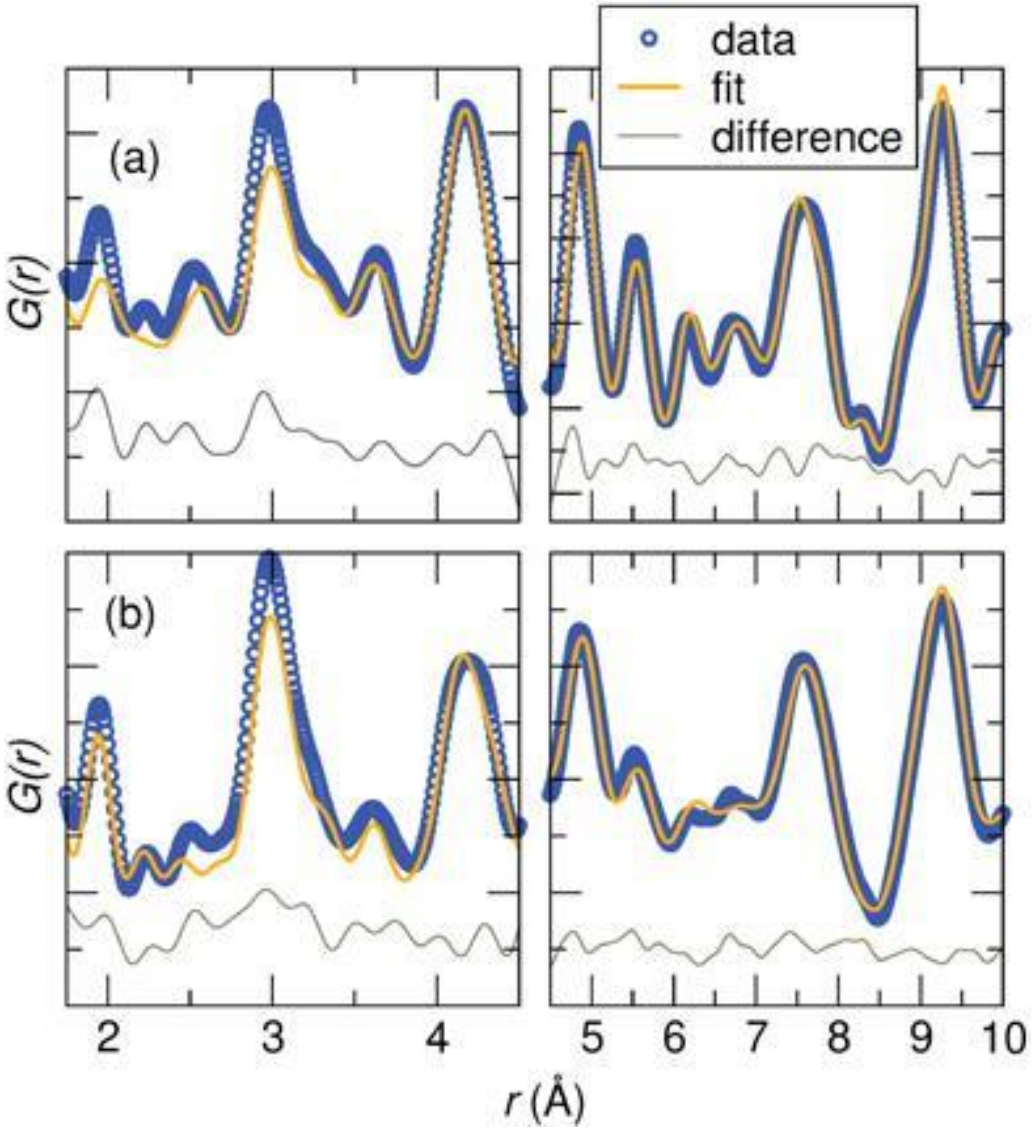

Figure 3-S3: Fits of the XPDF data against the *Pnma* crystallographic structure for $PbVO_3Cl$ at (a) 570 K (left panel: fit range of 1.75 - 4.5 Å, *Rw* = 30%; right panel: fit range of 5- 10 Å, *Rw* = 12%) and (b) (left panel: fit range of 17.5 - 4.5 Å, *Rw* = 37%; right panel: fit range of 5 - 10 Å, *Rw* = 14%) indicate that the poor local fit is not a result of correlations arising from poor scatterers; a poor fit to the local coordination environment is still observed over length scales where the data is not dominated by scattering from Pb, suggesting disorder of the local coordination environment of Pb.

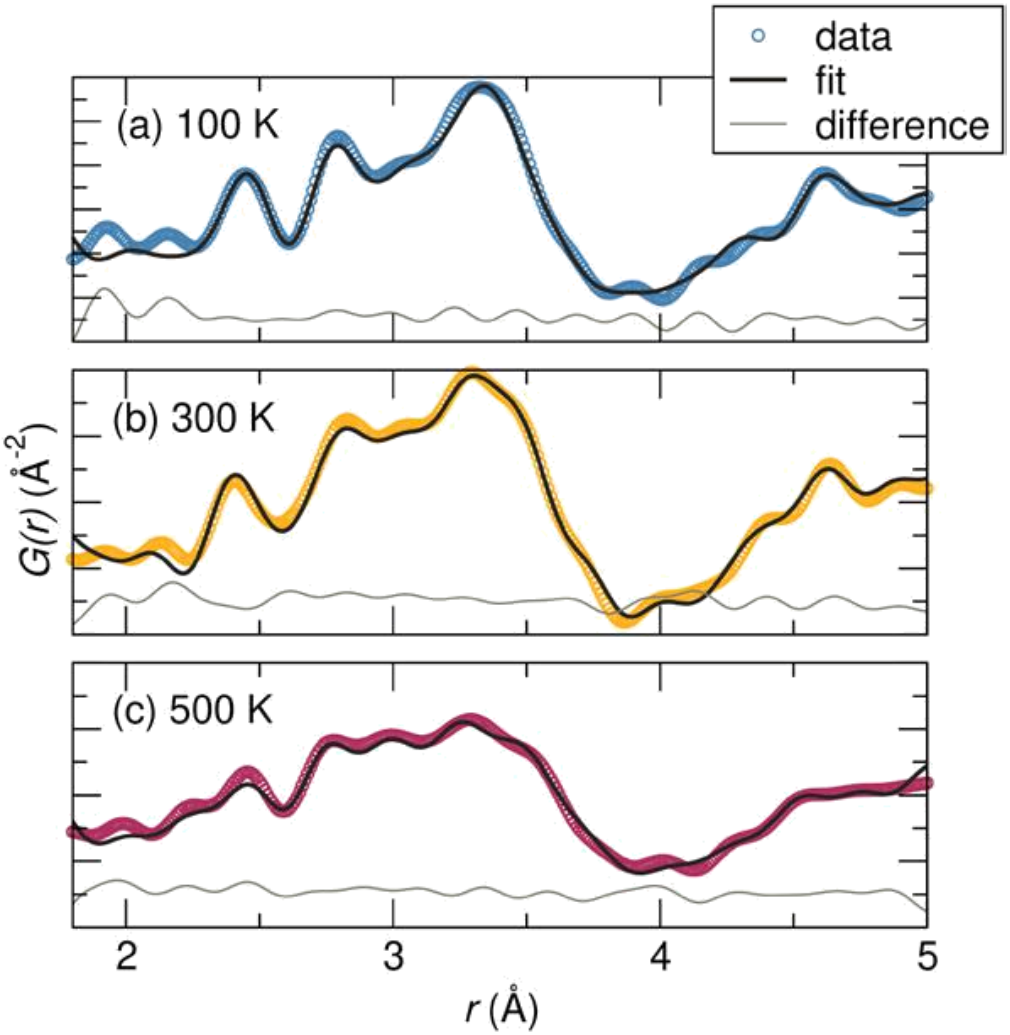

Figure 3-S4: Neutron PDF data of $PbVO_3Cl$ fit against the *Pnma* structure at (a) 100 K (*Rw* = 11%), (b) 300 K (*Rw* = 10%), and (c) 500 K (*Rw* = 13%).

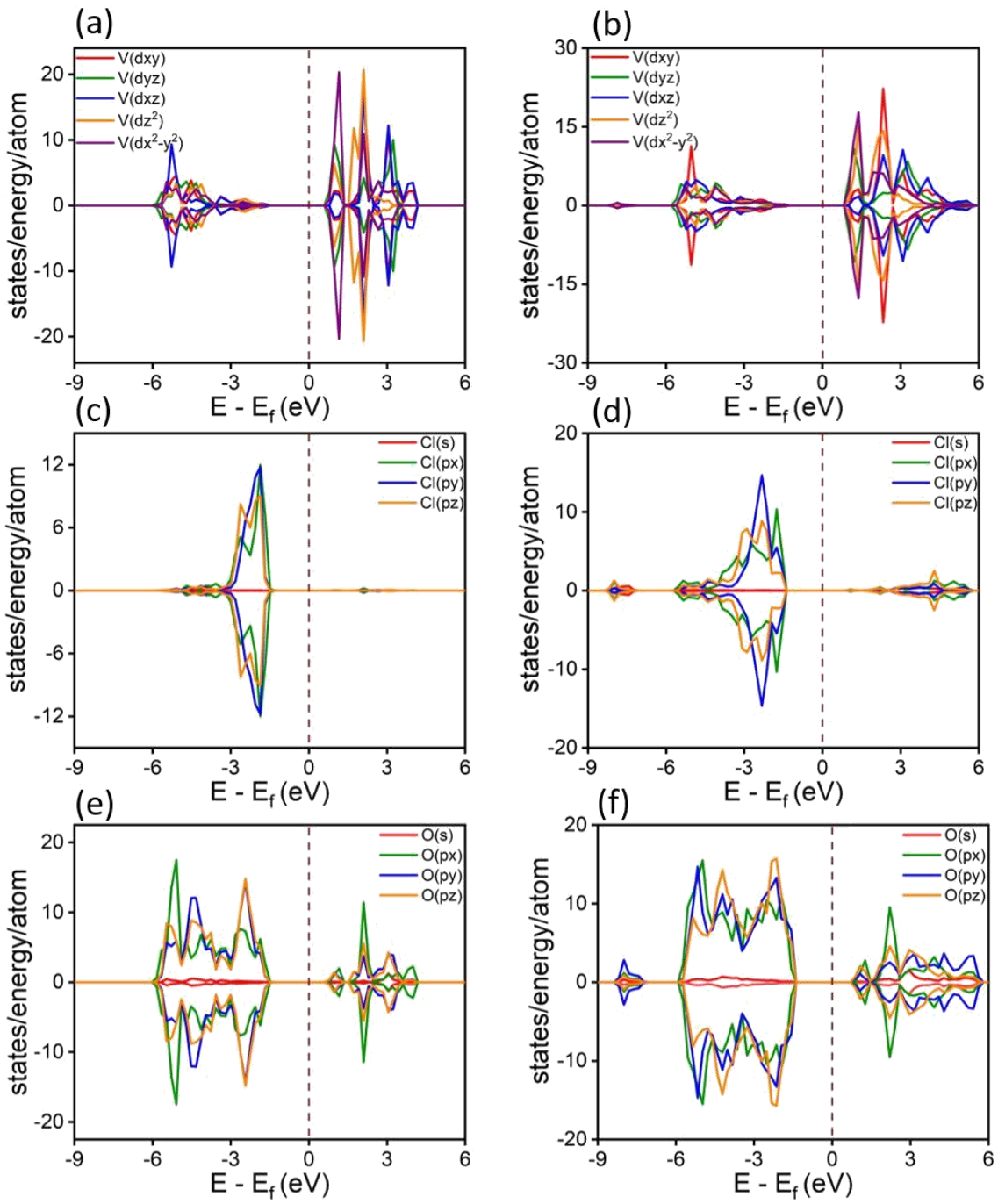

Figure 3-S5: Projected density of states calculated using GGA+U for a) vanadium states in $BaVO_3Cl$; b) vanadium states in $PbVO_3Cl$; c) chlorine states in $BaVO_3Cl$; (d) chlorine states in $PbVO_3Cl$; (e) oxygen states in $BaVO_3Cl$; and (f) oxygen states in $PbVO_3Cl$.

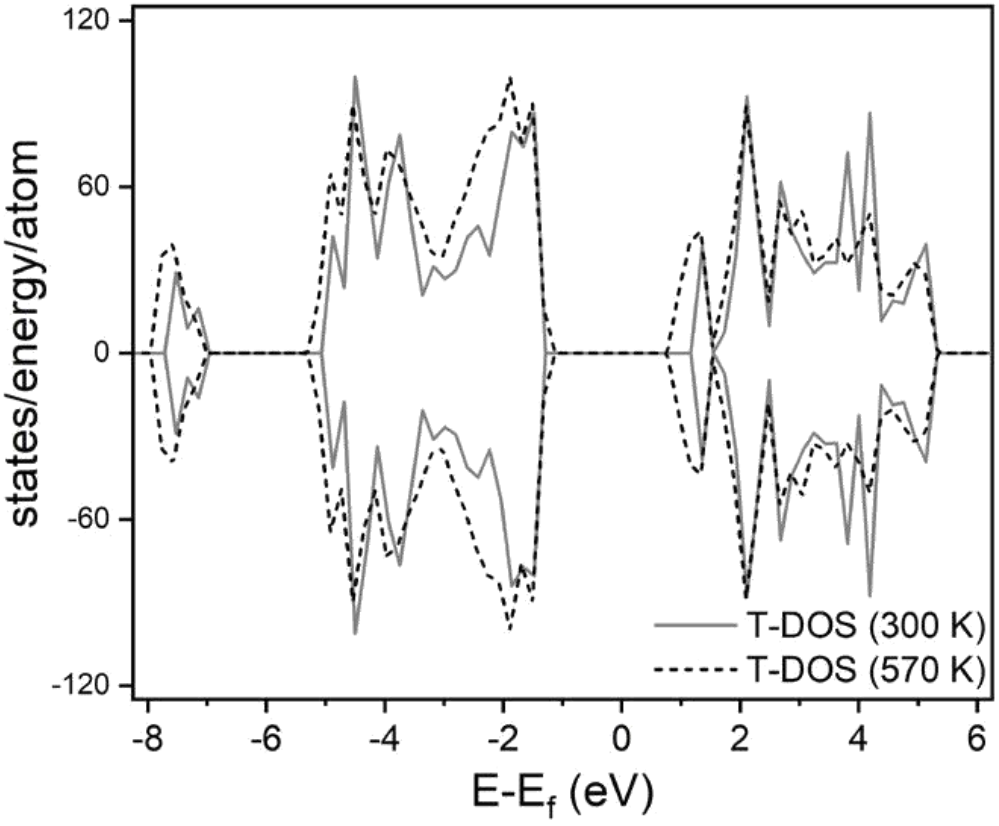

Figure 3-S6: Total density of states calculated using DFT for $PbVO_3Cl$ using structural models derived from XPDF measurements at 300 K and 570 K.

Table 4-S1: Refined crystallographic data for the nominal Pb1.5Nb2O6.5 with the A-site cation in the ideal 16d position.

Formula	$Pb_{1.49(2)}Nb_2O_{6.48(2)}$	$Pb_{1.47(2)}Nb_2O_{6.46(2)}$	$Pb_{1.47(2)}Nb_2O_{6.46(2)}$	$Pb_{1.47(2)}Nb_2O_{6.46(2)}$
Source	Neutron	Neutron	Neutron	Neutron
Beamline	BT-1, NIST	NOMAD, ORNL	NOMAD, ORNL	NOMAD, ORNL
Temperature (K)	300	300	200	100
Space Group	$Fd\bar{3}m$ (#227)	$Fd\bar{3}m$ (#227)	$Fd\bar{3}m$ (#227)	$Fd\bar{3}m$ (#227)
a (Å)	10.5618(1)	10.5648(3)	10.5616(2)	10.5555(2)
Volume a ($Å^3$)	1178.19(1)	1179.18(5)	1178.12(6)	1176.09(4)
Z	8	8	8	8
Formula weight (g/mol)	597.86	597.7	597.7	597.7
Pb U_{xx} ($Å^2$)	0.024(3)	0.023(4)	0.020(2)	0.018(2)
Pb U_{xy} ($Å^2$)	-0.004(2)	-0.003(3)	-0.003(2)	-0.003(2)
Nb U_{iso} ($Å^2$)	0.009(2)	0.010(4)	0.009(3)	0.008(3)
O (48*f*) U_{iso} $Å^2$)	0.0092(8)	0.009(2)	0.007(2)	0.006(3)
O (8*b*) U_{iso} ($Å^2$)	0.062(5)	0.053(5)	0.054(4)	0.053(4)
O (48*f*) *x* ($Å^2$)	0.3133(5)	0.3139(7)	0.3140(6)	0.3140(6)
R_{wp} (%)	7.28	5.47	5.82	6.21

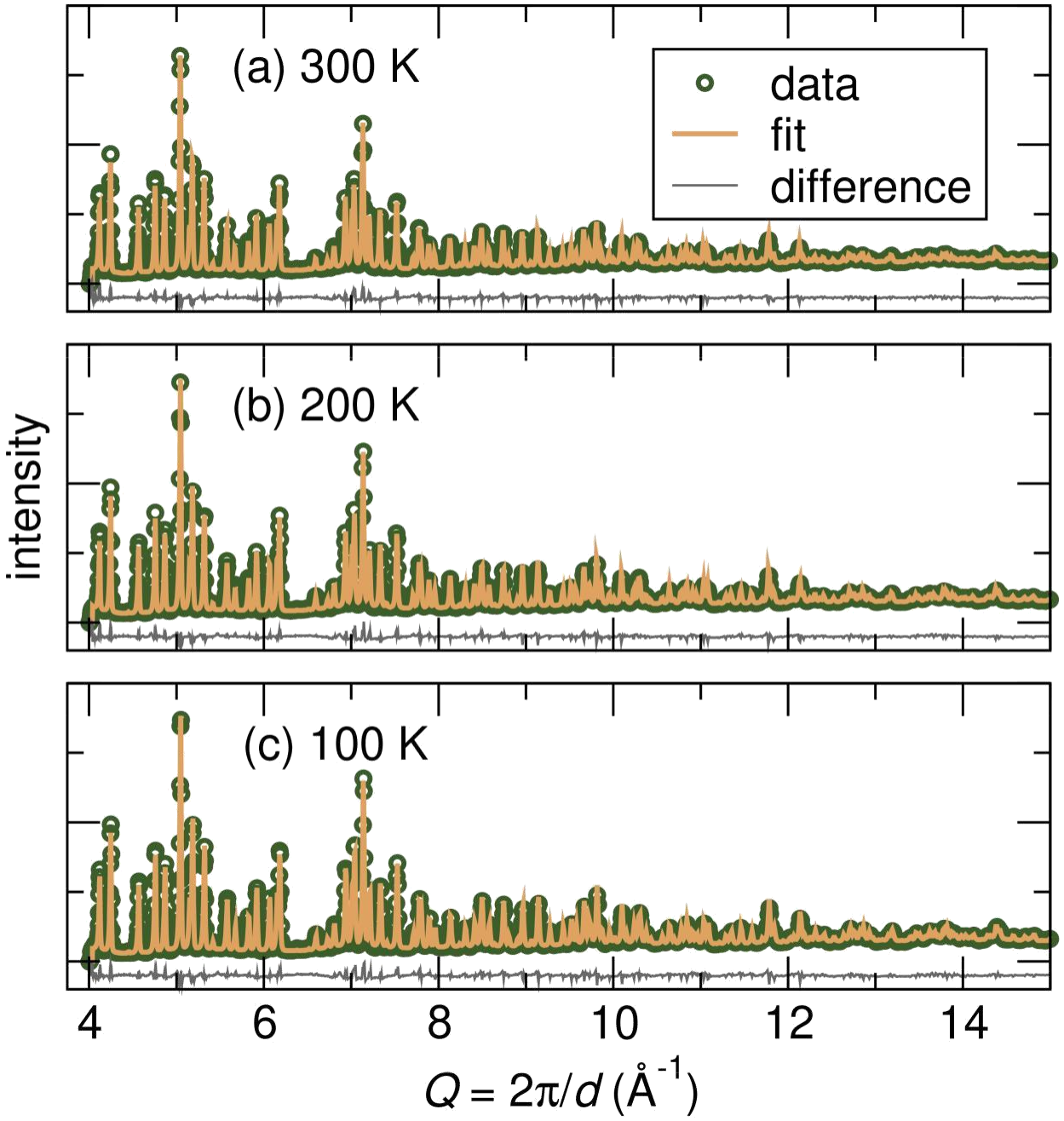

Figure 4-S1: Fits of the neutron diffraction data (NOMAD, SNS, ORNL, bank 5) at (a) 300 K, (b) 200 K, and (c) 100 K against the $Fd\bar{3}m$ model with Pb in the 16d Wyckoff position.

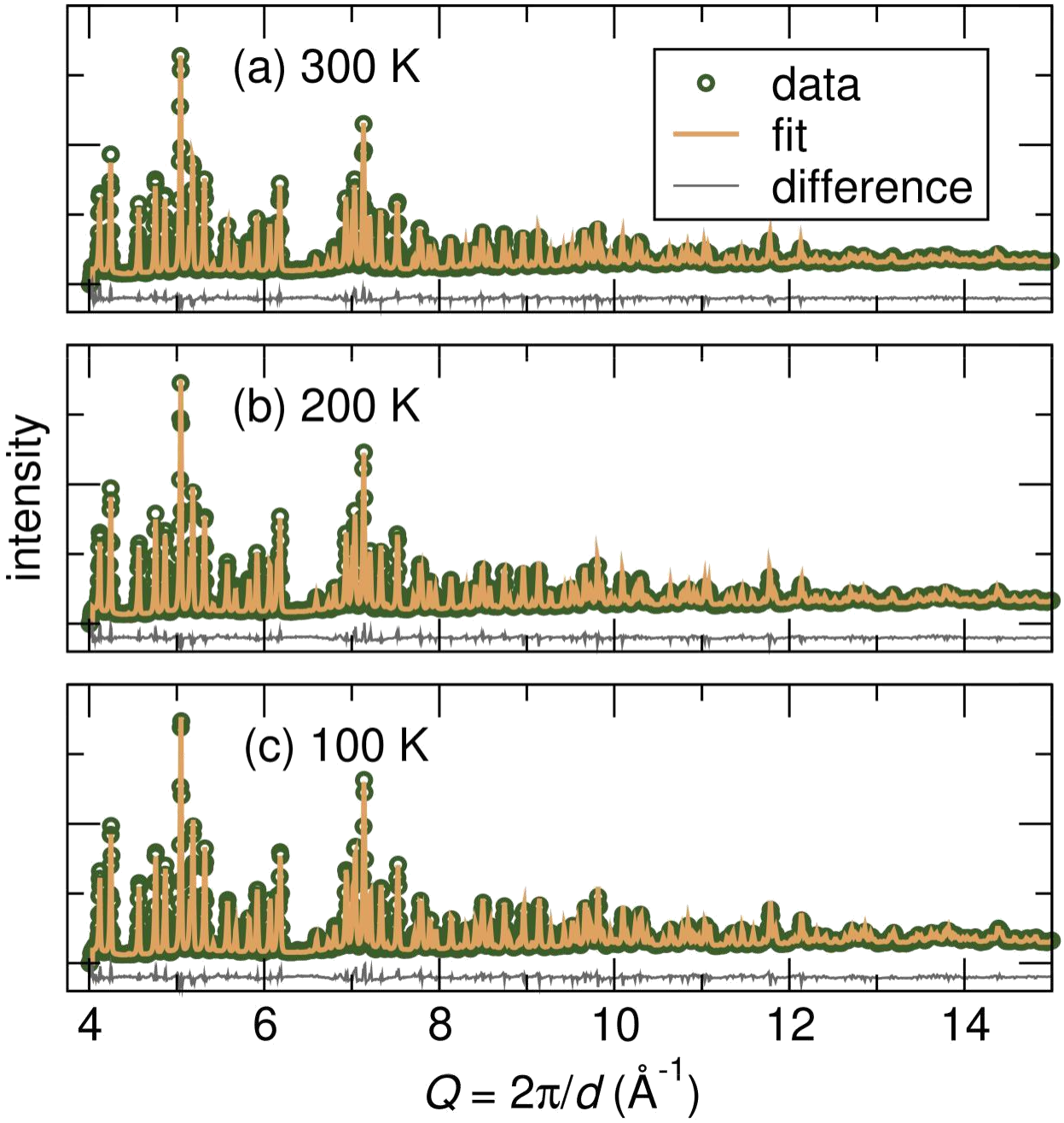

Figure 4-S2: Experimental data collected at various temperatures compared to calculated partials from cubic $Fd\bar{3}m$ model with the A-site cation in the 16d Wyckoff position.

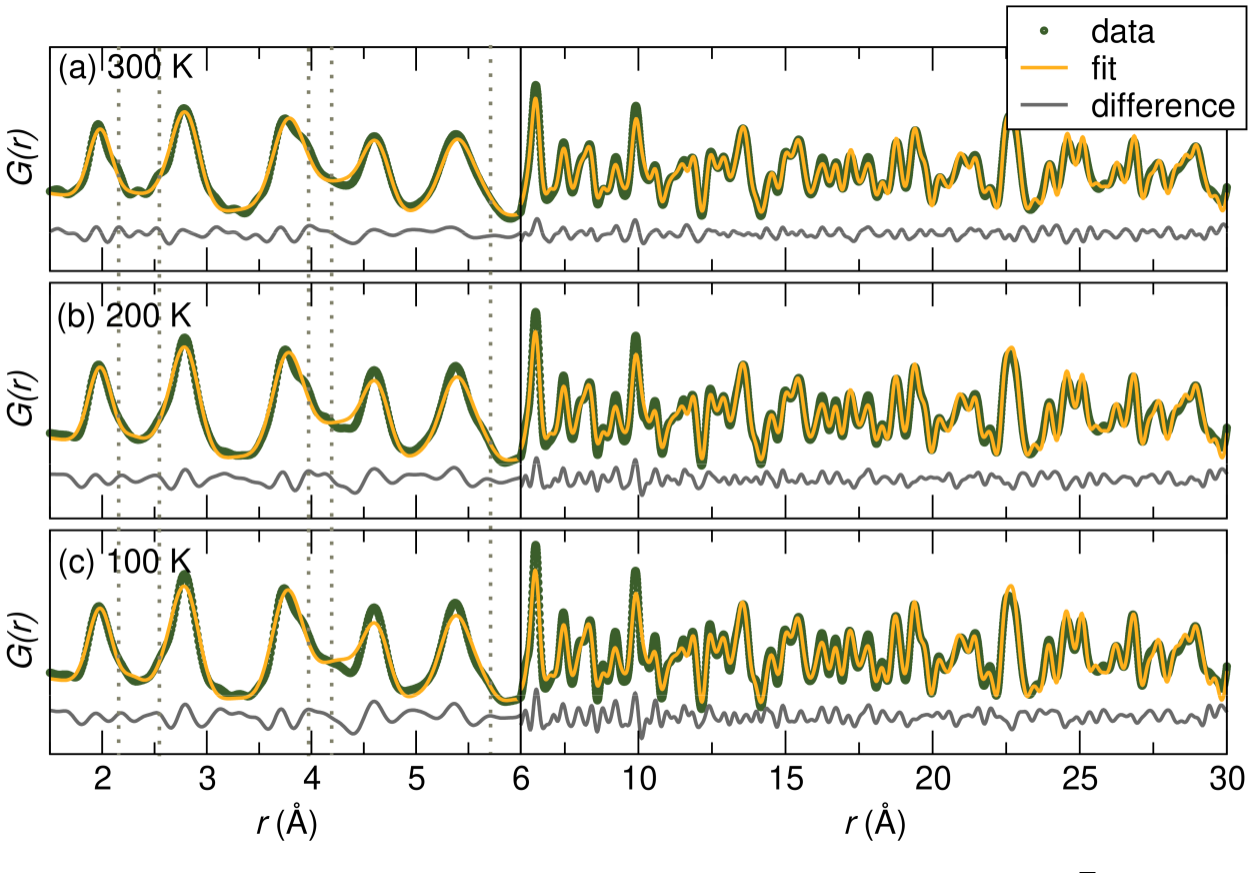

Figure 4-S3: Fits of the NPDF data (NOMAD, SNS, ORNL) against the cubic $Fd\bar{3}m$ model at (a) 300 K, (b) 200 K, (c) 100 K. For these fits the A-site cation was placed in the 16d Wyckoff position and anisotropic ADPs were allowed to refine.

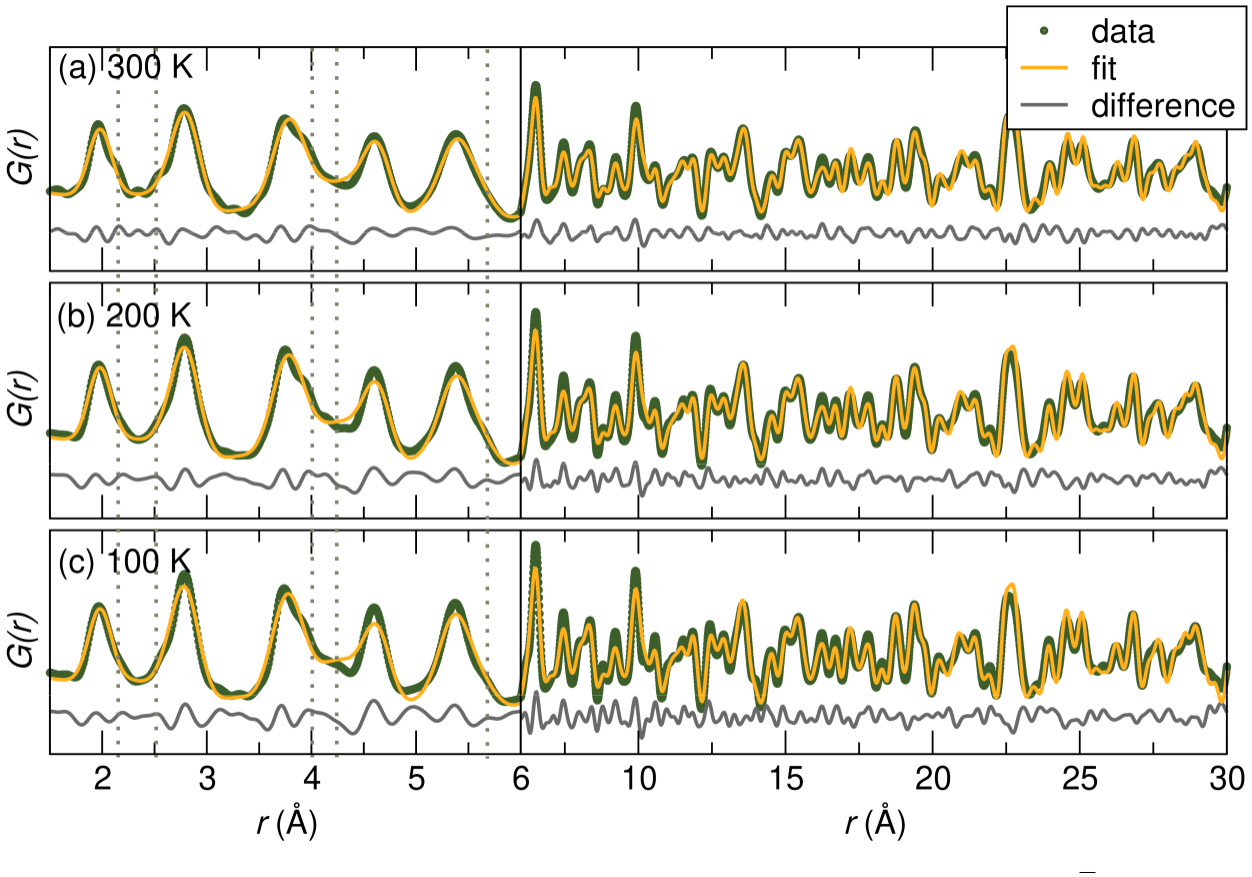

Figure 4-S4: Fits of the NPDF data (NOMAD, SNS, ORNL) against the cubic $Fd\bar{3}m$ model at (a) 300 K, (b) 200 K, (c) 100 K. For these fits the A-site cation was placed in the 96g Wyckoff position and isotropic ADPs were allowed to refine.

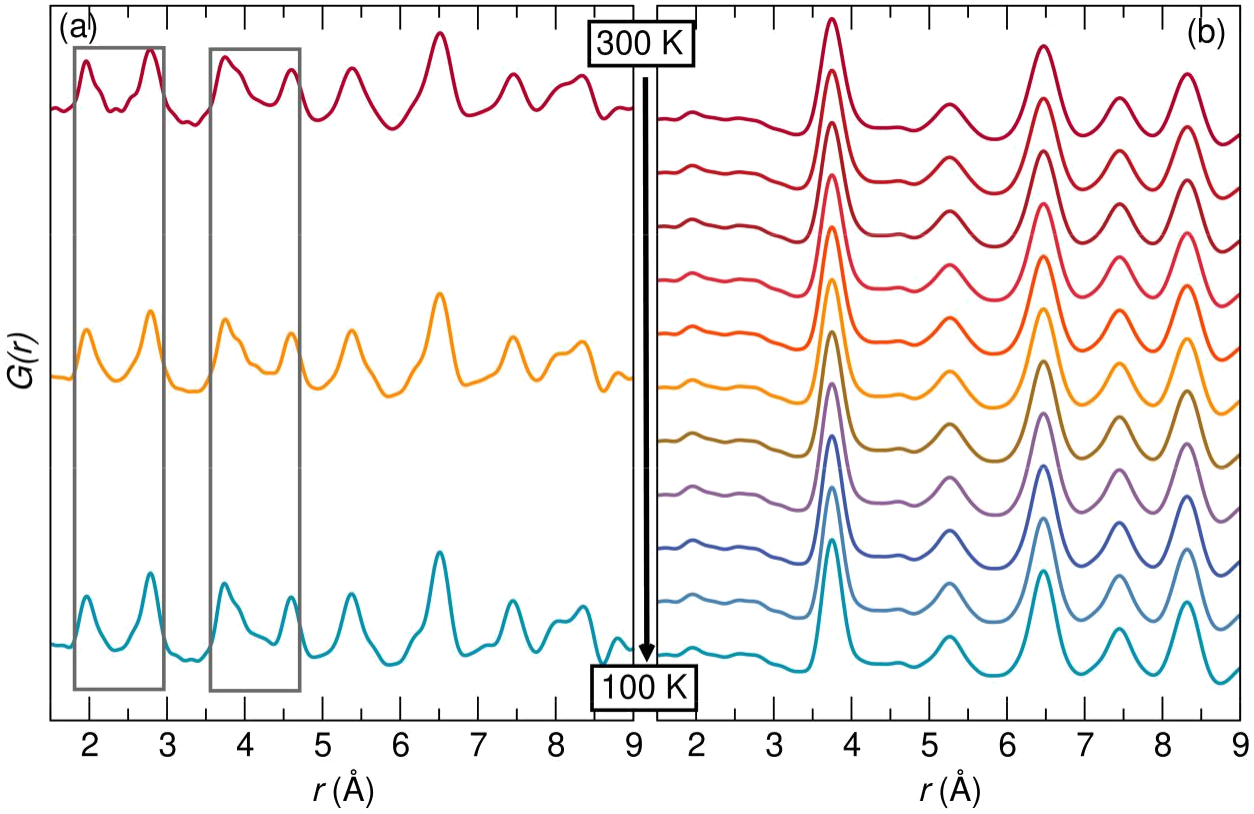

Figure 4-S5: Variable temperature (a) neutron (NOMAD, SNS) and (b) X-ray (28-ID-1, BNL) PDF data from 300 to 100 K. Highlighted regions in the NPDF data illustrate the evolution of new peaks upon warming. Note that this trend is not as evident in the XPDF data, which is dominated by Pb-Pb correlations due to the high scattering power of Pb relative to the other elements in the system.

Appendix C Other Projects

1. Preliminary data of the cubic and rhombohedral lead niobates

The lead niobate systems, $Pb_nNb_2O_{5+n}$ ($1.5 < n < 2.5$), show great promise for the development of tunable dielectric materials as changing the Pb concentration changes the relative dielectric constant.[1] Moreover, the relative dielectric constant, ε_r, and the Q-factor, Q, show a dependence upon n.[2] In addition, different synthetic actions such as rapid quenching and post-synthesis annealing temperatures can affect whether the final product includes mixed phases or a single phase.[3] Cook and Jaffe were the first to synthesize and report the existence of the stoichiometric lead niobate, $Pb_2Nb_2O_7$, which has a distorted fluorite structure of rhombohedral symmetry whereas $Pb_{1.5}Nb_2O_{6.5}$ possesses a cubic pyrochlore structure.[4] Since then, several other groups have prepared $Pb_2Nb_2O_7$ by conventional solid-state methods. There remain, however, unanswered questions with the composition and structure of $Pb_2Nb_2O_7$. Variation in ε_r have raised concerns about the oxygen concentration due to the volatility of one of the starting reagents, PbO.[2-3]

It is well known that lone pair electrons contribute to asymmetric coordination and resulting in acentric or even polar crystal structures with potential dielectric properties.[5] We attempted to synthesize the stoichiometric lead niobate, $Pb_2Nb_2O_7$, to investigate the relationship between the Pb^{2+} $6s^2$ lone pair and rhombohedral distortion of pyrochlore structure, which is not yet understood. We aimed to prepare powder sample of $Pb_2Nb_2O_7$ based on a phase equilibrium diagram for the system PbO-Nb_2O_5.[6] The phase diagram shows $Pb_2Nb_2O_7$ as a congruently melting compound. $Pb_{1.5}Nb_2O_{6.5}$ was prepared by using stoichiometric amounts of PbO and Nb_2O_5 and $Pb_2Nb_2O_7$ was prepared with $2PbO:1Nb_2O_5$ molar ratio. For both samples, starting materials were ground in an agate mortar and pestle. The mixtures were transferred into an alumina crucible and subsequently placed inside a fused silica ampoule. The ampoule was sealed under vacuum, heated

at 10 °C/min to 1000 °C, where it dwelled for 10 hours, and then cooled to 25 °C at 20 °C/min. The powder products were visibly light yellow with typical yield of ~93%. Upon annealing at 1000 °C, the light-yellow sample appeared as a pale gray powder as shown in Figure 1. Two different phases of cubic $Pb_{1.5}Nb_2O_{6.5}$ and rhombohedral $Pb_2Nb_2O_7$.

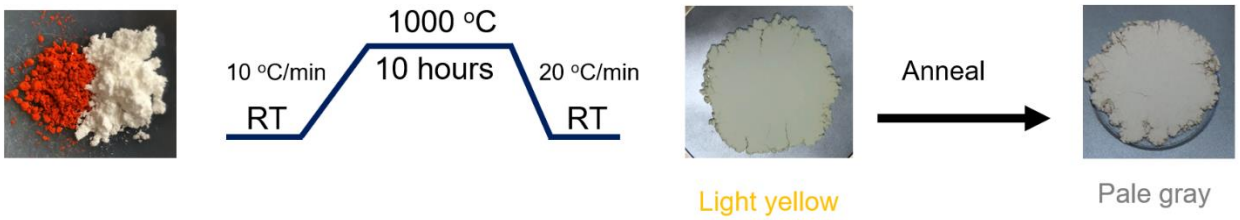

Cubic phase: $3PbO + 2Nb_2O_5 \rightarrow Pb_{1.5}Nb_2O_{6.5}$

Rhombohedral phase: $2PbO + Nb_2O_5 \rightarrow Pb_2Nb_2O_7$

Figure 1: Heating profile of cubic and rhombohedral lead niobate. Yellow powders appear to be light gray after annealing.

Powder X-ray diffraction data were collected on all samples at room temperature using laboratory PANalytical Empyrean diffractometer equipped with Cu K_α for phase identification. The yellow samples of rhombohedral phase were indexed with a mixture of $Pb_{2.31}Nb_2O_{7.31}$ and $Pb_{2.44}Nb_2O_{7.44}$ compositions which adopt the *R*3*mh* space group while the yellow cubic lead niobate crystallizes in the $Fd\bar{3}m$ space group.

Cubic $Pb_{1.5}Nb_2O_{6.5}$

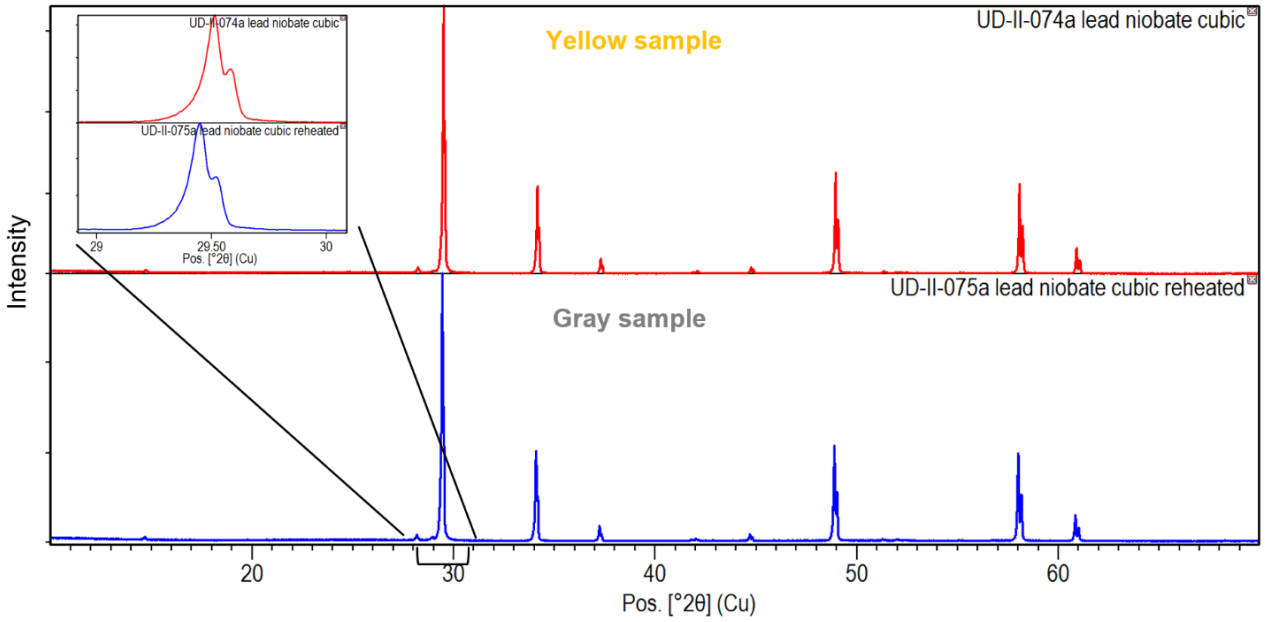

Figure 2: X-ray diffraction patterns of cubic lead niobate on yellow and gray samples. A peak-shifting to lower 2-theta angle of the (hkl) at 28.5° is observed.

Rhombohedral lead niobate

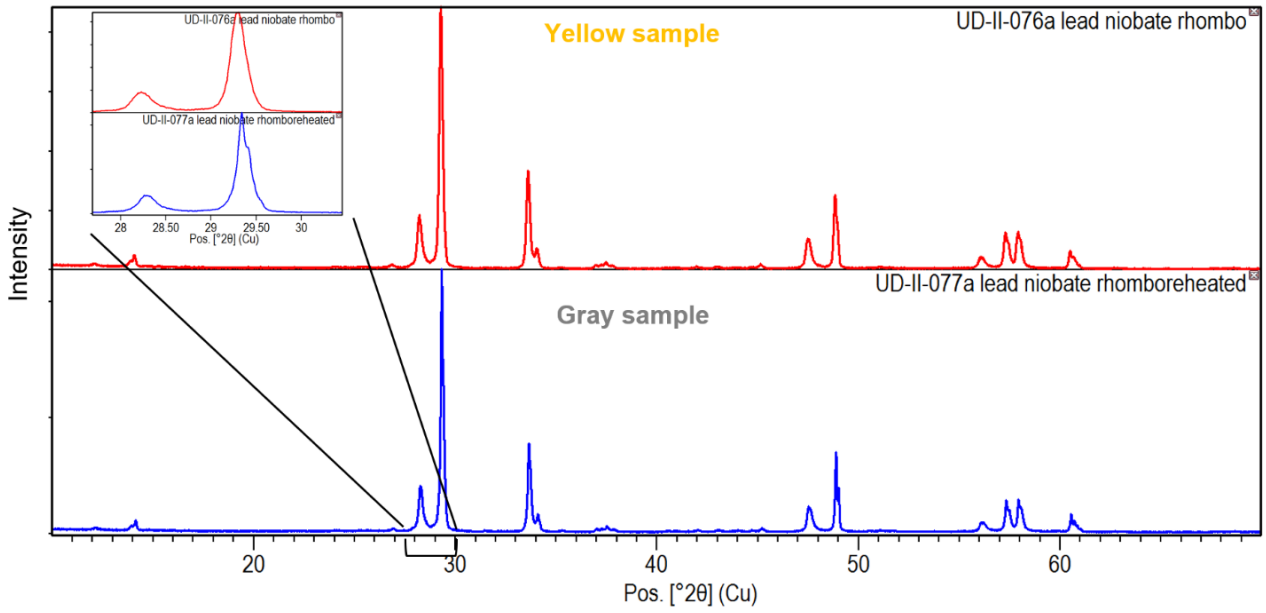

Figure 3: X-ray diffraction patterns of rhombohedral lead niobate samples. Peak-shifting is not observed in the diffraction pattern of the gray sample, but peak-splitting of the (hkl) peaks at 2θ = 29.4°, 48.9°, and 57.3°, respectively.

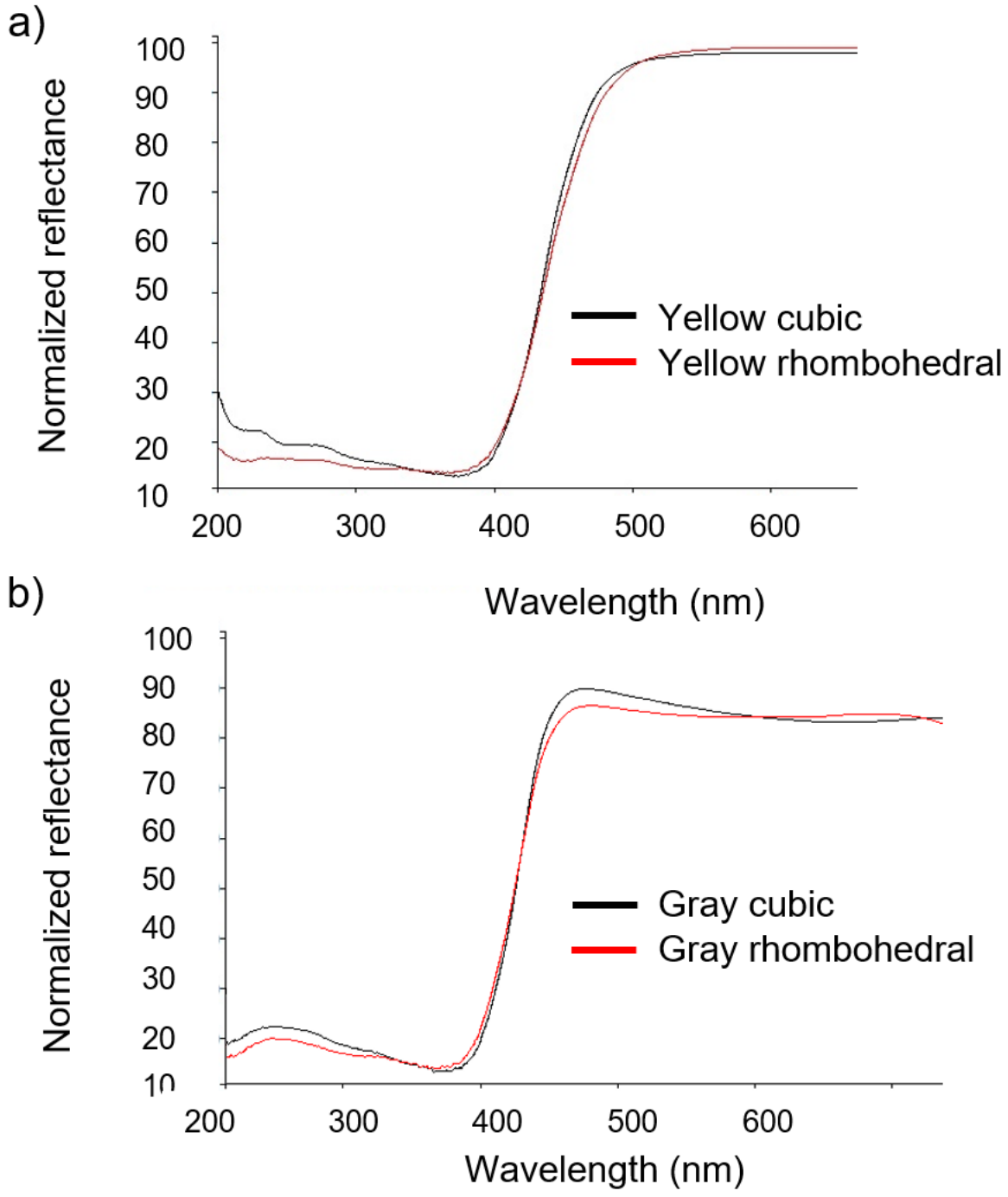

Figure 4: Diffuse reflectance data of the cubic a) and rhombohedral b) lead niobate samples.

a)

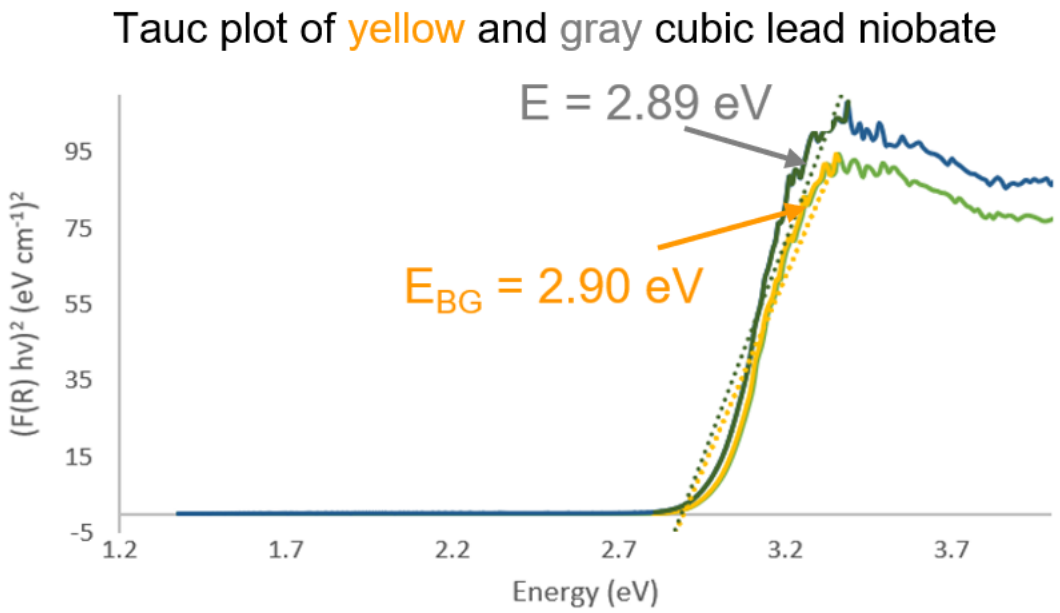

b)

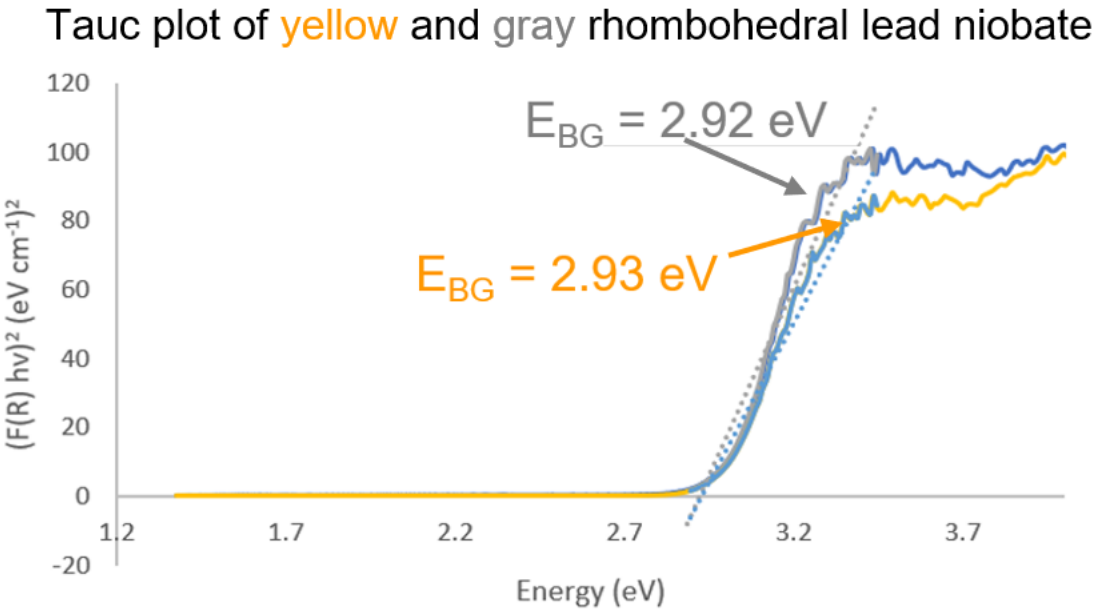

Figure 5: Tauc plots for cubic a) and rhombohedral b) phases of lead niobate. Tauc plots show that the band gaps of the yellow and gray sample in each phase are very close to each other.

2. Rietveld refinement on Rhombohedral pyrochlore $Pb_{2.31}Nb_2O_{7.31}$ and $Pb_{2.44}Nb_2O_{7.44}$

Neutron scattering data were collected on both yellow and gray samples of the rhombohedral $Pb_{2.31}Nb_2O_{7.31}$ and $Pb_{2.44}Nb_2O_{7.44}$ at room temperature at the National Institute of Standards and Technology (NIST) Center for Neutron Research. Rietveld refinement was performed using GSAS-II software[7], and the refinement results were shown in Table 1. Figures 6, 7, 8, 9, and 10 show Rietveld fits of neutron diffraction data collected for the yellow and gray rhombohedral phase samples modeled as a mixture of $Pb_{2.31}Nb_2O_{7.31}$ and $Pb_{2.44}Nb_2O_{7.44}$ phases.[8] Refined crystallographic data of rhombohedral yellow sample modeled as solely $Pb_{2.31}Nb_2O_{7.31}$ are shown in Figures 11 and 12.

Table 1: Summary of Rietveld refinement results on neutron data

	Rhombohedral yellow		Rhombohedral gray	
	$Pb_{2.31}Nb_2O_{7.31}$	$Pb_{2.44}Nb_2O_{7.44}$	$Pb_{2.31}Nb_2O_{7.31}$	$Pb_{2.44}Nb_2O_{7.44}$
Weight fraction (%)	47.0	53.0	42.0	58.0
Space group	*R* 3 *m h*	*R* 3 *m h*	*R* 3 *m h*	*R* 3 *m h*
a (Å)	7.4707(4)	7.4648(3)	7.4703(6)	7.4673(7)
b (Å)	7.4707(4)	7.4648(3)	7.4703(6)	7.4673(7)
c (Å)	66.832(4)	95.139(9)	66.813(4)	95.181(7)
GoF	1.471		1.446	
R_w (%)	9.348		8.724	

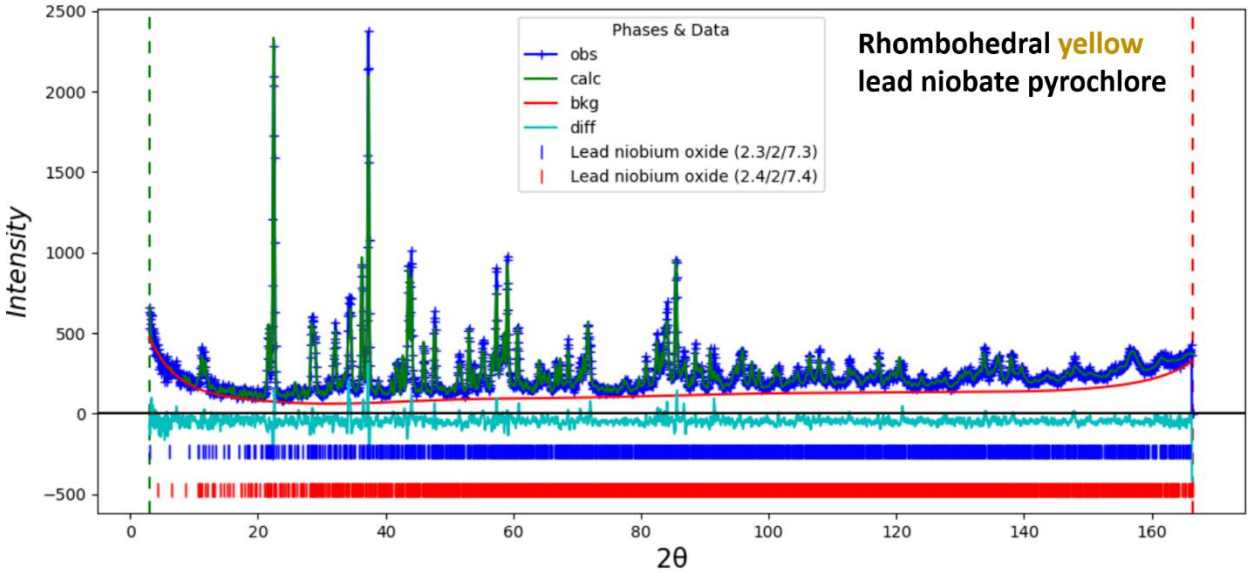

Figure 6: Rietveld fit of neutron diffraction data of the yellow sample modeled with R3mh space group with both $Pb_{2.31}Nb_2O_{7.31}$ and $Pb_{2.44}Nb_2O_{7.44}$ compositions. The best fit was achieved with R_w = 9.348%.

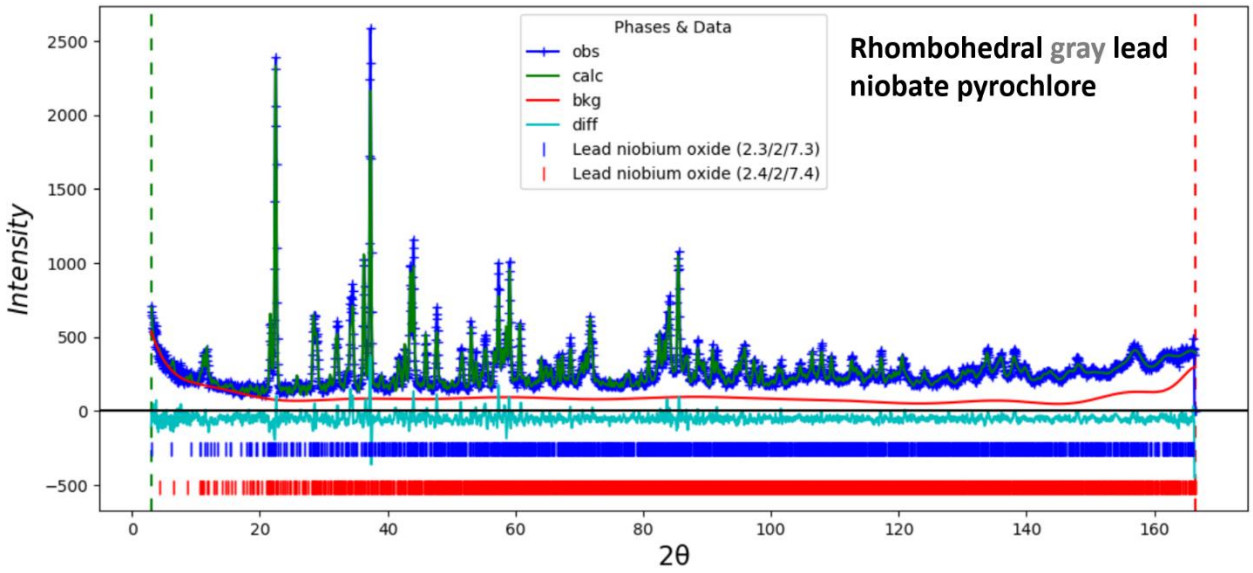

Figure 7: Rietveld fit of neutron diffraction data of the gray sample modeled with R3mh space group with both $Pb_{2.31}Nb_2O_{7.31}$ and $Pb_{2.44}Nb_2O_{7.44}$ compositions. The best fit is achieved with R_w = 8.724%.

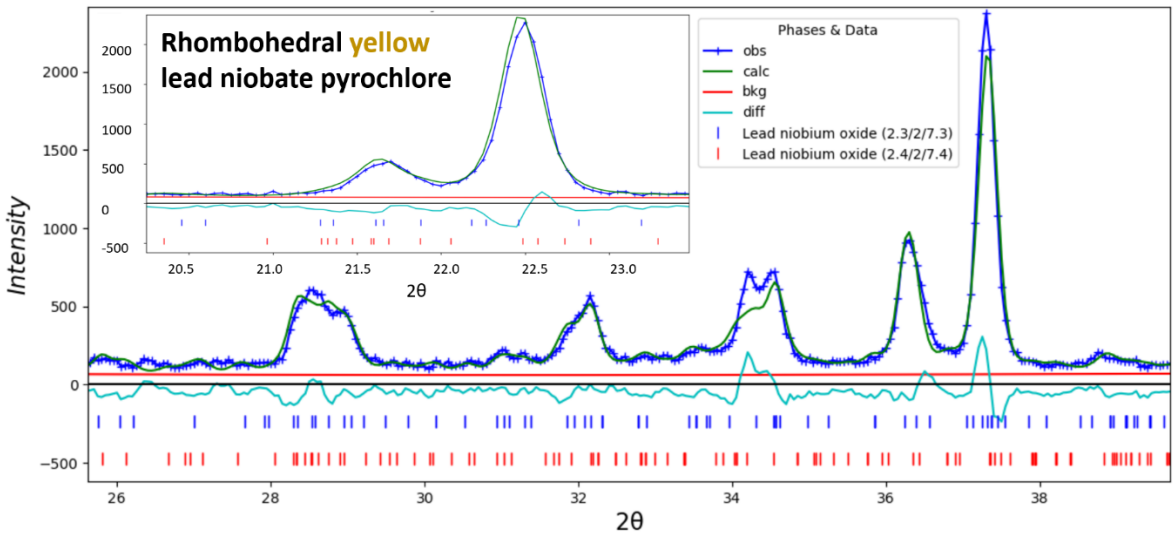

Figure 8: Rietveld fit of neutron diffraction data of yellow sample modeled with *R*3*mh* space group with both $Pb_{2.31}Nb_2O_{7.31}$ and $Pb_{2.44}Nb_2O_{7.44}$ compositions was zoomed in for peak-fitting analysis. Inset is the zoom-in of peaks from 2θ ~ 20.5° to 23.0°. The model is not fitted well to the data indicating by the mis-fit of peaks at 2θ ~ 28.5°, 32°, and 34°. Atomic displacement parameters and thermal parameters were allowed to refine.

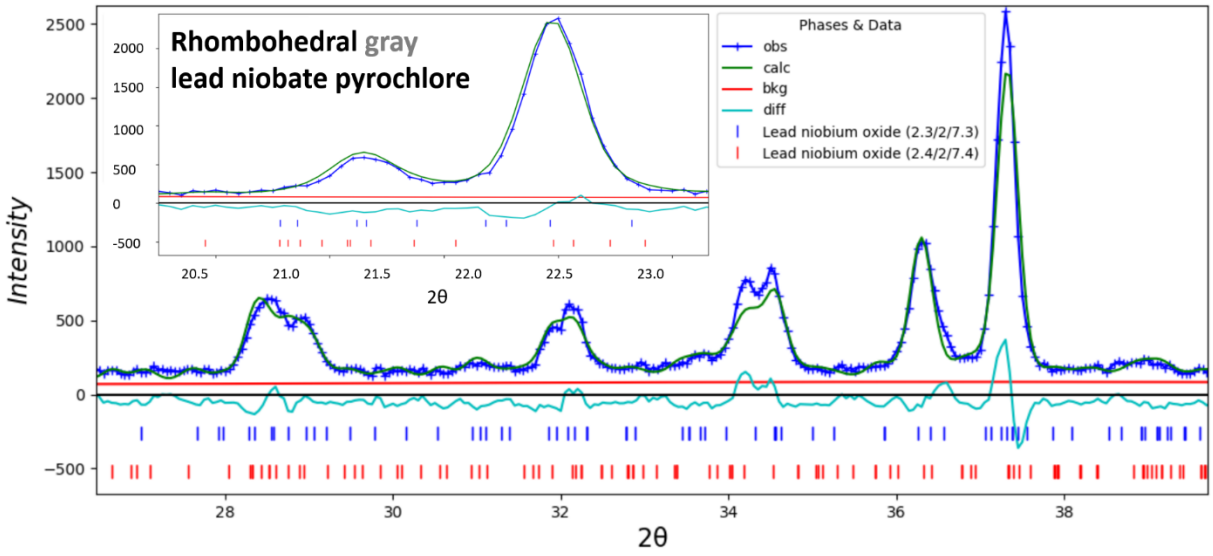

Figure 9: Rietveld fit of neutron diffraction data of gray sample modeled with R3mh space group with both $Pb_{2.31}Nb_2O_{7.31}$ and $Pb_{2.44}Nb_2O_{7.44}$ compositions was zoomed in for peak-fitting analysis. Inset is the zoom-in of peaks from 20.5° to 23.0° 2-theta. Similar to the Rietveld fit of the rhombohedral yellow sample, the model does not fit well at 2θ ~ 28.5°, 32°, and 34°. The diffraction patterns of the yellow and gray samples are quite similar except the peaks at 2θ~ 32° which have left shoulder for the yellow sample and almost a doublet for the gray sample. Other than that, the average structures determine from Rietveld refinements are similar for both yellow and gray samples despite different optical colors.

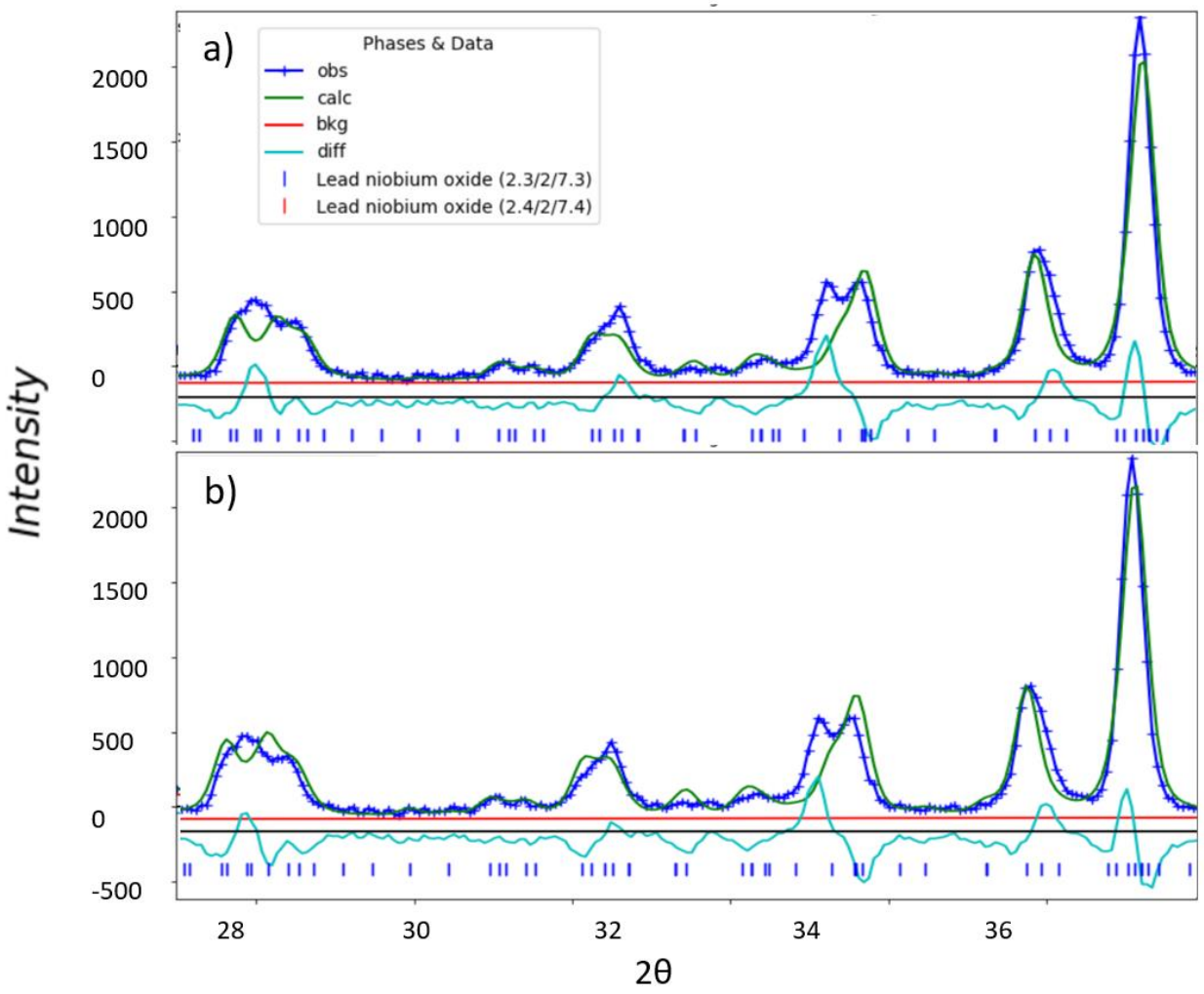

Figure 10: Rietveld fit of neutron diffraction data of the yellow sample against *R*3*mh* model using single phase $Pb_{2.31}Nb_2O_{7.31}$. (220) peak at 2θ~ 37.3° contains only Pb and Nb atoms which are at Pb(2), Pb(4), Pb(6), Pb(7), Nb(1), Nb(3), and Nb(5) positions. (20$\bar{7}$) peak at 2θ~ 22.5° contains only oxygen atoms at O(2), O(4), O(8), O(10), O(12), O(15), and O(20) positions. Panel a) and b) are the XRD patterns from Refinement 1 and Refinement 2, respectively.

Name	Type	refine	x	y	z	frac	site sym	mult	I/A	Uiso
Nb1	Nb+5		0.51871	0.48129	0.18394	1.0000	m(110)	9	I	0.01812
Nb2	Nb+5		0.00000	0.00000	0.47056	1.0000	3m(100)	3	I	-0.04927
Nb3	Nb+5		0.16609	0.83391	0.09172	1.0000	m(110)	9	I	0.00204
Nb4	Nb+5		0.00000	0.00000	0.04968	1.0000	3m(100)	3	I	0.01134
Nb5	Nb+5		0.83429	0.16571	0.00220	1.0000	m(110)	9	I	0.01757
Nb6	Nb+5		0.00000	0.00000	0.61968	1.0000	3m(100)	3	I	-0.00143
Nb7	Nb+5		0.00000	0.00000	0.90345	1.0000	3m(100)	3	I	0.01625
Pb1	Pb+2		0.00000	0.00000	0.18172	1.0000	3m(100)	3	I	0.01277
Pb2	Pb+2		0.83139	0.16861	0.14502	1.0000	m(110)	9	I	0.03664
Pb3	Pb+2		0.00000	0.00000	0.76713	1.0000	3m(100)	3	I	-0.00188
Pb4	Pb+2		0.49823	0.50177	0.04400	1.0000	m(110)	9	I	0.00979
Pb5	Pb+2		0.00000	0.00000	0.33106	1.0000	3m(100)	3	I	0.00078
Pb6	Pb+2		0.83548	0.16452	0.28471	1.0000	m(110)	9	I	0.01666
Pb7	Pb+2		0.16712	0.83288	0.23920	1.0000	m(110)	9	I	0.01923
O1	O-2		0.78434	0.21566	0.17974	1.0000	m(110)	9	I	0.00740
O2	O-2		0.45728	0.54272	0.15533	1.0000	m(110)	9	I	0.01396
O3	O-2		0.20343	0.79657	0.12101	1.0000	m(110)	9	I	0.01484
O4	O-2		0.87180	0.12820	0.09697	1.0000	m(110)	9	I	-0.00465
O5	O-2		0.45686	0.54314	0.08491	1.0000	m(110)	9	I	0.00546
O6	O-2		0.12868	0.87132	0.06389	1.0000	m(110)	9	I	0.00799
O7	O-2		0.87290	0.12710	0.03030	1.0000	m(110)	9	I	0.00969
O8	O-2		0.53875	0.46125	0.00466	1.0000	m(110)	9	I	-0.00080
O9	O-2		0.12550	0.87450	0.99612	1.0000	m(110)	9	I	0.01248
O10	O-2		0.79004	0.20996	0.97275	1.0000	m(110)	9	I	-0.00407
O11	O-2		0.12104	0.87896	0.91126	1.0000	m(110)	9	I	0.01142
O12	O-2		0.54643	0.45357	0.85566	1.0000	m(110)	9	I	0.01908
O13	O-2		0.87135	0.12865	0.87809	1.0000	m(110)	9	I	0.00234
O14	O-2		0.53830	0.46170	0.93889	1.0000	m(110)	9	I	-0.00910
O15	O-2		0.00000	0.00000	0.15532	0.8417	3m(100)	3	I	0.01527
O16	O-2		0.00000	0.00000	0.37633	0.8417	3m(100)	3	I	0.00364
O17	O-2		0.00000	0.00000	0.29392	0.8417	3m(100)	3	I	0.00809
O18	O-2		0.00000	0.00000	0.21691	0.8417	3m(100)	3	I	0.02737
O19	O-2		0.00000	0.00000	0.79290	0.8417	3m(100)	3	I	0.15212
O20	O-2		0.00000	0.00000	0.72866	0.8417	3m(100)	3	I	0.01203
O21	O-2		0.00000	0.00000	0.94470	0.8417	3m(100)	3	I	0.01400
O22	O-2		0.00000	0.00000	0.59049	0.8417	3m(100)	3	I	0.00381

Figure 11: Refined crystallographic data of rhombohedral yellow sample modeled with single phase $Pb_{2.31}Nb_2O_{7.31}$. There are 7 Nb positions and 7 Pb positions. The oxygen atoms are found in O1 to O14 for O positions, and O15 to O22 for O' positions. Setting the occupancies/fraction of Nb, Pb, and O atoms to 1 and that for O' to 0.8417 led to negative values of the atomic displacement parameters U_{iso} on some atomic positions.

Name	Type	refine	x	y	z	frac	site sym	mult	I/A	Uiso
Nb1	Nb+5		0.51790	0.48210	0.18399	1.0000	m(110)	9	I	0.01860
Nb2	Nb+5		0.00000	0.00000	0.47054	1.0000	3m(100)	3	I	0.01000
Nb3	Nb+5		0.16429	0.83571	0.09208	1.0000	m(110)	9	I	0.01000
Nb4	Nb+5		0.00000	0.00000	0.04996	1.0000	3m(100)	3	I	0.01115
Nb5	Nb+5		0.83135	0.16865	0.00200	1.0000	m(110)	9	I	0.01702
Nb6	Nb+5		0.00000	0.00000	0.61899	1.0000	3m(100)	3	I	0.01000
Nb7	Nb+5		0.00000	0.00000	0.90322	1.0000	3m(100)	3	I	0.01465
Pb1	Pb+2		0.00000	0.00000	0.18107	0.4715	3m(100)	3	I	0.01000
Pb2	Pb+2		0.83328	0.16672	0.14562	0.9939	m(110)	9	I	0.03198
Pb3	Pb+2		0.00000	0.00000	0.76732	1.2998	3m(100)	3	I	0.01000
Pb4	Pb+2		0.49931	0.50069	0.04413	0.9394	m(110)	9	I	0.00893
Pb5	Pb+2		0.00000	0.00000	0.33164	1.6817	3m(100)	3	I	0.01092
Pb6	Pb+2		0.83393	0.16607	0.28453	0.9501	m(110)	9	I	0.00769
Pb7	Pb+2		0.16568	0.83432	0.23895	1.1569	m(110)	9	I	0.01871
O1	O-2		0.78441	0.21559	0.17965	1.1587	m(110)	9	I	0.01194
O2	O-2		0.45504	0.54496	0.15601	0.8433	m(110)	9	I	0.01000
O3	O-2		0.19913	0.80087	0.11966	0.9377	m(110)	9	I	0.01405
O4	O-2		0.87269	0.12731	0.09734	1.1651	m(110)	9	I	0.01000
O5	O-2		0.45983	0.54017	0.08521	1.2228	m(110)	9	I	0.01140
O6	O-2		0.12556	0.87444	0.06304	1.0865	m(110)	9	I	0.01422
O7	O-2		0.86964	0.13036	0.03045	1.0646	m(110)	9	I	0.01000
O8	O-2		0.53941	0.46059	0.00448	1.1880	m(110)	9	I	0.01000
O9	O-2		0.12565	0.87435	0.99661	1.1504	m(110)	9	I	0.01274
O10	O-2		0.78907	0.21093	0.97233	1.3097	m(110)	9	I	0.01000
O11	O-2		0.11978	0.88022	0.91078	0.7056	m(110)	9	I	0.00719
O12	O-2		0.54677	0.45323	0.85557	0.6262	m(110)	9	I	0.01000
O13	O-2		0.87166	0.12834	0.87787	1.5203	m(110)	9	I	0.00959
O14	O-2		0.53925	0.46075	0.93909	0.8829	m(110)	9	I	-0.00704
O15	O-2		0.00000	0.00000	0.15374	0.7599	3m(100)	3	I	0.02678
O16	O-2		0.00000	0.00000	0.37553	0.4418	3m(100)	3	I	-0.00463
O17	O-2		0.00000	0.00000	0.29367	0.5974	3m(100)	3	I	0.00370
O18	O-2		0.00000	0.00000	0.21578	1.6220	3m(100)	3	I	0.06975
O19	O-2		0.00000	0.00000	0.79197	1.4763	3m(100)	3	I	0.26493
O20	O-2		0.00000	0.00000	0.72816	1.6062	3m(100)	3	I	0.04635
O21	O-2		0.00000	0.00000	0.94507	0.9783	3m(100)	3	I	0.01399
O22	O-2		0.00000	0.00000	0.59025	0.1310	3m(100)	3	I	-0.07106

Figure 12: Refined crystallographic data of rhombohedral yellow sample modeled as single phase $Pb_{2.31}Nb_2O_{7.31}$. This is from the Refinement 2. In this refinement, occupancies of Nb atoms were fixed to 1 while the others were refined. Then occupancies for all atoms were fixed, and the U_{iso} was refined. Then the U_{iso} with values less than 0.01 were set to 0.01. Since we were interested in

the effect of lone pair on Pb^{2+} coordination environment and the interaction between Pb and O, Nb occupancies were fixed to 1 and occupancies of Pb and O atoms were allowed to refine. Large values of occupancy, greater than 1, on the Pb and O sites point towards some structural disorder. Further refinement needs to be investigated.

References

1. Shirane, G.; Pepinsky, R., Dielectric Properties and Phase Transitions of $Cd_2Nb_2O_7$ and $Pb_2Nb_2O_7$ *Phys. Rev.* **1953,** *92*, 504.
2. Ubic, R.; Reaney, I. M., Structure and Dielectric Properties of Lead Pyrochlores. *J. Am. Ceram. Soc.* **2002,** *85* (10), 2472-2478.
3. Sreedhar, K.; Mitra, A., Formation and Transformation of Cubic Lead Niobate Pyrochlore Solid Solutions. *J. Am. Ceram. Soc.* **1999,** *82* (4), 1070-1072.
4. Cook, W. R.; Jaffe, H., Ferroelectricity in Oxides of Fluorite Structure. *Phys. Rev.* **1953,** *89*, 1297-1298.
5. Avanesyan, V. T.; Bordovskii, V. A.; Potachev, S. A., Dielectric Characterization of the Lone Pair Oxide Structure. *J. Non-Cryst Solids* **2002,** *305* (1-3), 136-139.
6. Roth, R. S., Phase Equilibrium Relations in the Binary System $PbO\text{-}Nb_2O_5$. *J. Res. Natl. Bur. Stand. (U. S.)* **1959,** *62*, 27-38.
7. Toby, B. H.; Dreele, R. B. V., GSAS-II: the Genesis of a Modern Open-Source all Purpose Crystallography Software Package. *J. Appl. Cryst.* **2013,** *46*, 544-549.
8. Bernotat-Wulf, H.; Hoffmann, W., Die Kristallstrukturen der Bleiniobate vom Pyrochlor-Types. *Z. Kristallogr.* **1982,** *158*, 101-117.

Biographical Information

Uyen Dang was born in Vietnam and came to the United State right after she graduated from high school in 2011. She attended Richland Community College in Dallas for English Speakers of Other Languages and core classes. Dang joined the Macaluso Group in February 2017 while she was pursuing her bachelor's degree in Biological Chemistry at University of Texas at Arlington. She received the B.S. degree in May 2018 and started her PhD program in solid-state chemistry under supervision of Dr. Robin Macaluso that fall. Her research focuses on synthesis and characterization of mixed-anion and solid-state Pb-containing materials. Emphasis is placed on exploring the interaction of the stereochemically active lone pairs on the Pb $6s^2$ with other atoms that results in thermochromic behavior. Her plans for the future are to continue pursuing knowledge and to gain more experiences through a position in an academic setting as professor in solid state chemistry; or a position in a research facility in developing new methods to synthesize new materials to many industrial applications.